LITHOS 400-401 (2021) 106396

Contents lists available at ScienceDirect

LITHOS

journal homepage: www.elsevier.com/locate/lithos

Research Article

Fractionation by compositional magma splitting: An example from Cerro Munro, Argentina

Carmen Rodríguez [a,b,*], Eugenio Aragón [c,d], Juan Díaz-Alvarado [e], Antonio Castro [a], Rocío Pedreira [f], Antonio Sánchez-Navas [g], Joan Martí [b]

[a] Instituto Andaluz de Ciencias de la Tierra (UGR-CSIC), Avda de las Palmeras 4, 18100 Armilla, Granada, Spain
[b] Geociences Barcelona (CSIC), c Lluís Solé i Sabaris s/n, 08028 Barcelona, Spain
[c] Facultad de Ciencias Naturales y Museo (UNLP), 122 y 60, s/n. (1900), La Plata, Buenos Aires, Argentina
[d] Centro de Investigaciones Geológicas, UNLP-CONICET, Calle 1 N° 644 (1900), La Plata, Argentina
[e] Instituto Geológico y Minero de España (IGME), Madrid, Spain
[f] Département des Sciences Appliquées, Unité d'enseignement en Sciences de la Terre, 555 Boulevard de l'Université (G7H 2B1), Chicoutimi, Québec, Canada
[g] Departamento de Mineralogía y Petrología, Universidad de Granada, Avda Fuentenueva s/n, 18071 Granada, Spain

ARTICLE INFO

Keywords:
Calc-alkaline magmatism
Fractionation
Mafic microgranular enclaves
Second boiling
Geochronology
Cathodoluminiscence

ABSTRACT

The Paleocene-Eocene Cerro Munro pluton, to the east of the North Patagonian Batholith (NPB), is a tonalitic intrusion emplaced as a shallow, small, sub-circular tonalite-granodiorite body hosting abundant co-magmatic mafic microgranular enclaves (MME). Besides, the intrusive body is crosscut by radial porphyritic dikes and has been related to andesitic, dacitic and rhyolitic dikes, lava flows and ignimbrites cropping out at neighboring areas. Magmatic contacts between MME and host tonalites, together with their common geochemical features, suggest derivation from a common parental magma, although short-range mineralogical and geochemical differences point to an early crystallization of MME (chilled margins) at the sidewalls of ascent conduits or at shallow reservoirs. The established thermal gradient and the advance of the solidification front were responsible for the presence of the mafic microgranular and tonalitic subsystems and, in a continuous process, promoted the water saturation and the second boiling that finally account for the segregation of a water rich highly differentiated residual liquid. Hbl-Pl cumulate textures observed in the tonalites and mafic enclaves, as well as incompatible element-enriched rhyolitic melts record the results of this in-situ differentiation process. U—Pb zircon ages obtained from tonalites (57.1 ± 1.4 Ma), dacitic (55.4 ± 0.6 Ma) and rhyolitic (54.1 ± 0.7 Ma) dikes constrain an age of around 54 Ma for the final consolidation of the tonalitic magma and the crystallization of the expelled highly differentiated melts. This age coincides with the deposition of dacitic volcanic and volcanoclastic deposits to the north of the Cerro Munro pluton, which suggests that the fractionation process led to the extrusion of segregated melts, favored by extension, uplift and exhumation of an active rift tectonic setting.

1. Introduction

Differentiation of silicic magmas is among the most debated topics in igneous petrology (Masotta et al., 2021). Granites (sensu *lato*) have been recently described as cumulate rocks that formed during the segregation and/or expulsion of an interstitial liquid (Lee and Morton, 2015; Vernon and Collins, 2011). Thus, many intermediate and felsic plutons, of diorite to granodiorite compositions, are interpreted as potential residues left behind at the time of rhyolitic eruptions (Bachmann and Bergantz, 2004; Bachmann and Bergantz, 2008; Bachmann and Huber, 2016; Deering and Bachmann, 2010). The expected residual features can be more likely evidenced in plutonic rocks since their slow post-entrapment cooling (Bacon, 1986). At the same time, these cumulate features are finally disguised in plutonic rocks (Guilherme and Mark, 2013; Lee and Morton, 2015). The amount of liquid retained in those cumulate, or mush-type magmatic residues, may represent a low fraction corresponding to the terminal porosity, around 20–30% liquid (Donev et al., 2004). Moreover, it has been shown with experiments that major-element geochemical trends of granite (*s.l.*) batholiths and calc-alkaline volcanic rocks follow the array of cotectic liquids (Castro, 2020, 2021), implying that separation of liquid and crystals actually was an efficient process in silicic magma differentiation within the crust.

* Corresponding author at: Instituto Andaluz de Ciencias de la Tierra (UGR-CSIC), Avda de las Palmeras 4, 18100 Armilla, Granada, Spain.
E-mail address: carmen.ralmodovar@csic.es (C. Rodríguez).

https://doi.org/10.1016/j.lithos.2021.106396
Received 22 March 2021; Received in revised form 5 July 2021; Accepted 21 July 2021
Available online 27 July 2021

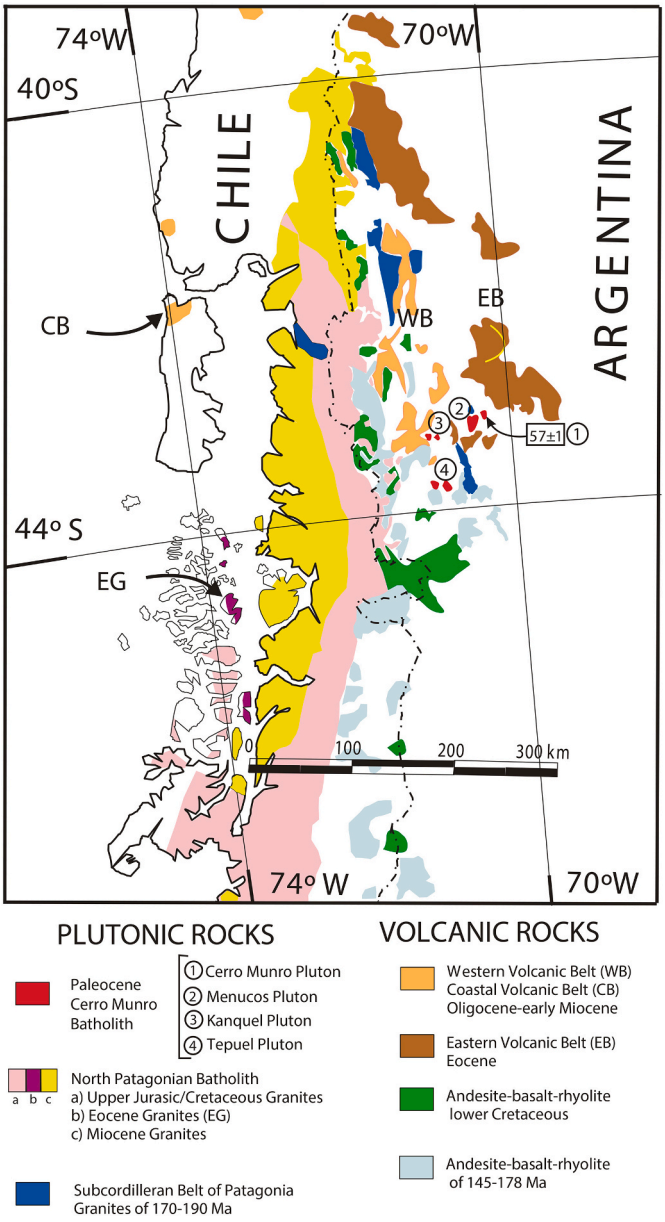

Fig. 1. Location map of northern Patagonia, showing the major igneous units related to the active margin from the Jurassic to the Cenozoic. Numbered circles provide the location for post-tectonic Palaeocene plutons. The NPB time-space distribution is modified from Pankhurst et al. (1999).

Compaction and hindered settling (Bachmann and Bergantz, 2004), magma cooling or solidification (Pistone et al., 2020) and/or volume contraction of the cooling magma chamber (John and Blundy, 1993; John and Stünitz, 1997) can be mechanisms responsible for the melt extraction. However, the high viscosity of silicic systems makes crystal–liquid separation inefficient by gravity forces, compaction and hindered settling (Glazner, 2014).

To solve this paradox, the old concept of Sisson and Bacon (1999) that exsolved water may assist crystal-liquid separation by gas filter pressing, in the course of crystallization, is gaining strength (Boudreau, 2016; Lee et al., 2015; Pistone et al., 2015; Pistone et al., 2020; Rodríguez and Castro, 2017; Weinberg et al., 2021). The thermal gradient, inherent to the walls of ascent conduits, imposes a magma solidification front where is effective a process called "compositional magma splitting". In this paper, we use the term "compositional magma splitting" to refer to the process in which a fractionated liquid is segregated by gas-driven filter pressing (Rodríguez and Castro, 2017; Sisson and Bacon, 1999), within a thermal boundary layer corresponding to the solidification front.

Assessing silicic magma differentiation in the upper continental crust can be constrained by the crystallization process, the pressure of emplacement and initial water content of plutonic rocks that are spatially and temporally associated with rhyolitic volcanic eruptions or subvolcanic complexes. Here we show a geochemical, textural and geochronological study of a small tonalite intrusion, and its spatially and temporally associated volcanic and subvolcanic rocks from the Eastern Volcanic Belt in Patagonia. On one hand, we show the relations of autoliths and host plutonic rocks to decipher processes of crystallization and differentiation by compositional magma splitting in ascent conduits at the time of emplacement and cooling. On the other hand, we compare ages and geochemical/textural patterns of subvolcanic rocks surrounding the plutonic intrusion.

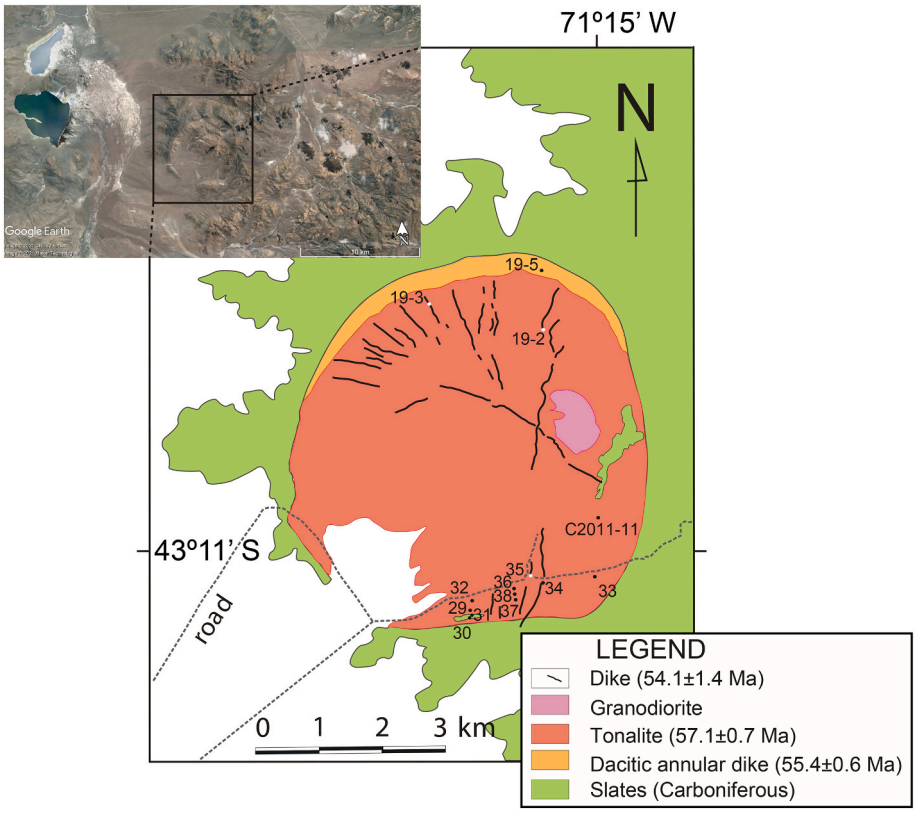

Fig. 2. Inset corresponds to a satellite image showing the morphology of the pluton in the upper left corner. Geological map of Cerro Munro Tonalite with location of the collected samples.

2. Geological setting

The Paleocene Cerro Munro pluton belongs to a group of small intrusions (5 to 10 km in diameter) emplaced to the east of the North Patagonian batholith during a time period (60–50 *Ma*) characterized by voluminous ignimbrite successions (Fig. 1). In the area of Cerro Munro, shallow plutons were intruded by sub-volcanic rocks while the volcanic products of the Pilcaniyeu Volcanic Belt and Cautiva Complex were deposited (Spikermann, 1978; Turner, 1982). A K/Ar age of the Cautiva Complex volcanic rocks yielded 54 ± 3 Ma (Turner, 1982). Volcanic rocks are included in the Eastern Palaeocene Volcanic belt defined as a rhyolitic–basaltic bimodal volcanism (Rapela et al., 1987). The Eastern Palaeocene Volcanic belt is constituted by rhyolites and dacites, mostly erupted as large ignimbrite plateaux, with subordinate domes and lava flows (Aragón and Mazzoni, 1997; Rapela et al., 1987), suggesting an ignimbrite flare-up (Aragón et al., 2011; Aragón et al., 2018). To the west of the Eastern Palaeocene Volcanic belt, a second and younger volcanic belt known as the Western Oligocene Volcanic belt defines a typical calc-alkaline association (Rapela et al., 1983; Rapela et al., 1987) (Fig. 1). The volcanic rocks of the Western Oligocene Volcanic belt also started as dacite-rhyolite flows and ignimbrites. The top of the sequence is mostly andesitic to basaltic and shows a range of K/Ar ages of 24 to 33 *Ma* (Rapela et al., 1987). Coeval to the Western Oligocene Volcanic belt, on a fore-arc setting, the Coastal Volcanic belt (Muñoz et al., 2000) is constituted by basalts of primitive composition.

To the west of the Cerro Munro area, the main North Patagonian batholith was emplaced along the main cordillera of the Patagonian Andes (Fig. 1) with two main batholith building episodes at this latitude, one in the upper Cretaceous and the second in the mid-Miocene, separated by a magmatic gap during the Paleogene (e.g., Aragón et al., 2011; Fernández Paz et al., 2018; Iannelli et al., 2018).

The Paleogene is controlled by the subduction of the Farallon-Aluk active ridge, the detachment of the Farallon plate, the opening of a slab window, mantle upwelling and the development of the Patagonides active rift (Aragón et al., 2011; Aragón et al., 2018). Therefore, emplacement of the Cerro Munro Pluton is controlled by extension, uplift and the exhumation of the Eastern Paleocene Volcanic belt, previous to the Miocene Andean Orogen (Savignano et al., 2016). According to this, the Cerro Munro pluton is the first example where a plutonic roof from the Eastern Paleocene Volcanic Belt, hypothetically representing one of the shallow magma reservoirs for ignimbrite and rhyolite eruptions, is exposed.

3. The Cerro Munro pluton and related subvolcanic rocks

The Paleocene-Eocene Cerro Munro pluton is a shallow ellipsoidal body with an area of 25 km^2 in a map view with a major axis azimuth of N 35° W and a maximum diameter of 8 km (Fig. 2). The Cerro Munro pluton intrudes into Carboniferous-Permian sediments from the Tepuel Group. Field relationship between the tonalitic pluton and intruding subvolcanic rocks show that the latter are arranged as radial and cross-cutting dikes within the pluton and as an annular dike intruded at the contact between the tonalitic pluton and the host rock in the northern boundary (Fig. 2). Late porphyritic radial dikes are mainly located towards the margins of the plutonic body, but do not cut the surrounding volcanic rocks, except for the case of the rhyolitic dikes to the south (Fig. 2). The groundmass proportion of porphyry dikes increases near the northern contact. The intrusive body is formed by pale gray to pink, medium to coarse-grained rocks (Fig. 3) ranging from Qz-diorites/tonalites to granodiorites at the core, showing concentric zoning. Main plutonic facies host abundant dark, fine-grained enclaves, as well as irregular patches and dikes of micro-leucogranites (graphic and miarolitic), dikes of aplites, and abundant radial porphyritic and lamprophyric dikes of andesitic, dacitic and rhyolitic composition. Mafic microgranular enclaves (MME) are abundant in the Cerro Munro pluton, decreasing their concentration towards the pluton core. They are of

Fig. 3. Field relations between tonalites and MME from Cerro Munro. (a and b) Outcrop of MME within the tonalite. (c) Rounded microgranular enclave of dm-size hosted in the coarse-grained tonalite A312–33. (d) Coarse-grained texture of the tonalite A312–32.

igneous appearance and variable size from several cm to dm (Fig. 3). Shapes vary from irregular and angular to rounded, the smallest ones showing the more rounded shape (Fig. 3a, b and c).

4. Sampling and analytical techniques

4.1. Whole rock and mineral analyses

Sample location of igneous rocks is showed in Fig. 2. Sampling on the Cerro Munro pluton was arranged to cover a wide range of the igneous rocks that constitute the intrusive body, including MME, porphyritic, subvolcanic and host rocks (Fig. 2). Paired samples of MME and host tonalites were collected in order to discriminate between local- and pluton-scale processes of magma fractionation. Also the dacitic annular dike was sampled, as it is assumed to correspond to the volcanic counterpart of the Cerro Munro magma chamber (Fig. 2).

Approximately 3 kg of fresh rock was collected from tonalites, porphyries, subvolcanic dikes and host rocks, crushed and milled to a fine powder for whole-rock geochemistry. In the case of MME, the entire sample was completely crushed, except the portion for thin sections. Major elements and Zr were determined by X-ray fluorescence (XRF) at the CIC (Centro de Instrumentación Científica, University of Granada, Spain). Precision for major elements is better than 1% relative. Trace elements, except for Zr, were obtained by inductively coupled plasma mass spectrometry (ICP-MS) also at the CIC, University of Granada, following the standard procedures described by Baedecker (1987). Analysis of trace elements was carried out according to the method described by Bea et al. (1996); the precision was approximately 2% and 5% error on concentrations of 50 and 5 ppm, respectively.

Thin sections of intrusive rocks were polished and subsequently analyzed in order to determine the composition of major elements in mineral phases using a JEOL JXA-8200 Superprobe at the University of Huelva (Spain). A combination of silicates and oxides (detailed in Table S1) were used for calibration. A beam of 5-μm diameter was used to analyse mineral phases to minimize Na migration. For the EBSD and cathodoluminiscence study, the porphyry sample was cut and polished with silica gel, and subsequently analyzed structurally.

In order to constrain the magmatic process generating rhyolite dikes hosted in Cerro Munro pluton, textural analysis was performed in Qz phenocrysts from a rhyolitic porphyry (sample A312–34; Table 7). This late porphyry cuts Cerro Munro tonalites and the country rocks (Fig. 2). Cathodoluminiscence studies in Qz from a rhyolite porphyry was carried out by an Environmental Scanning Electron Microscopy (ESEM, FEI Quanta 400) coupled with a cathodoluminscence detector (ChromaCL, Gatan), at the CIC, University of Granada (Spain). The Electron backscattered diffraction (EBSD) was conducted by a High-Resolution Scanning Electron Microscopy (HRSEM, AURIGA (FIB-FESEM) from Carl Zeiss SMT), also at the CIC, University of Granada (Spain). The sample was polished with colloidal silica of 0.01 μm of grain size for the cathodoluminiscence and EBSD study.

4.2. SHRIMP U—Pb Zircon geochronology

Samples were crushed and milled to a medium and fine grain fraction at the National University of La Plata (Argentina). Zircon separation was accomplished at the University of Huelva by traditional techniques

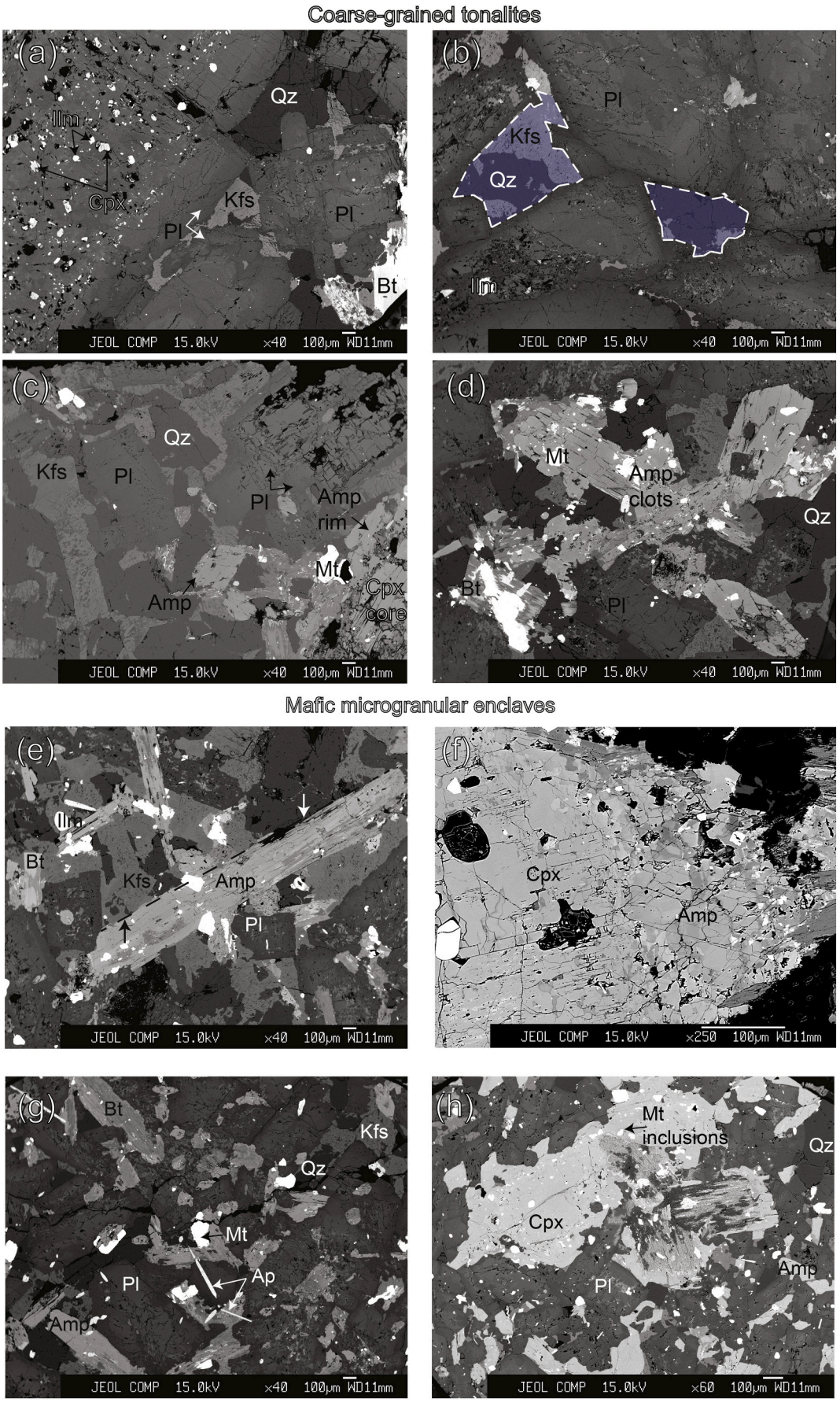

(caption on next page)

Fig. 4. (a-d) BSE images of tonalites and MME from Cerro Munro pluton. (a) Plagioclase phenocrysts have zoning and abundant inclusions of Fe—Ti oxides and clinopyroxene. (b) Plagioclase is arranged forming cumulate texture and interstices are occupied by Qz and Kfs, forming graphic textures (blue shadow zones). Amphibole is present as phenocryst and replacing Cpx rim (c). Amphibole clots also occur (d). (e-h) BSE images of MME from Cerro Munro. (e) Amphibole euhedral phenocryst indicates their early growth and high initial water contents. (b) Amp and Pl have smaller grain size in MME. (c) Acicular apatite also supports the high initial water contents of the magma. (d) Cpx phenochrysts are present in enclaves with abundant Mt. inclusions, typically related to a rapid subvolcanic growth, unable to expel the inclusions. Mineral abbreviations after Whitney and Evans (2010). (For interpretation of the references to colour in this figure legend, the reader is referred to the web version of this article.)

using dense liquids and magnetic separation (Frantz). Crystals free of impurities and fractures were selected by hand-picking with a binocular lens. Analyses were carried out in the SHRIMP II microprobe at Beijing SHRIMP Center (sample C2011–11) and in the SHRIMP II microprobe at the IBERSIMS, University of Granada (samples A312–34 and MUN19–5).

Analytical procedures are as follows at the SHRIMP Beijing Center (Chinese Academy of Geological Sciences). Zircon grains were mounted in epoxy, together with reference standards SL13 (U = 238) and TEMORA ($^{206}Pb/^{238}U = 0.06683$), and polished. Sectioned zircons were studied by CL imaging for selection of point analyses. The mounts were then cleaned and coated with high-purity Au. Core and rims were analyzed in several grains of each individual sample with the aim of identifying inherited cores. These selected points were target over the CL images and analyzed for U-Th-Pb isotopes with SHRIMP II, following methods given in Williams (1998) and references therein. A 10 kV negative oxygen primary beam was focused to c. 20 mm diameter. Positive secondary ions were extracted at 10 kV and mass analyzed at c. R5000 on a single ETP multiplier by peak stepping through the isotopes of interest. Analytical uncertainties are 1 s precision estimates. All the analyses listed and plotted were corrected for common Pb using the measured ^{204}Pb and a common Pb composition appropriate to the age of each spot (Cumming and Richards, 1975).

Analytical methods are as follows at the IBERSIMS facilities (University of Granada, Spain). Zircon concentrates were cast on a 3.5 cm diameter epoxy mount, together with zircon standards (TEMORA, SL13 and GAL zircon) and documented by SEM-CL. Mounts were coated with gold (80-μm thick) and inserted into the SHRIMP for analysis. Each selected spot was rastered with the primary beam during 120 s prior to analysis, and then analyzed over 6 scans following the isotope peak sequence: $^{196}Zr_2O$, ^{204}Pb, 204.1 background, ^{206}Pb, ^{207}Pb, ^{208}Pb, ^{238}U, ^{248}ThO, ^{254}UO. Every peak of each scan was measured sequentially 10 times with the following total counts per scan: 2 s for mass 196; 5 s for masses 238, 248, and 254; 15 s for masses 204, 206, and 208; and 20s for mass 207. The primary beam, composed of $^{16}O^{16}O^{2+}$, was set to an intensity of 4 to 5 nA, using a 120-μm Kohler aperture, which generates 17 × 20-μm elliptical spots on the target. The secondary beam exit slit was fixed at 80 μm, reaching a resolution of about 5000 at 1% peak height. Mass calibration was carried out on the GAL zircon (ca. 480 *Ma*, very high U, Th and common lead content; (Montero et al., 2008). Sessions initially involved the measurement of SL13 zircon (Claoue-Long et al., 1995), used as a concentration standard (238 ppm U). TEMORA zircon (ca. 417 *Ma*, Black et al., 2003), used as isotope ratios standard, was measured every 4 unknowns.

The final result for each isotope was calculated as the value at the mid-time of the analysis resulting from the regression line. $^{206}Pb/^{238}U$ was estimated from the measured $^{206}Pb^+/^{238}U^+$ and UO^+/U^+, following the method of Williams (1998). Plotted and tabulated analytical uncertainties are 1σ precision estimates. Concordia ages have been calculated with ISOPLOT 3.0 software (Ludwig, 2003). Uncertainties are 95% confidence limits ($t\sigma$, where t is the student's t multiplier) and include the uncertainty in the Pb/U calibration (ca. 0.3–0.5%). Ages were calculated with λ errors and MSWD was determined using Concord. + Equiv. Ages were calculated using the constants recommended by the IUGS Subcommission on Geochronology (Steiger and Jäger, 1977).

5. Petrography, mineral chemistry and geobarometry

5.1. Tonalites

These are medium- to coarse-grained, mesocratic rocks composed of Pl, Amp, Kfs, Qz, Bt, ± Cpx (abbreviations are according to Whitney and Evans, 2010) as essential minerals. Accessory minerals are Ap, Zr, Ilm, Mt., Aln and Spn (Fig. 4). Plagioclase appears as euhedral to subhedral crystals, complexly zoned with patches and oscillatory zones (Fig. 4a and b), ranging in composition from An_{50} at the cores to An_{18} (subscripts denote mol% of anorthite) near the rims (Table 1 and Fig. 5a). Reverse zoning is present in intermediate layers of crystals. Plagioclase cores show patching zoning and are surrounded by fine oscillatory zones in which resorption surfaces may be present (Fig. 4a). Patching zoning cores may contain tiny inclusions of pyroxene (Fig. 4a). Plagioclase crystals form an interlocked framework, resembling cumulate-like textures (Fig. 4b) in which, quartz and occasionally K-feldspar occupy the interstices giving rise to graphic intergrowths.

Amphiboles tend to form subhedral crystals, partially molded by plagioclase (Fig. 4c and d). Note that amphibole is not present as inclusion in tonalites. They are classified as Mg-hornblende (Table 2 and Fig. 5b) and contain inclusions of Ilm and Ti—Mt (Table S2). Amphibole

Table 1
Microprobe analyses of plagioclases from the Cerro Munro tonalites.

Sample	29	29	29	29	29	29	29	29	32	32	32	32	32	33
Run	29–4	29–5	29–6	29–7	29–12	29–13	29–14	29–15	32–4	32–7	32–11	32–12	32–13	33–2
Position [a]	inc	core	int	rim	core	int	int	rim	core	rim	core	int	rim	core
SiO_2	65.81	58.94	57.59	63.83	59.31	56.71	60.49	62.96	58.67	65.51	61.14	56.44	60.34	56.22
Al_2O_3	21.61	25.87	26.79	22.39	25.66	27.55	25.02	23.40	25.79	21.56	23.79	26.98	24.22	27.60
FeO	0.31	0.26	0.21	0.14	0.38	0.28	0.31	0.25	0.35	0.12	0.34	0.41	0.32	0.35
CaO	2.36	7.20	8.28	3.09	7.06	9.08	6.31	4.38	7.47	2.27	5.17	8.71	5.48	9.33
Na_2O	9.77	7.15	6.71	9.33	7.36	6.08	7.47	8.72	7.02	9.87	8.37	6.69	8.26	5.89
K_2O	0.62	0.45	0.31	0.78	0.54	0.32	0.58	0.59	0.43	0.71	0.87	0.38	0.48	0.36
BaO	0.01		0.08	0.04	0.02	0.03	0.06	0.22		0.06	0.06	0.09	0.08	0.04
Total	100.6	99.97	100.2	99.67	100.5	100.2	100.4	100.8	99.95	100.2	100.0	99.88	99.36	99.98
X_{An}	0.11	0.35	0.40	0.15	0.34	0.44	0.31	0.21	0.36	0.11	0.24	0.41	0.26	0.46
X_{Ab}	0.85	0.63	0.58	0.81	0.63	0.54	0.66	0.76	0.61	0.85	0.71	0.57	0.71	0.52
X_{Or}	0.04	0.03	0.02	0.04	0.03	0.02	0.03	0.03	0.02	0.04	0.05	0.02	0.03	0.02

inc: phase included in Amp.
aPosition represent the relative position of spot analyses within the crystal: int — intermediate between core and border.

also may appear forming polycrystalline aggregates or clots (Fig. 4d). Clinopyroxene (Mg# = 0.75; Table 3 and Fig. 5c) is partially transformed to amphibole, occurring as inclusions and relict cores (Fig. 4a and c). Biotite (Mg# = 0.66) (Table S3) appears as subhedral and anhedral crystals, in some cases, partially chloritized, and containing inclusions of apatite, zircon and opaque minerals (Fig. 4a and d). Fluorapatite, with up to 4.8 wt% of F, shows euhedral habit and also is included in Amp and Pl crystals.

Geothermobarometry was carried out in amphibole crystals with all regressions available in the literature for calc-alkaline compositions and low-pressure environments (Table 2). However, the low-pressure values recorded in the Cerro Munro pluton invalidate most of the estimations due to the regressions not being reliable for pressure lower than 1.3 kbar (Ridolfi and Renzulli, 2012) or for pressures lower than 0.73 kbar (Ridolfi et al., 2010). Thus, values lower than 0.73 kbar were not included in Tables 2, 5 and 8. Nonetheless, we can establish a subvolcanic pressure (<1 kbar), without an accurate pressure range, for tonalites in the Cerro Munro pluton. Temperatures range from 754 to 842 °C being mostly clustered at around 790 °C and melt water content when the amphibole crystallized is close to 3 wt% (Table 2). These are near-solidus conditions in water-poor tonalitic to quartz-dioritic magmas, in agreement with the late crystallization of Amp.

5.2. Mafic microgranular enclaves

These are fine-grained rocks formed by a similar mineral assemblage compared to the host tonalites. Main differences consist in the presence of Opx, the higher abundance of Cpx and subtle differences in textures and modal abundances.

Plagioclase is euhedral (Fig. 4) and shows normal zoning, ranging in composition (mole %) from An_{67} at the core to An_{16} at the rim (Table 4, Fig. 5a). Reverse zoning is not observed in the case of enclaves. Pyroxenes are partially replaced by amphibole (Fig. 4f) and are surrounded by plagioclase (Fig. 4h). Amphibole (Mg-Fe-hornblende to actinolite; Table 5, Fig. 5b) tends to form acicular phenocrysts (Fig. 4e), polycrystalline aggregates and is also replacing the Cpx (Fig. 4f). Amphibole and clinopyroxene together with magnetite (Ti-Mt; Table S2), are slightly more abundant with respect to the host tonalite. Actinolite occurs often at the rims of amphibole crystals in MME (Table 5 and Fig. 5b). Plagioclase show polycrystalline interlockings, leaving the interstices occupied by Amp, Kfs and Qz (Fig. 4g and h). Clinopyroxene (Mg# of 0.74; Table 6, Fig. 5c) is present as inclusions in Pl, as relict cores in Amp and forming subhedral crystals with oxide inclusions (Fig. 4h). Orthopyroxene (Table 6) appears as relict cores in amphibole crystals and as inclusion in Pl. Biotite (Mg# = 0.62; Table S3) forms anhedral, partially chloritized crystals, occupying interstices. The acicular habit of apatite (Fig. 4g) is indicative of quenching (Janoušek et al., 2000; Wyllie et al., 1962). Geothermobarometry estimations on amphibole crystals are listed in Table 5, yielding pressure values lower than 1 kbar, similar to the tonalites. Temperatures range from 622 to 861 °C being mostly clustered at around 750 °C (Table 5), which are slightly lower than the conditions of the host tonalites and quartz diorites mentioned above. Water melt contents at the amphibole saturation are around 3.5 wt%.

5.3. Subvolcanic dikes

Porphyritic dikes show coherent, non-fragmental textures and range in composition from andesites to rhyolites, having a common mineral assemblage with phenocrysts of Opx, zoned Pl, Amp and Bt (Fig. 6); except for the rhyolitic dike, where Kfs and Qz are major phases. Orthopyroxene, Amp and Pl crystallize as phenocrysts, while the matrix is composed of Pl, Amp, Cpx, Bt, Qz and K-fsp and Fe—Ti oxides (Fig. 6). Phenocrysts of euhedral zoned plagioclase range in composition from An_{53} at the core to An_{28} at the rim whereas the plagioclases from the matrix range from An_{31} at the core to An_{11} at the rim (Table 7). Amphiboles are classified as Mg-hornblende (Table 8) and form phenocrysts and inclusions within Opx. Cummingtonite crystallizes at the Amp polycrystalline aggregates in dacitic dikes. Clinopyroxene is only present in the matrix and orthopyroxene (En_{61} Fs_{32}) crystallize as phenocrysts in the andesitic porphyry (Table 9). Biotite (Mg# = 0.42, Table S3) is replacing amphibole and forming part of the matrix. Fe—Ti oxides are classified as Mt. and Ilm and Uvö is not present. The annular dacitic dike is characterized by a groundmass composed by Pl microlites (Fig. 6b). Most of the pressure values, given from Amp geothermobarometry of Ridolfi et al., 2010, are below the confidence range for geothermobarometry in igneous rocks, matching the subvolcanic pressure estimated for plutonic rocks. Temperatures range from 644 to 910 °C being the highest values found in the andesitic porphyry. The dacitic porphyries are mean temperatures values close to 700 °C, being the lowest values for the magmatic rocks from the Cerro Munro and the melt water contents are close to 4.9 wt%.

The textural study by cathodoluminiscence techniques in the mineral phases found in volcanic and plutonic rocks has clearly proved to be useful in recording magmatic processes as melt extraction, rejuvenation, mingling and recharge of magma chambers (Beane and Wiebe, 2012; D'Lemos et al., 1997; Fiedrich et al., 2017; Higgins, 2017; Matthews et al., 2011; Matthews et al., 2012; Wiebe et al., 2007).

The euhedral Qz from the A312–34 rhyolitic dike selected for the CL study is zoned (Fig. 7a and b) and can be subdivided in three areas, which correspond to growing stages: (1) An inner area with spherical shape and oscillatory zoning stands out in the main crystal (Fig. 7b). Circular shapes of magmatic crystals and stable luminescence behavior have been described in relation to oversaturation conditions in melt-rich environments (Götze et al., 2001; Kirkpatrick, 1981). (2) Subsequently, Qz crystallization progresses following the same crystal orientation

33	33	33	33	33	36	36	36	36	36	36	37	37	37	37	37	37
33–3	33–4	33–5	33–6	33–7	36–1	36–17	36–18	36–24	36–25	36–27	37–5	37–17	37–18	37–19	37–26	37–27
int	int	int	int	rim	int	int	rim	core	int	rim	int	rim	int	core	rim	core
59.49	59.11	58.15	58.94	58.47	59.35	58.93	64.57	60.65	55.33	62.78	62.49	63.39	54.93	56.41	64.11	55.57
25.30	25.71	26.43	25.67	25.99	25.59	25.64	22.21	24.75	28.08	22.85	23.24	22.74	28.61	27.29	21.96	27.16
0.28	0.37	0.33	0.30	0.27	0.32	0.24		0.30	0.29	0.20	0.21	0.30	0.32	0.30	0.19	0.36
6.77	7.13	7.91	7.17	7.50	6.46	6.75	2.11	5.55	9.44	3.35	4.34	3.86	10.42	9.11	2.52	9.23
7.22	6.93	6.60	6.86	6.67	7.48	7.13	9.53	7.60	5.61	9.59	8.85	9.23	5.53	6.18	9.84	6.05
0.60	0.52	0.44	0.50	0.40	0.45	0.33	0.14	0.61	0.29	0.43	0.67	0.47	0.25	0.35	0.72	0.28
0.06	0.06	0.01	0.05	0.06	0.07	0.07	0.04		0.12	0.09	0.06	0.09	0.12	0.06	0.13	0.03
99.89	100.1	100.1	99.73	99.52	100.0	99.34	98.74	99.82	99.49	99.43	100.0	100.2	100.3	99.88	99.65	98.83
0.33	0.35	0.39	0.36	0.37	0.31	0.34	0.11	0.28	0.47	0.16	0.21	0.18	0.50	0.44	0.12	0.45
0.64	0.62	0.59	0.62	0.60	0.66	0.64	0.88	0.69	0.51	0.82	0.76	0.79	0.48	0.54	0.84	0.53
0.03	0.03	0.03	0.03	0.02	0.03	0.02	0.01	0.04	0.02	0.02	0.04	0.03	0.01	0.02	0.04	0.02

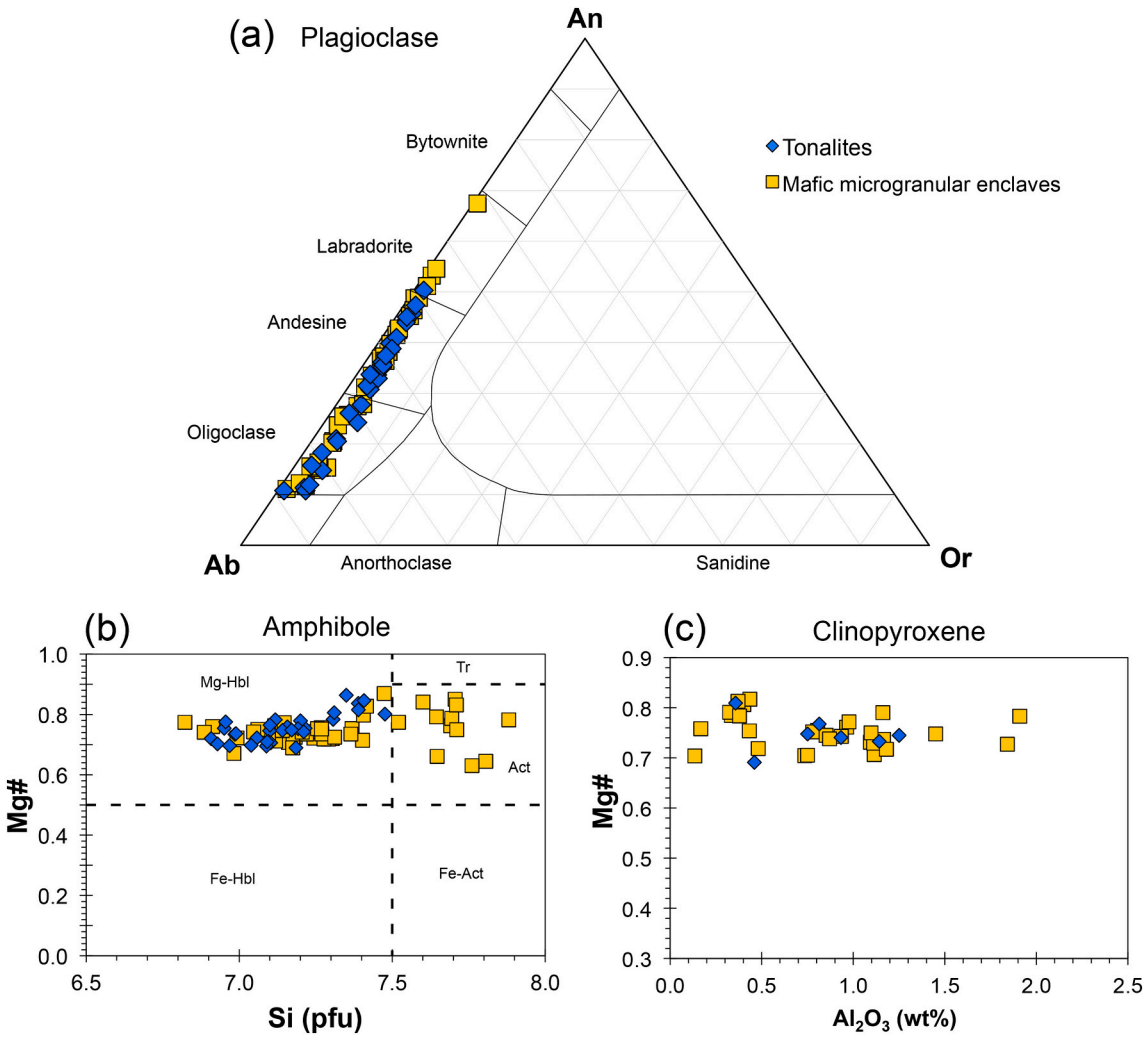

Fig. 5. Classification diagrams for plagioclase according to anorthite (X_{An}) and albite (X_{Ab}) molar fraction (a), for calcic amphiboles (b) and clinopyroxenes (c). Amphibole classification after (Locock, 2014). Si cation proportion is represented per formula unit.

(Fig. 7c and d) and according to well-developed crystal faces. This development of euhedral shapes is related to fluid-rich regions where the ion mobility is high and the oversaturation is lower than that corresponding to the spherical growth (Sunagawa, 1981). The EBSD study reveals a uniform orientation for both circular and euhedral crystals, close to c axis (Fig.7d). (3) Finally, the myrmekite rims around the main crystal (Fig. 7b) also follow the orientation along the c axis (Fig. 7d) and show bright red reaction rim (Götze et al., 2001), evidencing the final low-temperature episode of Qz growth.

6. Whole rock geochemistry

Twenty samples of tonalites, MME, porphyritic dikes, volcanic and host rocks were collected in fresh outcrops and analyzed for major and trace elements (Table 10). Both tonalites and MME are magnesian and calc-alkalic according to the MALI index (Frost et al., 2001) (Fig. 8a and b). Enclaves are metaluminous (Fig. 8c; except MME from A312–36) while tonalites are slightly peraluminous. Most samples of tonalites overpass the boundary of $SiO_2 > 63$ (equivalent to approx. > 20 vol% Qz). However, some of the rocks referred to as tonalites and most of the MME have $SiO_2 < 63$ wt% (Table 10 and Fig. 9) and must be classified as Qz-diorites. For simplicity in the descriptions we call tonalites to all the intrusive rocks in this study.

A systematic correlation between enclave-host pairs was found (Fig. 8). There is a marked silica gap separating enclaves and host tonalites from 58 to 62 wt% SiO_2 (Fig. 8). The molar ratio $K_2O/(K_2O + CaO)$ vs K_2O (Fig. 9a) of tonalites and enclaves follow a differentiation trend similar to calc-alkaline patterns of Cordilleran batholith (Patagonian batholith; Castro et al., 2011). Preferentially, enclaves have dioritic compositions while their host-rocks vary between Qtz-diorite and granodiorite/tonalite. However, Mg# and MgO contents depart slightly form Andean batholiths. The Mg# remains almost constant at relatively high values around 0.5 (Fig. 9b) over the whole silica interval from 57 to 65 wt% SiO_2, slightly higher than the average trend of the Andean Patagonian batholith. Also, the differentiation trend of plutonic rocks is departed from the main calc-alkaline cotectic (MCA; Castro, 2021) (Fig. 9e).

Chondrite-normalized REE diagrams (Fig. 10) show steep patterns in both tonalites and enclaves, i.e. enriched in light REE as compared to heavy REE. Negative *Eu* anomalies are marked for all tonalite–enclave pairs indicating fractionation of feldspar in both systems, except for the A312–36 pair that shows, by contrast, a positive *Eu* anomaly. Differences between MME and host tonalites are subtle. Consistently, enclaves present slightly higher ∑REE values, having the tonalites a more fractionated REE pattern than their related MME. For the case of the tonalite A312–36 (Fig. 10c), the enclaves show a wider range of compositional variation. Enclaves A312–36b and A312–36c are the more primitive ends whereas the enclave A312–36a and the tonalite A312–36 present a positive *Eu* anomaly indicating plagioclase accumulation together with amphibole or clinopyroxene fractionation according to the concave

Table 2
Microprobe analyses of amphiboles from the Cerro Munro tonalites.

Sample	29	29	29	29	29	32	32	32	32	32	32	36	36	36	36	36	36	36
Run	291	293	298	2911	2917	321	329	3210	3217	3222	3223	362	367	368	369	3612	3613	3621
Position[a]	int	int	core	rim	core	int	core	rim	core	core	int	core	rim	core	int	core	rim	int
SiO_2	49.30	49.60	49.07	50.35	49.81	50.19	48.97	52.36	47.79	47.56	51.78	47.12	52.32	49.28	49.29	47.54	51.90	49.22
TiO_2	1.51	1.31	1.38	1.11	1.29	1.24	1.36	0.68	1.66	1.87	0.71	1.67	0.80	1.08	1.06	1.57	0.72	1.35
Al_2O_3	5.59	5.29	5.74	4.57	5.01	4.74	5.13	3.42	6.52	6.62	3.48	6.19	3.27	4.57	4.38	5.95	3.54	4.94
Cr_2O_3		0.00		0.06	0.08	0.09	0.03	0.09	0.02	0.07		0.03	0.06			0.03	0.04	
FeO	11.73	11.48	10.97	12.91	12.55	11.49	12.62	9.86	11.37	12.58	9.84	12.31	9.04	12.72	13.45	11.95	8.91	12.42
MnO	0.20	0.20	0.23	0.27	0.30	0.26	0.32	0.11	0.16	0.29	0.14	0.19	0.21	0.31	0.34	0.21	0.09	0.29
MgO	16.21	16.59	16.43	15.98	15.97	16.60	15.45	18.49	16.07	15.28	18.01	15.80	18.73	15.75	15.39	15.94	19.00	15.58
NiO	0.04	0.05	0.03	0.12	0.02	0.02	0.04	0.09		0.06	0.10	0.03	0.04	0.05		0.01	0.05	0.06
CaO	11.31	11.22	11.15	11.05	11.06	11.12	10.83	11.43	10.94	11.00	11.68	11.00	11.78	11.10	11.04	11.07	11.69	11.18
Na_2O	1.63	1.54	1.65	1.40	1.43	1.58	1.51	1.25	2.02	2.03	1.31	1.59	1.01	1.31	1.12	1.58	1.06	1.22
K_2O	0.51	0.49	0.52	0.41	0.50	0.45	0.48	0.38	0.60	0.64	0.38	0.57	0.34	0.43	0.43	0.52	0.40	0.45
F	0.09	0.36	0.31	0.27	0.23	0.57	0.69	1.15	0.73	1.32	1.20	0.75	0.61	0.78	0.83	0.45	1.01	0.69
Total	98.10	98.13	97.48	98.5	98.24	98.34	97.42	99.29	97.87	99.33	98.63	97.25	98.20	97.38	97.30	96.82	98.41	97.4
Si (T)[b]	7.10	7.12	7.10	7.22	7.16	7.20	7.14	7.39	6.95	6.91	7.39	6.97	7.41	7.19	7.21	6.96	7.35	7.17
Al (T)	0.90	0.88	0.90	0.77	0.84	0.80	0.86	0.57	1.05	1.09	0.59	1.03	0.55	0.79	0.75	1.03	0.59	0.83
Ti (T)				0.01				0.04			0.02		0.05	0.02	0.03	0.02	0.06	
Ti (C)	0.16	0.14	0.15	0.11	0.14	0.13	0.15	0.03	0.18	0.20	0.05	0.19	0.04	0.10	0.08	0.15	0.02	0.15
Al (C)	0.05	0.01	0.08		0.01	0.00	0.02		0.07	0.04		0.05						0.02
Cr (C)				0.01	0.01	0.01	0.00	0.01	0.00	0.01		0.00	0.01			0.00	0.01	
Fe^{3+} (C)	0.23	0.39	0.23	0.44	0.42	0.37	0.40	0.40	0.24	0.24	0.30		0.35	0.42	0.48	0.45	0.42	0.38
Ni (C)	0.00	0.01	0.00	0.01	0.00	0.00	0.00	0.01		0.01	0.01	0.00	0.01	0.01		0.00	0.01	0.01
Fe^{2+} (C)	1.08	0.90	0.99	1.02	1.01	0.93	1.06	0.66	1.02	1.19	0.80	1.27	0.65	1.05	1.09	0.91	0.54	1.06
Mg (C)	3.48	3.55	3.54	3.42	3.42	3.55	3.36	3.89	3.48	3.31	3.83	3.48	3.95	3.43	3.36	3.48	4.01	3.39
Mn^{2+} (B)	0.02	0.02	0.03	0.03	0.04	0.03	0.04	0.01	0.02	0.04	0.02	0.02	0.03	0.04	0.04	0.03	0.01	0.04
Fe^{2+} (B)	0.11	0.09	0.11	0.09	0.08	0.08	0.08	0.10	0.12	0.10	0.07	0.25	0.08	0.08	0.08	0.10	0.10	0.07
Ca (B)	1.75	1.73	1.73	1.70	1.70	1.71	1.69	1.73	1.71	1.71	1.79	1.73	1.79	1.74	1.73	1.74	1.77	1.75
Na (B)	0.12	0.16	0.14	0.18	0.18	0.19	0.19	0.16	0.16	0.15	0.13		0.11	0.14	0.14	0.14	0.12	0.15
Na (A)	0.33	0.27	0.33	0.21	0.22	0.26	0.23	0.19	0.41	0.42	0.23	0.46	0.16	0.23	0.18	0.31	0.17	0.20
K (A)	0.09	0.09	0.10	0.08	0.09	0.08	0.09	0.07	0.11	0.12	0.07	0.11	0.06	0.08	0.08	0.10	0.07	0.08
OH (W)	1.96	1.84	1.86	1.88	1.90	1.74	1.68	1.49	1.67	1.39	1.46	1.65	1.73	1.64	1.62	1.79	1.55	1.68
F (W)	0.04	0.16	0.14	0.12	0.10	0.26	0.32	0.51	0.34	0.61	0.54	0.35	0.28	0.36	0.38	0.21	0.45	0.32
Cl (W)	n.a.	n.a.	n.a.	n.a.	n.a.	n.a.	n.a.	n.a.	n.a.	n.a.	n.a.	n.a.	n.a.	n.a.	n.a.	n.a.	n.a.	n.a.
Sum T,C,B,A	15.42	15.36	15.42	15.29	15.31	15.34	15.32	15.25	15.52	15.54	15.31	15.58	15.23	15.31	15.26	15.40	15.25	15.28
#Mg	0.75	0.78	0.76	0.75	0.76	0.78	0.75	0.84	0.75	0.72	0.81	0.70	0.85	0.75	0.74	0.77	0.86	0.75
T (°C)	792	790	786	767	779	777	775	783	818	825	754	842	774	778	774	829	786	771
P (kbar)[c]	0.74		0.77						0.94	0.96		0.88				0.83		
$H_2O^c_{melt}$ (wt%)	3.15	3.15	3.04	3.49	3.37	3.05	3.40	2.27	2.87	3.08	2.63	3.52	2.40	3.54	3.81	3.48	2.19	3.61

Sample	37	37	37	37	37	37	37	37	37	37	37	37	37
Run	371	374	378	379	3710	3711	3715	3716	3721	3722	3725	3729	3731
Position[a]	int	int	core	int	rim	core	rim	int	core	rim	rim	int	int
SiO_2	48.55	48.64	50.81	47.40	52.27	48.89	48.36	47.99	48.16	50.92	49.30	48.89	48.09
TiO_2	1.36	1.54	1.08	1.55	0.61	1.50	1.53	1.72	1.39	0.79	1.18	1.54	1.65
Al_2O_3	5.30	5.57	3.80	6.33	3.01	5.33	5.64	6.03	5.19	3.98	4.71	5.55	5.88
Cr_2O_3				0.11	0.03		0.15	0.00		0.07			0.04
FeO	13.35	12.82	11.63	13.57	10.35	13.56	13.91	12.27	13.85	9.43	14.35	13.32	12.35
MnO	0.29	0.21	0.27	0.26	0.31	0.29	0.34	0.30	0.31	0.24	0.37	0.30	0.24
MgO	15.27	15.63	16.86	14.97	17.63	15.19	14.90	15.70	14.89	18.09	14.94	15.23	15.85
NiO	0.04	0.01	0.01	0.03		0.07	0.06				0.00	0.00	0.08

(*continued on next page*)

Table 2 (*continued*)

Sample	37	37	37	37	37	37	37	37	37	37	37	37	37
Run	371	374	378	379	3710	3711	3715	3716	3721	3722	3725	3729	3731
Position[a]	int	int	core	int	rim	core	rim	int	core	rim	rim	int	int
CaO	10.87	10.93	11.07	10.89	11.55	10.73	10.79	10.84	10.83	11.56	10.76	10.82	10.98
Na_2O	1.78	1.96	1.40	2.05	1.20	1.81	1.79	2.02	1.82	1.59	1.74	1.78	2.00
K_2O	0.51	0.54	0.40	0.59	0.30	0.50	0.53	0.54	0.50	0.52	0.49	0.51	0.50
F	1.33	1.20	1.53	1.30	1.14	1.54	1.26	0.81	1.26	2.03	1.19	1.21	0.76
Total	98.62	99.06	98.86	99.04	98.39	99.41	99.25	98.21	98.19	99.22	99.03	99.14	98.4
Si (T)[b]	7.10	7.06	7.31	6.93	7.48	7.10	7.04	6.99	7.09	7.31	7.19	7.09	6.99
Al (T)	0.90	0.94	0.64	1.07	0.51	0.90	0.96	1.01	0.90	0.67	0.81	0.91	1.01
Ti (T)			0.05		0.02				0.01	0.01	0.01		0.00
Ti (C)	0.15	0.17	0.07	0.17	0.05	0.16	0.17	0.19	0.15	0.07	0.12	0.17	0.18
Al (C)	0.01	0.01		0.02		0.02	0.01	0.02				0.04	
Cr (C)				0.01	0.00		0.02			0.01			0.00
Fe^{3+} (C)	0.28	0.25	0.40	0.28	0.30	0.28	0.29	0.26	0.27	0.20	0.29	0.27	0.27
Ni (C)	0.00	0.00	0.00	0.00		0.01	0.01						0.01
Fe^{2+} (C)	1.24	1.19	0.92	1.26	0.89	1.24	1.28	1.12	1.32	0.85	1.34	1.23	1.11
Mg (C)	3.33	3.38	3.61	3.26	3.76	3.29	3.23	3.41	3.27	3.87	3.25	3.29	3.43
Mn^{2+} (B)	0.04	0.03	0.03	0.03	0.04	0.04	0.04	0.04	0.04	0.03	0.05	0.04	0.03
Fe^{2+} (B)	0.12	0.12	0.08	0.13	0.05	0.13	0.13	0.11	0.12	0.08	0.12	0.12	0.13
Ca (B)	1.70	1.70	1.71	1.71	1.77	1.67	1.68	1.69	1.71	1.78	1.68	1.68	1.71
Na (B)	0.14	0.15	0.18	0.14	0.14	0.17	0.15	0.16	0.14	0.11	0.15	0.16	0.14
Na (A)	0.36	0.40	0.21	0.45	0.19	0.34	0.36	0.41	0.38	0.34	0.34	0.34	0.43
K (A)	0.09	0.10	0.07	0.11	0.06	0.09	0.10	0.10	0.09	0.10	0.09	0.09	0.09
OH (W)	1.38	1.45	1.30	1.40	1.48	1.29	1.42	1.63	1.42	1.08	1.45	1.44	1.65
F (W)	0.62	0.55	0.70	0.60	0.52	0.71	0.58	0.37	0.58	0.92	0.55	0.56	0.35
Cl (W)	n.a.	n.a.	n.a.	n.a.	n.a.	n.a.	n.a.	n.a.	n.a.	n.a.	n.a.	n.a.	n.a.
Sum T,C,B,A	15.46	15.50	15.29	15.55	15.24	15.43	15.46	15.51	15.47	15.43	15.43	15.43	15.52
#Mg	0.71	0.72	0.78	0.70	0.80	0.71	0.70	0.73	0.69	0.81	0.69	0.71	0.74
T (°C)[c]	797	806	794	827	760	791	805	820	802	780	780	789	826
P (kbar)[c]		0.75		0.90			0.76	0.84				0.74	0.8
$H_2O^c_{melt}$ (wt%)	3.28	3.00	2.53	3.28	2.64	3.30	3.50	3.08	3.34	2.23	3.34	3.33	3.16

[a]Position represent the relative position of spot analyses within the crystal: int — intermediate between core and border.
[b]Structural amphibole formula was calculated according to Locock (2014)/
[c]Pressure, temperature and melt water content obtained by Amp thermobarometry from Ridolfi et al. (2010).

Table 3
Microprobe analyses of pyroxenes of the Cerro Munro tonalites.

Phase	Cpx	Cpx	Cpx	Cpx	Cpx	Cpx	Cpx
Sample	32 (relict core)	33 (inc)	33 (inc)	33 (inc)	36 (relict core)	36 (relict core)	37 (relict core)
Run	32–21	33–8	33–9	33–11	36–20	36–33	37–13
SiO_2	52.29	51.96	52.61	52.60	53.85	52.64	52.99
TiO_2	0.27	0.32	0.20	0.27	0.02	0.11	0.17
Al_2O_3	0.75	1.25	0.93	1.14	0.36	0.46	0.81
Cr_2O_3	0.06	0.09	0.05	n.d.	0.15	n.d.	0.03
FeO	8.79	8.91	8.98	9.42	6.45	10.62	8.22
MnO	0.39	0.33	0.34	0.35	0.32	0.33	0.51
MgO	14.62	14.60	14.37	14.48	15.32	13.33	15.21
NiO	0.00	n.d.	n.d.	0.02	n.d.	n.d.	0.02
CaO	21.54	21.48	21.76	21.67	23.08	21.94	21.49
Na_2O	0.49	0.42	0.44	0.43	0.21	0.37	0.38
K_2O	0.01	n.d.	0.01	0.00	0.02	n.d.	0.00
F	n.d.	0.15	n.d.	n.d.	0.17	0.13	0.03
Total	99.27	99.59	99.82	100.43	99.95	99.96	99.88
#Mg[a]	0.75	0.74	0.74	0.73	0.81	0.69	0.77

inc: phase included in Pl.
n.d.: not determined.
[a]Mg# = molar MgO/[MgO+ FeO].

upward pattern of HREE.

Subvolcanic dikes vary from andesites to rhyolites and follow a fractionation trend similar to tonalites and enclaves (Fig. 11). For the whole system, it is evidenced the departure from the MCA and the Patagonian batholith trend in the CaO–MgO diagram (Fig. 11f). The andesitic porphyries are plotted on the gap between enclaves and tonalites and present intermediate geochemical compositions between the studied plutonic rocks (Fig. 11). The rhyolitic porphyry is enriched in light elements as Li and Rb (Table 10) and presents a higher K/(K + Ca) ratio than tonalites and MME (Fig. 12). The REE pattern of the rhyolitic porphyry is clearly depleted (Fig. 11d) showing geochemical evidence of a long-lasting fractionation process. Dacitic annular dike has a similar composition to the more evolved tonalites and dacitic dikes (Fig. 11).

7. U-Th-Pb geochronology results

The main tonalitic facies of the Cerro Munro pluton, a porphyritic dike and a dacitic subvolcanic rock were sampled and analyzed for zircon geochronology with the aim to study the temporal relation between the crystallization of the shallow magma chamber, channelized intrusions and related volcanic deposits. Sample C.2011–11 (Fig. 2) is a fine-grained biotite-hornblende tonalite. The rock has abundant inclusions of MME that were avoided during the sample processing. The texture is subidiomorphic and the modal mineralogy includes zoned Pl, Hbl, Bt and interstitial Qz and Kfs, with some cases of perthitic and graphic textures. Apatite, titanite, zircon and opaque minerals are present as accessory minerals. Sample A312–34 (Fig. 2) is an inner rhyolitic dike with porphyritic texture and Qz and Kfs phenocrysts. The dacitic sample has Pl and Kfs phenocrysts and a porphyritic matrix composed of Pl, Kfs, Qz ± Amp. Considering the absence of nearby volcanic deposits, we have selected a dacitic annular dike as extrusive counterpart for the Cerro Munro intrusives (sample MUN-195; Fig. 2). Petrographic characteristics are exposed in section 5.3 and Fig. 6b.

7.1. U-Th-Pb geochronology results

Results are listed in the supplementary material (Table S4). Representative zircon crystals and spots from each sample are shown in Fig. 12 together with concordia diagrams and average ages. Zircon populations selected from all samples (Fig. 12) are euhedral to subhedral medium-large crystals (120–300 μm). CL images show simple internal structures in zircons, with parallel-banded zoning in more elongated crystals and concentric or sector zoning in less acicular zircons, although the tonalite sample (C2011–11) present some darker, less zoned zircon crystals (Fig. 12a). Th/U ratios are comprised between 0.5 and 1.7, typical of intermediate to basic magmatism, showing no relation with U—Pb ages.

For the tonalite sample, ten analyses with $^{206}Pb/^{238}U$ ages between 59.6 ± 2.7 and 53.8 ± 2.1 *Ma* (Table S4a) yield an estimation for the crystallization age of 57.1 ± 1.4 *Ma* (MSWD = 0.7) (Fig. 12a). Thirty analyses were carried out for the porphyritic rhyolite (A312–34), giving a lower intercept in the concordia diagram of 54.1 ± 0.7 *Ma* (MSWD = 1.4) (Fig. 12b). Considering only low discordance results, eighteen analyses yield $^{206}Pb/^{238}U$ ages between 56 and 52 *Ma*, resulting a mean age of 53.9 ± 0.6 *Ma* (MSWD = 1.2) (Table S4b). For the subvolcanic dacite sample, twenty-five analyses give highly close $^{206}Pb/^{238}U$ ages between 57.6 and 53.2 *Ma* (Table S4c). Low discordance data yield a statistical age (lower intercept) of 55.4 ± 0.6 *Ma* (MSWD = 3.0) (Fig. 12c).

8. Discussion

8.1. The Cerro Munro pluton: magmatic differentiation from a single parental magma

The mineralogical, textural, geochemical and geochronological characteristics of the Cerro Munro tonalites, MME and related porphyritic and subvolcanic rocks reveal the genetic linkage between the magmatic products that finally constitute the shallow magma reservoir.

The sampled tonalite shows a wide range of ages, between 59 and 53 *Ma*, while the ages obtained from the rhyolitic dike are more concentrated around 54 *Ma* (Table 8a and b, Fig. 12). This result is coincident, within the analytical error, with the age of subvolcanic dacite to the north edge of the intrusive complex (55.4 ± 0.6 *Ma*) (Table S4, Fig. 12). Accordingly, the protracted evolution of the quartz dioritic to tonalitic parental magma at the emplacement level or likely during an earlier evolution at deeper reservoirs or ascent conduits is recorded in the older antecrysts dated in the Cerro Munro tonalites (Fig. 13). The felsic liquid segregation, the main crystallization stage in the shallow emplacement level and the late dikes are dated around 54–55 *Ma* (Fig. 13) by the younger ages obtained in the tonalite and the best estimation of the crystallization ages for porphyries and subvolcanic intrusives. Besides, we interpret that the magma chamber consolidation is coeval with the eruption (mobilization) of dacitic and rhyolitic magmas according to the results of the subvolcanic ring dike and the age of the volcanic deposits of La Cautiva Complex (Turner, 1982) (Fig. 13). Apart from being coeval, plutonic and volcanic–subvolcanic rocks in the Cerro Munro area show important geochemical similarities between them, supporting the hypothesis of a genetic linkage. Besides, the textural characteristics and compositions of the Pl, Amp and Px phenocrysts in the porphyritic dikes are similar to those studied in the main tonalitic facies of the pluton. While rhyolites can represent the last fractionated liquids from the intrusive magma (tonalite to Qz-diorite), andesite dikes may represent the pristine, undifferentiated magma from which tonalites and enclaves were formed.

Cathodolumiscence images from Qz crystals in rhyolitic dikes (Fig. 7) indicate a multistage crystallization occurred in the magma chamber of the Cerro Munro pluton. During an early crystallization stage, euhedral Qz phenocrysts were formed. These were partially dissolved in the melt during ascent and decompression producing the spherical cores. Subsequently, spherical cores are regrown during slow cooling in a magma chamber previously to remobilization and injection in subvolcanic dikes, giving rise to the observed euhedral shape rims. Such slow cooling stage may have been associated with fluid-rich domains where the ion mobility is high (Sunagawa, 1981). This second crystallization stage was followed by a late *subsolidus* solidification of myrmekitic Qz and Kfs, as is evidenced by CL images (Fig. 7b).

Table 4
Microprobe analyses of plagioclases from the Cerro Munro enclaves.

Sample	29b	29b	29b	29b	29b	29b	29b	29b	29b	33a	33a	36A	36a	36a	36a	36a	36B	36B	36B	36B	36B	36B	36B
Run	29b-6	29b-7	29b-8	29b-9	29b-10	29b-19	29b-20	29b-25	29b-26	33a-12	33a-13	36A-2	36A-4	36A-8	36A-44	36A-46	36B-5	36B-6	36B-14	36B-15	36B-16	36B-17	36B-23
Position[a]	core	rim	core	int	rim	int	int	int	rim	core	rim	int	core	rim		inc	core	rim	core	rim	core	rim	inc
SiO_2	56.97	64.23	54.58	62.84	65.63	62.57	55.38	57.69	61.33	53.08	62.33	57.14	55.92	63.51	64.07	54.92	56.47	63.16	57.33	65.12	54.79	60.97	59.87
Al_2O_3	27.30	22.29	29.14	23.63	21.96	24.04	28.78	26.79	24.32	29.39	22.96	26.39	27.93	22.70	23.32	28.75	26.85	22.24	26.38	21.75	28.24	24.34	25.11
FeO	0.27	0.23	0.30	0.18	0.07	0.36	0.27	0.30	0.33	0.20	0.21	0.44	0.28	0.35	0.27	0.38	0.29	0.19	0.24	0.12	0.24	0.22	0.28
CaO	8.82	3.21	11.00	4.32	2.28	4.90	10.46	8.18	5.40	11.27	4.18	7.61	9.24	3.07	3.20	10.18	8.55	3.23	7.88	2.45	10.08	5.28	6.36
Na_2O	6.44	9.27	5.23	8.90	10.01	8.49	5.37	6.66	8.35	5.07	8.78	7.07	5.97	9.38	9.38	5.83	6.45	9.45	6.80	9.77	5.69	8.13	7.51
K_2O	0.28	0.85	0.19	0.55	0.18	0.38	0.24	0.31	0.47	0.19	0.55	0.39	0.32	0.56	0.66	0.15	0.31	0.40	0.40	0.61	0.24	0.46	0.42
BaO		0.09	0.02	0.05			0.12	0.06	0.16	0.04			0.05	0.06	0.02		0.08		0.05	0.06	0.07		0.03
Total	100.3	100.3	100.8	100.7	100.4	101.1	100.9	100.1	100.5	99.40	99.09	99.15	99.90	99.81	101.1	100.5	99.18	98.86	99.38	100.2	99.51	99.92	99.66
X_{An}	0.42	0.15	0.53	0.21	0.11	0.24	0.51	0.40	0.26	0.55	0.20	0.36	0.45	0.15	0.15	0.49	0.42	0.16	0.38	0.12	0.49	0.26	0.31
X_{Ab}	0.56	0.80	0.46	0.76	0.88	0.74	0.47	0.58	0.72	0.44	0.77	0.61	0.53	0.82	0.81	0.50	0.57	0.82	0.60	0.85	0.50	0.72	0.66
X_{Or}	0.02	0.05	0.01	0.03	0.01	0.02	0.01	0.02	0.03	0.01	0.03	0.02	0.02	0.03	0.04	0.01	0.02	0.02	0.02	0.03	0.01	0.03	0.02

Sample	37a	37a	37a	37a	37a	37a	38	38	38	38	38	38
Run	37a-3	37a-4	37a-5	37a-6	37a-13	37a-16	38–9	38–10	38–14	38–18	38–19	38–23
Position[a]	int	core	int	rim	int	core	core	rim	inc	core	rim	
SiO_2	57.90	54.80	58.20	64.38	59.06	58.52	56.50	63.61	61.06	50.40	61.55	60.78
Al_2O_3	26.31	27.88	26.10	21.80	25.56	26.00	27.59	22.83	24.82	31.53	23.90	24.64
FeO	0.25	0.33	0.30	0.41	0.36	0.36	0.31	0.26	0.37	0.30	0.34	0.32
CaO	7.88	9.55	7.83	2.59	7.00	7.65	8.85	3.63	5.71	13.76	5.15	5.80
Na_2O	7.27	5.90	7.04	10.03	7.44	7.08	6.38	9.92	7.99	3.61	8.11	7.87
K_2O	0.34	0.32	0.38	0.43	0.39	0.49	0.27	0.58	0.56	0.11	0.36	0.66
BaO			0.13	0.03	0.12	0.07	0.02	0.09	0.05	0.06		0.01
Total	100.2	99.06	100.1	99.83	100.2	100.4	100.2	101.3	100.8	99.90	99.60	100.4
X_{An}	0.37	0.46	0.37	0.12	0.33	0.36	0.43	0.16	0.27	0.67	0.25	0.28
X_{Ab}	0.61	0.52	0.61	0.85	0.64	0.61	0.56	0.81	0.69	0.32	0.72	0.68
X_{Or}	0.02	0.02	0.02	0.02	0.02	0.03	0.02	0.03	0.03	0.01	0.02	0.04

[a]Position represent the relative position of spot analyses within the crystal: int — intermediate between core and border.
inc: phase included in Cpx or Amp.

Table 5
Microprobe analyses of amphiboles from the Cerro Munro enclaves.

Sample	29b	29b	29b	29b	29b	29b	29b	29b	29b	29b	29b	29b	33a	33a	33a	33a	33a	33a	33a	33a	33a	33a	33a
Position[a]	int	int	int	int	rim	core	rim	core	int	rim	rim	int	core	rim	rim	int	int	int	int	int	core	rim	int
Run	29b1	29b3	29b4	29b11	29b12	29b14	29b17 (inc)	29b21 (inc)	29b22	29b23	29b24 (inc)	29b27	33a1	33a2	33a4	33a5	33a11	33a14	33a15	33a17	33a18	33a19	33a23
SiO_2	49.40	49.11	50.27	50.70	53.84	49.58	49.17	53.84	49.55	52.83	51.18	50.39	53.67	53.88	55.06	47.32	52.30	52.42	52.93	53.06	54.31	52.11	49.06
TiO_2	1.11	1.13	1.25	0.99	0.35	1.35	1.26	0.23	1.49	0.62	0.26	1.04	0.16	0.23	0.06	1.62	0.14	0.33	0.07	0.17	0.29	0.13	1.32
Al_2O_3	4.64	4.85	4.40	4.04	2.08	5.03	5.24	1.50	5.17	2.84	3.86	4.48	1.40	1.75	0.47	5.99	1.27	2.12	1.51	1.33	1.74	1.76	5.29
Cr_2O_3	0.08	0.09	0.01	0.02			0.02	0.00		0.05	0.03	0.13	0.04	0.03	0.09	0.12	0.06	0.11	0.04	0.09			0.05
FeO	14.06	14.35	13.92	14.08	10.70	12.15	14.01	12.14	12.35	11.14	13.50	13.08	14.90	10.57	10.05	14.32	18.11	13.59	16.20	18.71	7.86	15.83	13.07
MnO	0.33	0.31	0.33	0.42	0.51	0.31	0.41	0.43	0.27	0.21	0.41	0.21	0.64	0.30	0.38	0.51	0.66	0.42	0.54	0.70	0.18	0.49	0.30
MgO	15.06	14.74	15.23	15.24	18.14	16.15	14.88	17.45	16.12	17.16	16.12	15.76	14.37	17.67	18.03	14.04	12.16	15.06	14.03	11.74	19.37	14.14	15.77
NiO	0.05		0.01							0.04			0.04	0.08	0.03	0.04	0.00	0.03			0.02	0.03	
CaO	11.06	10.96	10.99	11.08	11.26	11.08	11.16	11.53	11.14	12.12	10.84	11.14	12.16	12.13	12.48	11.15	11.89	12.55	11.53	11.81	12.22	12.04	11.15
Na_2O	1.20	1.46	1.35	1.19	0.58	1.42	1.47	0.35	1.49	0.71	0.96	1.30	0.18	0.40	0.07	1.55	0.25	0.27	0.23	0.24	0.45	0.29	1.49
K_2O	0.41	0.43	0.37	0.33	0.12	0.50	0.47	0.11	0.48	0.23	0.28	0.39	0.07	0.08	0.03	0.54	0.08	0.08	0.07	0.05	0.15	0.10	0.56
F	0.25	0.33	0.40	0.34	0.45	0.55	0.40	0.13	0.25	0.26	0.04	0.25	0.08	0.27		0.58	0.17	0.16		0.03	0.45	0.10	0.67
Total	97.63	97.75	98.53	98.43	98.03	98.12	98.48	97.70	98.29	98.21	97.49	98.17	97.70	97.38	96.73	97.78	97.07	97.13	97.15	97.94	97.03	97.01	98.73
Si (T)[b]	7.18	7.16	7.24	7.30	7.65	7.14	7.12	7.69	7.12	7.52	7.37	7.25	7.81	7.70	7.88	6.98	7.79	7.63	7.76	7.84	7.71	7.65	7.10
Al (T)	0.80	0.83	0.75	0.69	0.35	0.85	0.88	0.25	0.87	0.48	0.63	0.75	0.19	0.30	0.08	1.02	0.21	0.36	0.24	0.16	0.29	0.31	0.90
Ti (T)	0.02	0.01	0.01	0.01	0.00			0.03	0.01	0.00				0.01	0.01			0.01			0.00	0.01	0.00
Ti (C)	0.10	0.12	0.13	0.10	0.03	0.15	0.14		0.15	0.07	0.03	0.11	0.02	0.02		0.18	0.02	0.03	0.01	0.02	0.03		0.14
Al (C)							0.02				0.03	0.01	0.05			0.03	0.01		0.02	0.07			
Cr (C)	0.01	0.01	0.00	0.00			0.00			0.01	0.00	0.01	0.01	0.00	0.01	0.01	0.01	0.01	0.01	0.01			0.01
Fe^{3+} (C)	0.47	0.42	0.41	0.42	0.26	0.41	0.40	0.26	0.41	0.26	0.49	0.40	0.09	0.24	0.10	0.25	0.15	0.24	0.18	0.06	0.21	0.32	0.29
Ni (C)	0.01		0.00							0.01			0.01	0.01	0.00	0.01		0.00			0.00	0.00	
Fe^{2+} (C)	1.15	1.25	1.18	1.20	0.87	0.97	1.24	1.02	0.99	1.02	0.99	1.08	1.72	0.97	1.05	1.43	2.11	1.41	1.72	2.25	0.66	1.59	1.16
Mg (C)	3.27	3.20	3.27	3.27	3.84	3.47	3.21	3.72	3.45	3.64	3.46	3.38	3.12	3.76	3.85	3.09	2.70	3.27	3.07	2.59	4.10	3.09	3.40
Mn^{2+} (B)	0.04	0.04	0.04	0.05	0.06	0.04	0.05	0.05	0.03	0.03	0.05	0.03	0.08	0.04	0.05	0.06	0.07	0.02	0.07	0.08	0.02	0.06	0.04
Fe^{2+} (B)	0.09	0.08	0.08	0.07	0.14	0.08	0.06	0.14	0.08	0.04	0.14	0.09	0.00	0.05	0.03	0.08		0.09			0.06	0.01	0.13
Ca (B)	1.72	1.71	1.70	1.71	1.71	1.71	1.73	1.77	1.71	1.85	1.67	1.72	1.89	1.86	1.91	1.76	1.90	1.96	1.81	1.87	1.86	1.89	1.73
Na (B)	0.15	0.16	0.18	0.17	0.08	0.17	0.16	0.05	0.17	0.08	0.13	0.17	0.03	0.06	0.01	0.09	0.04	0.02	0.03	0.05	0.06	0.04	0.10
Na (A)	0.19	0.25	0.19	0.17	0.08	0.23	0.26	0.05	0.25	0.12	0.13	0.19	0.03	0.06	0.01	0.35	0.04	0.06	0.03	0.02	0.06	0.04	0.32
K (A)	0.08	0.08	0.07	0.06	0.02	0.09	0.09	0.02	0.09	0.04	0.05	0.07	0.01	0.02	0.01	0.10	0.02	0.01	0.01	0.01	0.03	0.02	0.10
OH (W)	1.89	1.85	1.82	1.85	1.80	1.75	1.82	1.94	1.89	1.88	1.98	1.89	1.96	1.88	2.00	1.73	1.92	1.93	2.00	1.99	1.80	1.96	1.70
F (W)	0.11	0.15	0.18	0.15	0.20	0.25	0.18	0.06	0.11	0.12	0.02	0.11	0.04	0.12		0.27	0.08	0.07		0.01	0.20	0.05	0.30
Cl (W)	n.a	n.a	n.a	n.a	n.a	n.a	n.a	n.a	n.a	n.a	n.a	n.a	n.a	n.a	n.a	n.a	n.a	n.a	n.a	n.a	n.a	n.a	n.a
Sum T,C,B,A	15.27	15.33	15.26	15.23	15.10	15.32	15.35	15.07	15.33	15.16	15.19	15.27	15.04	15.07	15.01	15.45	15.05	15.07	15.05	15.03	15.09	15.06	15.42
#Mg	0.72	0.71	0.72	0.72	0.79	0.77	0.71	0.76	0.76	0.77	0.75	0.74	0.64	0.79	0.78	0.67	n.d.	n.d.	0.63	n.d.	0.85	0.66	0.72
T (°C)[c]	772	772	758	747	735	785	778	717	793	715	778	757	646	700	669	808	640	677	669	622	713	681	803
P (kbar)[c]															0.85	0.85							
$(H_2O)^c_{melt}$ (wt%)	3.97	3.78	3.75	3.92	3.2	3.3	3.8	3.3	3.4	3.5	3.8	3.6	4.4	3.4	3.3	4.0	4.9	4.5	4.6	5.1	2.8	4.5	3.4

Sample	36a	36a	36a	36a	36a	36a	36a	36a	36B	36B	36B	36B	36B	36B	37a	37a	38	38	38	38	38	38	38	38	38	38	38
Position[a]	core	rim	rim	int	int	rim	core	core	rim	rim	core	int	rim	int	rim	int	int	int	core	rim	int	int	rim	int	int	rim	core
Run	36A10	36A11	36A16	36A32 (inc)	36A38 (inc)	36A40	36A42	36A43 (inc)	36B2	36B4	36B12	36B18	36B19	36B24	37a1	37a14	385	386	387	388	3812	3813	3817	3820	3826	3828	3829
SiO_2	49.35	51.50	51.85	50.05	50.25	49.36	54.59	50.00	46.72	52.52	47.74	47.76	48.80	48.57	53.51	49.78	50.88	49.90	49.77	54.04	47.01	49.25	49.67	49.85	50.28	50.91	49.03
TiO_2	1.16	0.76	0.61	0.76	0.92	1.10	0.29	0.82	1.75	0.67	1.84	1.70	1.45	1.50	0.32	0.93	0.71	0.98	1.01	0.35	1.86	1.27	0.79	1.05	1.03	0.64	1.06
Al_2O_3	4.97	3.51	3.54	4.20	4.13	4.67	1.34	4.55	6.54	2.84	6.63	6.04	5.72	5.52	1.39	3.89	3.72	4.04	4.04	2.02	7.01	4.80	3.98	4.50	4.27	4.02	5.13
Cr_2O_3		0.09		0.06	0.01		0.10	0.10	0.05	0.01	0.06	0.11		0.10		0.10	0.02	0.09	0.05	0.07	0.04	0.07	0.07		0.03		0.00
FeO	13.99	10.60	9.98	14.21	14.95	14.29	9.24	14.24	12.39	8.11	11.48	12.68	12.37	13.13	12.14	14.16	13.94	13.69	14.29	9.43	11.50	12.19	13.83	12.52	13.71	13.49	14.56
MnO	0.30	0.17	0.27	0.31	0.34	0.30	0.21	0.32	0.26	0.13	0.20	0.16	0.26	0.25	0.14	0.38	0.29	0.33	0.37	0.29	0.11	0.22	0.37	0.16	0.27	0.34	0.28
MgO	14.88	17.27	18.05	15.08	15.55	15.41	19.35	15.50	15.76	19.15	16.20	15.32	15.65	15.42	17.01	15.09	15.08	15.17	14.72	18.84	15.55	16.19	15.08	15.77	15.18	15.66	14.28
NiO	0.07		0.07	0.04		0.10			0.01	0.04			0.04		0.05		0.02	0.04	0.05	0.04	0.03	0.04	0.05	0.05	0.09		0.00

(*continued on next page*)

Table 5 (*continued*)

Sample	36a	36a	36a	36a	36a	36a	36a	36a	36B	36B	36B	36B	36B	36B	37a	37a	38	38	38	38	38	38	38	38	38	38	38
Position[a]	core	rim	rim	int	int	rim	core	core	rim	rim	core	int	rim	int	rim	int	int	int	core	rim	int	int	rim	int	int	rim	core
Run	36A10	36A11	36A16	36A32 (inc)	36A38 (inc)	36A40	36A42	36A43 (inc)	36B2	36B4	36B12	36B18	36B19	36B24	37a1	37a14	385	386	387	388	3812	3813	3817	3820	3826	3828	3829
CaO	11.01	11.67	11.27	11.03	10.94	10.80	11.73	10.90	11.07	12.12	10.98	11.00	11.19	11.09	11.70	10.90	10.93	10.81	10.81	12.25	10.99	11.02	10.81	11.04	10.91	10.78	10.99
Na_2O	1.20	0.82	0.81	0.90	0.94	1.20	0.45	1.11	1.78	0.71	1.83	1.67	1.54	1.44	0.53	1.38	1.06	1.16	1.13	0.55	1.99	1.36	0.94	1.20	1.14	1.05	1.43
K_2O	0.43	0.36	0.26	0.38	0.36	0.41	0.13	0.37	0.56	0.23	0.52	0.51	0.50	0.49	0.19	0.34	0.27	0.35	0.34	0.12	0.63	0.46	0.30	0.39	0.31	0.29	0.46
F	0.49	0.93	0.65	0.25	0.08	0.43	0.38	0.49	0.55	0.56	0.55	0.85	0.38	0.67	0.77	1.38	0.07	0.22	0.23	0.07	0.16	0.36	0.16	0.04	0.07	0.34	0.15
Total	97.85	97.68	97.36	97.27	98.46	98.06	97.81	98.38	97.43	97.10	98.02	97.79	97.90	98.17	97.74	98.32	96.99	96.78	96.80	98.06	96.87	97.23	96.03	96.57	97.29	97.53	97.37
Si (T)[b]	7.18	7.41	7.42	7.29	7.22	7.14	7.71	7.21	6.82	7.47	6.91	6.99	7.06	7.05	7.71	7.28	7.40	7.27	7.27	7.60	6.89	7.15	7.31	7.26	7.27	7.37	7.18
Al (T)	0.82	0.59	0.58	0.71	0.70	0.80	0.22	0.77	1.13	0.48	1.09	1.01	0.94	0.94	0.24	0.67	0.60	0.69	0.70	0.33	1.11	0.82	0.69	0.74	0.73	0.64	0.83
Ti (T)					0.08	0.06	0.03	0.02	0.05	0.05				0.01	0.03	0.05		0.04	0.03	0.04		0.03			0.00		
Ti (C)	0.13	0.08	0.07	0.08	0.02	0.06		0.07	0.14	0.02	0.20	0.19	0.16	0.15		0.05	0.08	0.07	0.08		0.21	0.11	0.09	0.12	0.11	0.07	0.12
Al (C)	0.03	0.00	0.01	0.01							0.05	0.04	0.04				0.04				0.10		0.00	0.03		0.05	0.06
Cr (C)		0.01		0.01	0.00		0.01	0.01	0.01	0.00	0.01	0.01		0.01		0.01	0.00	0.01	0.01	0.01	0.01	0.01	0.01		0.00		
Fe^{3+} (C)	0.44	0.34	0.39	0.45	0.59	0.60	0.23	0.55	0.51	0.35	0.29	0.26	0.37	0.43	0.22	0.44	0.39	0.61	0.59	0.33	0.22	0.45	0.44	0.40	0.58	0.41	0.38
Ni (C)	0.01		0.01	0.01		0.01			0.00	0.01			0.01		0.01		0.00	0.00	0.01	0.00	0.00	0.01	0.01	0.01	0.01		
Fe^{2+} (C)	1.17	0.87	0.67	1.17	1.06	1.01	0.69	1.04	0.91	0.56	0.97	1.16	1.05	1.07	1.12	1.21	1.22	1.02	1.11	0.71	1.08	0.93	1.14	1.03	1.03	1.09	1.33
Mg (C)	3.23	3.70	3.85	3.27	3.33	3.32	4.07	3.33	3.43	4.06	3.50	3.34	3.38	3.33	3.65	3.29	3.27	3.29	3.20	3.95	3.40	3.50	3.31	3.42	3.27	3.38	3.12
Mn^{2+} (B)	0.04	0.02	0.03	0.04	0.04	0.04	0.03	0.04	0.03	0.02	0.02	0.02	0.03	0.03	0.02	0.05	0.04	0.04	0.05	0.04	0.01	0.03	0.05	0.02	0.03	0.04	0.03
Fe^{2+} (B)	0.09	0.07	0.13	0.12	0.15	0.12	0.14	0.13	0.09	0.06	0.14	0.13	0.07	0.09	0.10	0.08	0.09	0.04	0.04	0.04	0.11	0.10	0.12	0.10	0.05	0.13	0.07
Ca (B)	1.72	1.80	1.73	1.72	1.68	1.68	1.78	1.68	1.73	1.85	1.70	1.73	1.73	1.72	1.81	1.71	1.70	1.69	1.69	1.85	1.72	1.71	1.70	1.72	1.69	1.67	1.72
Na (B)	0.16	0.11	0.11	0.13	0.13	0.17	0.06	0.15	0.14	0.08	0.13	0.12	0.16	0.15	0.07	0.17	0.17	0.23	0.22	0.08	0.15	0.16	0.13	0.16	0.22	0.16	0.17
Na (A)	0.18	0.12	0.11	0.13	0.13	0.17	0.06	0.16	0.36	0.12	0.38	0.35	0.28	0.25	0.08	0.22	0.13	0.10	0.10	0.08	0.42	0.23	0.14	0.18	0.09	0.14	0.24
K (A)	0.08	0.07	0.05	0.07	0.07	0.08	0.02	0.07	0.10	0.04	0.10	0.10	0.09	0.09	0.03	0.06	0.05	0.07	0.06	0.02	0.12	0.09	0.06	0.07	0.06	0.05	0.09
OH (W)	1.77	1.58	1.71	1.88	1.96	1.80	1.83	1.78	1.75	1.75	1.75	1.61	1.83	1.69	1.65	1.36	1.97	1.90	1.89	1.97	1.93	1.83	1.93	1.98	1.97	1.85	1.93
F (W)	0.23	0.42	0.29	0.12	0.04	0.20	0.17	0.23	0.25	0.25	0.25	0.40	0.17	0.31	0.35	0.64	0.03	0.10	0.11	0.03	0.08	0.17	0.07	0.02	0.03	0.16	0.07
Cl (W)	n.a	n.a	n.a	n.a	n.a	n.a	n.a	n.a	n.a	n.a	n.a	n.a	n.a	n.a	n.a	n.a	n.a	n.a	n.a	n.a	n.a	n.a	n.a	n.a	n.a	n.a	n.a
Sum T,C,B, A	15.26	15.19	15.16	15.20	15.20	15.25	15.09	15.22	15.47	15.16	15.48	15.44	15.37	15.34	15.11	15.29	15.18	15.17	15.16	15.10	15.53	15.31	15.19	15.25	15.15	15.19	15.32
#Mg	0.72	0.80	0.83	0.72	0.73	0.75	0.83	0.74	0.77	0.87	0.76	0.72	0.75	0.74	0.75	0.72	0.71	0.76	0.74	0.84	0.74	0.77	0.72	0.75	0.75	0.73	0.69
T (°C)[c]	760	740	778	754	796	812	728	801	861	755	833	812	789	802	701	786	718	749	745	729	826	792	780	751	739	740	751
P (kbar)[c]									0.95		0.96	0.84	0.77	0.74							1.08						
$(H_2O)^c_{melt}$ (wt%)	3.95	3.30	3.24	4.04	3.52	3.39	2.61	3.68	3.56	2.64	3.38	3.52	3.45	3.71	2.9	3.19	3.92	3.86	4.01	3.01	3.11	3.42	3.9	3.56	3.97	3.85	3.77

inc: phase included in Pl or Fe—Ti oxide

[a]Position represent the relative position of spot analyses within the crystal: int — intermediate between core and border.

[b]Structural amphibole formula was calculated according to Locock (2014).

[c]Pressure, temperature and melt water content obtained by Amp thermobarometry from Ridolfi et al. (2010).

Table 6
Microprobe analyses of pyroxenes from the Cerro Munro enclaves.

Phase	Cpx	Cpx	Cpx	Cpx	Cpx	Cpx	Cpx	Cpx	Cpx	Cpx	Cpx	Cpx	Cpx	Cpx	Cpx	Cpx	Cpx	Cpx	Cpx	Cpx	Cpx	Cpx	Cpx	Cpx	Opx
Sample	36a	36a	36a	36a	36a	36a	36a	36a	36a	36a	36a	36a	36a	36a	36a	36B	36B	36B	37a	37a	37a	37a	37a	37a	37a	37a
Run	36A-3	36A-13	36A-14	36A-15	36A-22	36A-23	36A-24	36A-25	36A-28	36A-29	36A-30	36A-31	36A-39	36A-47	36B-1	36B-10	36B-11	37a-2	37a-7	37a-10	37a-11	37a-15	37a-19	37a-20	37a-12
Position[a]	inc	core	rim	core	core						core		core, inc	rim, inc	core				inc	core	rim	inc	core	rim	inc
SiO_2	51.29	52.99	51.93	53.11	52.56	52.56	51.96	53.21	53.30	52.58	52.64	52.15	52.43	51.60	51.94	52.64	52.28	53.54	51.97	52.07	53.47	52.82	53.38	52.40	52.70
TiO_2	0.65	0.03	0.16	0.06	0.13	0.10	0.21	0.08	0.09	0.12	0.13	0.21	0.09	0.41	0.21	0.15	0.16	0.06	0.33	0.12	0.05	0.30	0.09	0.21	0.21
Al_2O_3	1.84	0.40	0.74	0.17	0.75	0.14	1.12	0.44	0.37	0.96	0.81	0.94	0.48	1.91	0.78	1.16	0.98	0.34	1.17	0.85	0.33	1.09	0.38	1.11	0.57
Cr_2O_3	0.09	0.01	n.d.	0.10	n.d.	0.01	0.08	0.10	0.02	0.04	0.05	0.06	0.05	0.12	0.10	n.d.	0.16	n.d.	0.03	n.d.	n.d.	n.d.	n.d.	0.09	0.07
FeO	9.50	6.65	10.44	8.32	10.22	10.20	9.92	6.20	6.34	7.99	8.40	9.06	10.02	7.64	8.77	7.06	8.06	7.37	9.41	8.83	7.32	9.49	7.47	9.18	21.86
MnO	0.34	0.22	0.32	0.29	0.35	0.34	0.29	0.27	0.14	0.13	0.31	0.28	0.38	0.21	0.27	0.23	0.35	0.24	0.30	0.30	0.32	0.36	0.27	0.26	0.71
MgO	14.22	15.51	13.95	14.60	13.71	13.59	13.38	15.50	15.45	14.30	14.50	14.68	14.35	15.47	14.90	14.92	15.29	15.05	14.78	14.48	15.53	14.47	15.16	13.88	22.60
NiO	0.11	0.03	0.02	0.06	0.05	0.01	0.10	0.01	n.d.	0.01	0.09	0.04	0.08	0.06	0.03	0.05	0.03	n.d.	0.04	0.07	0.04	n.d.	0.02	n.d.	0.02
CaO	21.07	23.20	21.47	22.95	21.67	22.30	22.06	23.46	23.55	23.09	22.20	21.30	21.66	21.93	21.60	23.04	21.95	22.89	20.90	21.56	22.76	21.30	22.82	22.21	1.09
Na_2O	0.46	0.28	0.28	0.14	0.21	0.13	0.31	0.23	0.23	0.31	0.32	0.26	0.34	0.31	0.40	0.31	0.39	0.28	0.46	0.44	0.31	0.43	0.36	0.50	0.03
K_2O	0.02	0.02	n.d.	0.02	0.01	0.01	n.d.	0.01	0.00	n.d.	n.d.	0.02	0.01	0.01	n.d.	0.01	0.01	0.01	n.d.	0.01	0.01	0.00	0.01	0.00	0.00
F	n.d.	0.03	0.06	n.d.	0.07	n.d.	0.19	n.d.	n.d.	n.d.	0.09	0.24	n.d.	n.d.	0.22	0.02	n.d.	0.11	0.03	0.10	0.03	0.06	n.d.	0.08	n.d.
Total	99.61	99.51	99.38	99.85	99.76	99.40	99.61	99.55	99.55	99.61	99.53	99.26	99.91	99.79	99.27	99.60	99.72	99.98	99.50	98.91	100.16	100.37	99.99	99.96	99.95
#Mg[b]	0.73	0.81	0.70	0.76	0.71	0.70	0.71	0.82	0.81	0.76	0.75	0.74	0.72	0.78	0.75	0.79	0.77	0.78	0.74	0.75	0.79	0.73	0.78	0.73	0.65

Phase	Cpx	Cpx	Cpx	Cpx	Cpx	Opx	Opx	Opx	Opx
Sample	37	38	38	38	38	38	38	38	38
Run	38–1	38–11	38–16	38–22	38–25	38–2	38–15	38–21	38–27
Position[a]	int	relic core		inc		inc		inc	relic core
SiO_2	51.80	53.14	52.42	52.81	52.43	52.56	52.87	53.04	53.60
TiO_2	0.26	0.09	0.35	0.26	0.41	0.23	0.19	0.21	0.14
Al_2O_3	1.10	0.43	1.18	0.87	1.45	0.61	0.66	0.63	0.45
Cr_2O_3	n.d.	0.03	0.13	0.01	0.08	0.01	0.03	0.02	n.d.
FeO	8.80	8.25	9.65	9.02	8.75	23.34	22.76	21.89	21.57
MnO	0.41	0.26	0.29	0.31	0.29	0.84	0.67	0.55	0.57
MgO	14.67	14.15	13.70	14.25	14.56	21.50	21.81	22.28	22.65
NiO	0.01	0.02	0.04	n.d.	0.02	0.04	n.d.	n.d.	0.02
CaO	21.18	22.96	21.73	21.33	21.60	1.11	1.24	1.40	1.13
Na_2O	0.48	0.34	0.43	0.37	0.44	0.03	0.03	0.03	0.03
K_2O	n.d.	0.02	n.d.	n.d.	n.d.	0.00	0.01	0.01	0.02
F	0.07	n.d.	n.d.	0.07	n.d.	n.d.	n.d.	n.d.	0.17
Total	98.82	99.73	99.94	99.33	100.1	100.3	100.3	100.1	100.5
#Mg[b]	0.75	0.75	0.72	0.74	0.75	0.62	0.63	0.64	0.65

inc: phase included in Pl.
[a]Position represent the relative position of spot analyses within the crystal: int — intermediate between core and border; inc — inclusion.
[b]Mg# = molar MgO/[MgO+ FeO].
n.d.: not determined.

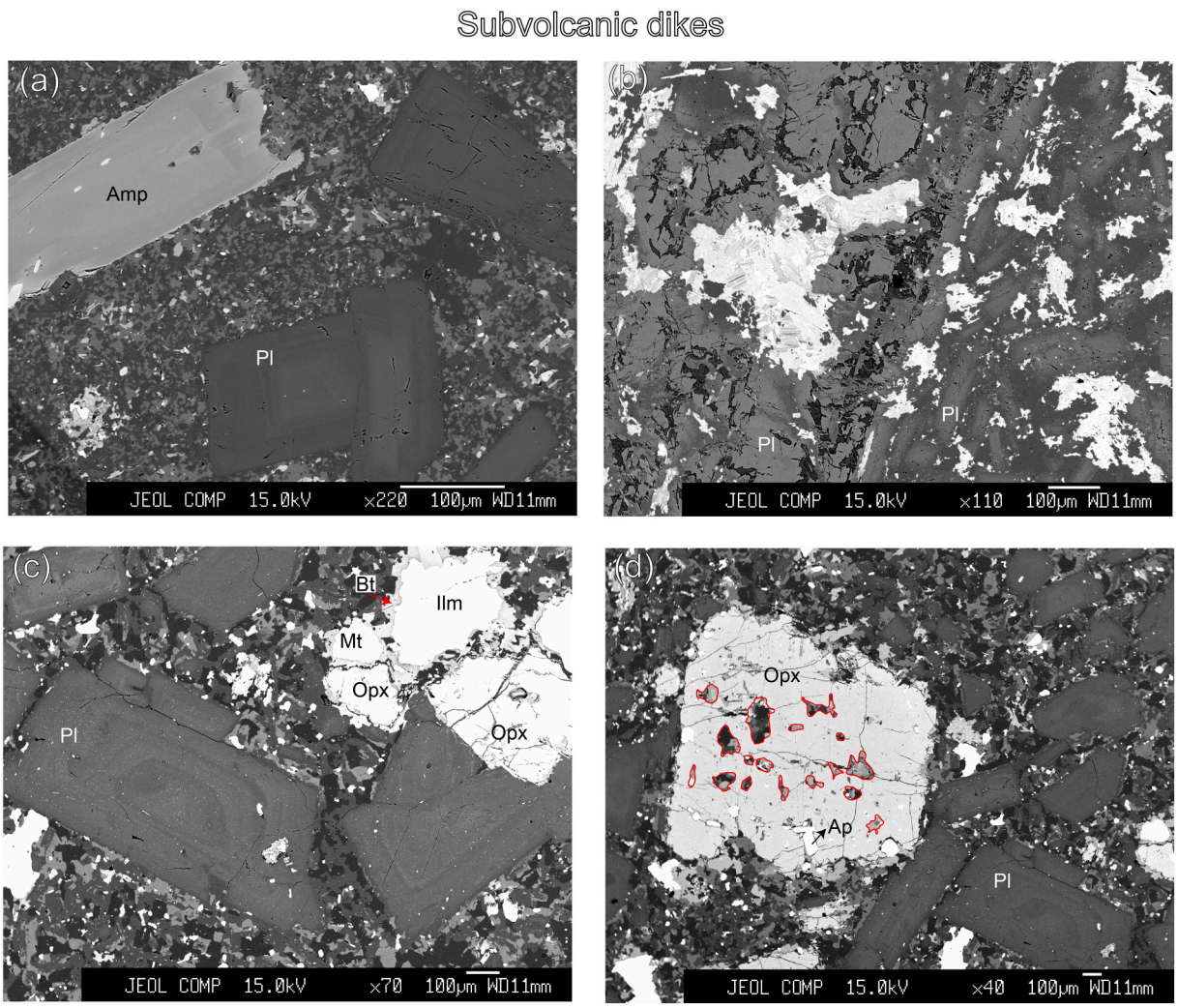

Fig. 6. BSE images of subvolcanic dikes of Cerro Munro magmatic system. (a) Dacitic porphyry dike MUN19–3 showing Amp and Pl phenocrysts in an abundant matrix composed of Pl, Amp, Kfs and Qz. (b) Dacitic annular dike MUN19–5 showing Pl as phenocrysts and microlites. (c) Andesitic porphyry dike MUN19–2 with Opx, Fe—Ti oxides and Pl as phenocrysts. (d) Opx phenocryst from andesite MUN19–2 with crystallized melt pools with Qz, Amp, Fe—Ti oxides and Pl.

Differentiated rhyolitic dikes, rich in K_2O, Rb and other incompatible elements, represent more evolved liquids (Fig. 11). The melt water content (4.9 wt%; Table 8) of dacites when the Amp crystallizes indicates saturation in the dacites at subvolcanic pressure (Burnham, 1979). Melts with fractionated composition may have been expelled from the plutonic system when the water saturation is reached justifying the enrichment in highly incompatible elements as Li, Rb, Nb and Ta (Table 10). Andesitic dikes plot between tonalites and enclaves and may represent new pristine magmatic inputs to the almost crystallized magmatic chamber (Fig. 11).

The flat pattern observed in the Mg# vs MgO (wt%) diagram (Fig. 9d) should be explained by FeO depletion for the Mg-poorer samples. As that the MgO content evolves, decreasing with fractionation, according the calc-alkaline trend (Fig. 9d), only an FeO depletion justifies the constant Mg number for more evolved terms. The fractionation of Fe oxides (Ilm and Ti—Mt), hosted as inclusions in Cpx (Fig. 4h), maintains a high Mg# as magnesium decreases (Fig. 9d). The fractionation of Opx, Cpx and Fe oxides, mafic mineral phases that differentiate the mineral compositions of enclaves regarding to the host tonalites (Fig. 4), increase the MME basicity, displacing the trend from the MCA (Fig. 11f) since the Mg content of the magma is greater than what is expected, due to the Opx involvement (Fig. 11d). However, the Cerro Munro tonalites may be the result of a fractionation process following a mixing line (dashed line in Fig. 11f) between the rhyolite dike (residual liquid) and the andesitic dike (parental magma).

Clinopyroxene (or Amp) and Pl fractionation is also indicated by the concave REE patterns and negative *Eu* anomalies observed in enclaves and tonalites (Fig. 10). Almost parallel REE trends described by the MME-tonalite paired samples implies a common early evolution of both magmatic products. However, some tonalite samples display significant positive *Eu* anomalies, implying that after the separation of the early crystallized MME, the tonalitic magma evolved through the crystallization of Pl, and probably the reaction of previously crystallized anhydrous mafic minerals with a water-rich residual liquid (inclusions of Cpx and Hbl aggregates) (Fig. 4), to constitute a Hbl- and Pl-rich solid assemblage. Therefore, where are the felsic counterparts, i.e. residual liquids, of the early crystallized mafic enclaves and the slightly more evolved tonalites, i.e. cumulate-like crystal-rich mushes?

In-situ fractionation processes are described in magmatic reservoirs emplaced at deeper crustal levels, where less and more evolved magmas finally derive from a common source (Bachmann and Huber, 2016; Xu et al., 2021). In turn, the shallow Cerro Munro pluton is formed by mainly tonalitic facies (besides MMEs) and abundant radial porphyritic dikes. The observed geochemical and textural relations, compared with dynamic crystallization experiments within thermal gradients (Rodríguez and Castro, 2017) point to a mechanism of differentiation by gas-driven filter pressing and, consequently, compositional magma splitting (Castro et al., 2021; Xu et al., 2021), which is discussed in the next

Table 7
Microprobe analyses of plagioclases from the Cerro Munro subvolcanic rocks.

Sample	MUN19–2	MUN19–2	MUN19–2	MUN19–2	MUN19–2	MUN19–2	MUN19–2	MUN19–2	MUN19–3	MUN19–3	MUN19–3	MUN19–3	MUN19–3	MUN19–3	MUN19–3	MUN19–3	MUN19–3
Run	M19 2 17	M19 2 18	M19 2 19	M19 2 20	M19 2 21	M19 2 22	M19 2 27	M19 2 28	M19 3 18	M19 3 19	M19 3 20	M19 3 21	M19 3 22	M19 3 23	M19 3 24	M19 3 29	M19 3 30
Position	core	core	int	int	int	rim	matrix	core (matrix)	core	int	rim	core	int	rim	rim (matrix)	core (matrix)	core (matrix)
SiO_2	58.86	55.69	57.06	59.20	56.61	63.32	64.08	60.59	56.25	63.37	63.54	57.32	61.48	62.26	65.70	61.26	62.45
TiO_2	0.07		0.01		0.25	0.04	0.06	0.04	0.06		0.03	0.01	0.02	0.04	0.06	0.04	
Al_2O_3	26.48	28.38	27.77	26.55	27.81	23.47	23.05	25.42	27.50	23.22	23.32	26.61	23.87	23.87	22.88	25.34	23.89
FeO	0.18	0.14	0.18	0.22	0.20	0.23	0.24	0.24	0.44	0.30	0.25	0.31	0.26	0.32	0.23	0.12	0.33
MgO		0.01			0.02	0.02	0.01			0.02	0.02	0.03			0.02	0.00	
MnO	0.00				0.05			0.03	0.01	0.02	0.06	0.02	0.02	0.03	0.00		
CaO	7.45	9.78	8.82	7.45	8.73	3.96	3.61	6.27	9.30	3.91	3.79	8.31	4.91	4.88	2.45	5.41	4.46
Na_2O	6.88	5.75	6.30	7.01	6.18	9.18	9.08	7.73	6.18	9.12	9.07	6.74	8.61	8.70	10.18	8.62	9.05
K_2O	0.48	0.32	0.34	0.44	0.30	0.45	0.44	0.26	0.13	0.31	0.26	0.15	0.29	0.26	0.52	0.11	0.27
SrO	0.11	0.08	0.11	0.08	0.08	0.02	0.01	0.02	0.03	0.04	0.06	0.06	0.05	0.08	0.03	0.05	0.02
Total	100.6	100.1	100.6	100.9	100.2	100.7	100.6	100.6	99.9	100.4	100.4	99.6	99.5	100.5	102.1	100.9	100.5
X_{An}	36.41	47.55	42.77	36.05	43.07	18.76	17.58	30.49	45.08	18.83	18.48	40.17	23.57	23.29	11.39	25.60	21.08
X_{Ab}	60.79	50.62	55.28	61.44	55.16	78.70	79.88	68.01	54.19	79.43	79.99	58.95	74.76	75.21	85.71	73.79	77.43
X_{Or}	2.80	1.84	1.95	2.52	1.77	2.53	2.54	1.50	0.73	1.75	1.53	0.89	1.67	1.50	2.90	0.60	1.49

Sample	MUN19–3	MUN19–3	MUN19–3	MUN19–3	MUN19–3	MUN19–3	MUN19–5	MUN19–5	MUN19–5	MUN19–5	MUN19–5	MUN19–5	MUN19–5	MUN19–5	MUN19–5	MUN19–5	MUN19–5
Run	M19 3 49	M19 3 50	M19 3 51	M19 3 52	M19 3 53	M19 3 54	M19 5 1	M19 5 2	M19 5 3	M19 5 4	M19 5 5	M19 5 7	M19 5 9	M19 5 10	M19 5 11	M19 5 16	M19 5 17
Position	core	int	int	int	int	rim	core		core	core		matrix	core	int	rim	rim (matrix)	core (matrix)
SiO_2	54.75	57.94	56.67	59.44	56.99	61.04	52.74	52.74	52.59	51.41	53.76	60.93	52.72	53.10	60.65	65.85	61.23
TiO_2	0.06	0.08	0.10	0.09	0.03	0.01	0.08	0.05	0.05	0.08	0.01	0.06	0.03	0.06	0.02		0.05
Al_2O_3	28.55	26.66	27.77	25.34	26.59	24.61	30.32	30.22	30.05	30.97	29.13	24.82	29.90	30.19	24.77	22.22	24.38
FeO	0.46	0.40	0.42	0.60	0.48	0.40	0.39	0.43	0.44	1.38	0.44	0.43	0.49	0.49	0.36	0.21	0.38
MgO	0.04	0.02	0.01	0.07	0.08	0.07	0.09	0.13	0.13	0.25	0.08	0.05	0.09	0.05	0.02		0.03
MnO	0.04	0.02	0.01	0.01		0.04			0.03					0.00		0.02	
CaO	10.83	8.48	9.65	6.81	8.29	5.54	12.82	12.64	12.62	9.58	11.35	5.67	12.33	12.52	6.02	1.92	5.71
Na_2O	5.15	6.45	5.80	7.40	6.70	8.11	4.05	4.20	4.14	3.25	4.98	7.78	4.41	4.29	7.77	9.96	8.02
K_2O	0.20	0.37	0.33	0.36	0.26	0.27	0.09	0.15	0.09	0.56	0.17	0.40	0.12	0.10	0.24	0.22	0.26
SrO	0.08	0.06	0.08	0.07	0.08	0.07	0.07	0.12	0.12	0.04	0.09	0.02	0.03	0.03	0.03		0.04
Total	100.1	100.5	100.9	100.2	99.5	100.2	100.6	100.7	100.2	97.5	100.0	100.2	100.1	100.8	99.9	100.4	100.1
X_{An}	53.15	41.19	46.99	33.01	39.99	27.00	63.31	61.92	62.42	59.40	55.19	28.02	60.28	61.36	29.58	9.51	27.80
X_{Ab}	45.72	56.67	51.12	64.89	58.51	71.47	36.18	37.18	37.05	36.46	43.82	69.60	39.02	38.04	69.02	89.17	70.67
X_{Or}	1.14	2.15	1.89	2.10	1.50	1.54	0.51	0.90	0.53	4.15	0.99	2.38	0.69	0.60	1.40	1.32	1.52

Sample	MUN19–5	MUN19–5	MUN19–5	MUN19–5	MUN19–5	MUN19–5	MUN19–5	MUN19–5	MUN19–5	MUN19–5	MUN19–5
Run	M19 5 32	M19 5 33	M19 5 76	M19 5 77	M19 5 78	M19 5 79	M19 5 80	M19 5 81	M19 5 82	M19 5 83	M19 5 88
Position	core	rim	core (matrix)	matrix	rim	int	core	matrix	matrix	core (matrix)	rim (matrix)
SiO_2	54.41	57.49	56.93	65.88	58.08	53.07	50.83	60.72	57.17	58.17	62.76
TiO^2	0.06	0.04	0.03		0.02	0.10	0.02	0.05	0.12	0.03	
Al_2O_3	28.86	26.99	26.93	21.46	25.92	29.17	30.67	24.86	26.79	26.05	21.61
FeO	0.50	0.55	0.46	0.25	0.33	0.76	0.46	0.37	0.45	0.41	0.18
MgO	0.08	0.04				0.10	0.10		0.03	0.02	
MnO	0.06	0.03	0.02		0.02	0.04			0.01	0.01	0.04
CaO	11.18	8.77	8.78	1.68	7.49	11.51	13.41	5.84	8.43	7.70	2.23
Na_2O	5.06	6.47	6.26	10.30	7.09	4.85	3.81	8.09	6.43	6.81	10.07
K_2O	0.15	0.20	0.18	0.12	0.14	0.17	0.12	0.18	0.17	0.21	0.11
SrO	0.08	0.06	0.09	0.03	0.08	0.03	0.07	0.04	0.06	0.07	0.06
Total	100.4	100.6	99.7	99.7	99.2	99.8	99.5	100.2	99.7	99.5	97.1
X_{An}	54.48	42.36	43.19	8.20	36.58	56.20	65.60	28.21	41.57	37.97	10.82
X_{Ab}	44.65	56.49	55.77	91.09	62.63	42.80	33.71	70.73	57.43	60.77	88.57
X_{Or}	0.87	1.15	1.04	0.72	0.79	0.99	0.68	1.06	1.00	1.26	0.61

Table 8
Microprobe analyses of amphiboles from the subvolcanic rocks from Cerro Munro.

Sample	MUN19–2	MUN19–2	MUN19–2	MUN19–2	MUN19–3	MUN19–3	MUN19–3	MUN19–3	MUN19–3	MUN19–3	MUN19–3	MUN19–3	MUN19–3	MUN19–3	MUN19–3	MUN19–3	MUN19–3	MUN19–3	MUN19–3
Run	M19 2 7a	M19 2 9	M19 2 10	M19 2 11	M19 3 1	M19 3 3	M19 3 6	M19 3 7	M19 3 15	M19 3 16	M19 3 17	M19 3 25	M19 3 26	M19 3 31	M19 3 32	M19 3 33	M19 3 34	M19 3 35	M19 3 36
Position	matrix	matrix	inc	inc	rim	int	rim	core	core	int	rim	matrix	matrix	core	int	rim	core	rim	
SiO_2	48.12	53.36	52.05	43.60	50.29	52.45	53.01	52.61	44.54	46.83	51.08	50.70	50.02	50.38	49.90	50.17	47.48	47.15	46.97
TiO_2	1.84	0.61	0.42	2.02	0.33	0.27	0.27	0.31	2.32	1.88	0.92	0.80	0.58	0.29	0.25	0.33	1.58	1.27	1.75
Al_2O_3	6.58	3.28	4.20	9.97	1.56	1.31	1.98	1.45	8.42	7.10	8.87	2.58	3.38	2.05	2.27	2.10	6.25	5.55	6.68
Cr_2O_3	0.00		0.02	0.16	0.02		0.01			0.01	0.02	0.02		0.07	0.03	0.01	0.01		
MnO	0.21	0.19	0.13	0.15	0.48	0.49	0.52	0.57	0.25	0.30	0.42	0.60	0.49	0.54	0.64	0.51	0.27	0.44	0.27
FeO	12.13	9.90	10.19	13.70	19.69	19.09	20.14	19.40	12.38	11.85	14.79	17.90	18.28	20.28	21.00	19.61	12.11	18.63	12.22
MgO	15.60	18.61	18.30	13.83	12.39	12.90	12.76	12.76	15.02	15.63	9.75	13.14	12.28	11.55	11.28	11.92	16.31	11.81	16.11
CaO	11.69	11.47	11.62	11.53	10.34	10.66	10.75	11.09	11.25	11.23	9.60	10.85	11.40	11.59	10.96	11.14	11.23	10.93	11.36
Na_2O	1.47	0.64	1.08	2.03	0.32	0.28	0.42	0.33	2.30	1.97	3.06	0.60	0.76	0.47	0.57	0.42	1.77	1.35	1.77
K_2O	0.66	0.29	0.34	0.96	0.18	0.14	0.16	0.17	0.67	0.79	0.49	0.31	0.39	0.20	0.18	0.16	0.72	0.62	0.77
F									0.13	0.20							0.15	0.02	0.13
Total	98.32	98.34	98.36	97.93	95.61	97.58	100.01	98.68	97.27	97.77	98.98	97.48	97.58	97.41	97.06	96.35	97.88	97.78	98.04
Si (T)[a]	7.28	7.54	7.32	6.40	7.61	7.75	7.66	7.70	6.55	6.83	7.34	7.49	7.40	7.51	7.49	7.54	6.87	7.01	6.80
Al (T)	0.72	0.46	0.68	1.60	0.28	0.23	0.34	0.25	1.45	1.17	0.66	0.45	0.59	0.36	0.40	0.37	1.07	0.97	1.14
Ti (T)					0.04	0.02	0.00	0.03				0.07	0.01	0.03	0.03	0.04	0.07	0.01	0.07
Fe3+ (T)					0.08			0.02						0.09	0.09	0.05			
Ti (C)	0.21	0.07	0.04	0.22		0.01	0.03		0.26	0.21	0.10	0.02	0.06				0.11	0.13	0.13
Al (C)	0.46	0.09	0.02	0.12					0.01	0.05	0.84								
Cr (C)			0.00	0.02	0.00		0.00			0.00	0.00	0.00		0.01	0.00	0.00	0.00		
Fe^{3+} (C)			0.48	0.46	0.31	0.19	0.25	0.23	0.40	0.23		0.34	0.39	0.41	0.45	0.39	0.50	0.48	0.50
Fe^{2+} (C)	0.82	0.92	0.62	1.15	1.89	1.96	1.97	1.98	1.05	1.12	1.78	1.74	1.85	2.02	2.03	1.94	0.88	1.77	0.90
Mg (C)	3.52	3.92	3.84	3.03	2.80	2.84	2.75	2.78	3.29	3.40	2.09	2.89	2.71	2.57	2.52	2.67	3.52	2.62	3.47
Mn^{2+} (B)	0.03	0.02	0.02	0.02	0.06	0.06	0.06	0.07	0.03	0.04		0.07	0.06	0.07	0.08	0.07	0.03	0.06	0.03
Fe^{2+} (B)	0.72	0.25	0.10	0.07	0.22	0.21	0.21	0.14	0.08	0.10		0.12	0.03	0.01	0.08	0.08	0.09	0.07	0.08
Ca (B)	1.25	1.73	1.75	1.81	1.68	1.69	1.67	1.74	1.77	1.75	1.48	1.72	1.81	1.85	1.76	1.79	1.74	1.74	1.76
Na (B)			0.13	0.10	0.05	0.04	0.06	0.05	0.12	0.11	0.52	0.09	0.10	0.07	0.08	0.06	0.14	0.14	0.13
Ca (A)	0.64	0.01																	
Na (A)	0.43	0.18	0.16	0.48	0.05	0.04	0.06	0.05	0.53	0.44	0.33	0.09	0.12	0.07	0.08	0.06	0.36	0.25	0.37
K (A)	0.13	0.05	0.06	0.18	0.04	0.03	0.03	0.03	0.13	0.15	0.09	0.06	0.07	0.04	0.04	0.03	0.13	0.12	0.14
OH (W)		2.00	2.00	2.00	2.00	2.00	2.00	2.00	1.94	1.91	2.00	2.00	2.00	2.00	2.00	2.00	1.93	1.99	1.94
F (W)									0.06	0.09							0.07	0.01	0.06
Sum T,C,B,A	16.20	15.24	15.22	15.66	15.08	15.06	15.09	15.08	15.66	15.59	15.28	15.14	15.19	15.11	15.12	15.09	15.49	15.37	15.51
T (°C)[b]	814		792	910	720	676	694	682	903	847		731	704	706	716	706	859	781	871
P (kbar)[b]	0.95			2.25					1.54	1.09							0.88	0.78	0.97
$(H_2O)^b_{melt}$ (wt%)	3.37		3.13	4.10	4.44	4.3	4.61	4.42	3.46	2.83		4.03	4.64	4.89	4.94	4.86	3.01	4.48	3.06

Sample	MUN19–3	MUN19–3	MUN19–3	MUN19–3	MUN19–3	MUN19–3	MUN19–3	MUN19–3	MUN19–3	MUN19–3	MUN19–5	MUN19–5	MUN19–5	MUN19–5	MUN19–5	MUN19–5	MUN19–5	MUN19–5	MUN19–5
Run	M19 3 42	M19 3 43	M19 3 44	M19 3 45	M19 3 48	M19 3 39	M19 3 40	M19 3 41	M19 3 46	M19 3 47	M19 5 12	M19 5 13	M19 5 18	M19 5 20	M19 5 23	M19 5 25	M19 5 26	M19 5 27	M19 5 29
Position		core	rim	rim							matrix	matrix	matrix	rim		rim	core	rim	core
SiO_2	53.02	52.14	51.93	50.93	42.69	52.39	52.00	52.46	51.82	51.81	51.31	50.69	52.18	51.01	50.68	50.71	50.58	50.33	50.15
TiO_2	0.11	0.19	0.15	0.19	1.99	0.08	0.14	0.14	0.09	0.10	0.32	0.33	0.18	0.37	0.31	0.25	0.34	0.41	0.32
Al_2O_3	0.86	1.16	1.16	1.79	9.22	0.30	0.31	0.60	0.35	0.29	3.42	3.26	2.25	3.41	3.37	3.30	3.49	3.41	3.50
Cr_2O_3	0.07	0.05	0.07	0.02	0.04		0.04			0.03		0.01	0.01		0.02	0.01		0.04	0.02
MnO	0.33	0.48	0.48	0.51	0.34	1.09	1.12	1.09	1.13	1.09	0.62	0.54	0.70	0.56	0.61	0.54	0.65	0.53	0.59
FeO	17.01	19.36	18.86	19.93	22.61	29.25	29.09	24.05	29.76	30.60	19.34	19.98	19.23	19.74	19.87	19.89	19.76	19.97	19.99
MgO	14.19	13.60	13.62	12.79	7.93	13.85	13.24	17.04	13.33	13.08	10.71	10.43	11.66	10.89	11.11	11.09	10.85	11.03	10.91
CaO	11.55	10.06	10.64	10.27	10.91	1.00	1.04	1.32	1.19	0.99	11.18	11.77	10.95	11.11	11.04	11.00	11.03	11.07	11.10
Na_2O	0.20	0.23	0.23	0.35	2.04	0.05	0.05	0.13	0.04	0.05	0.36	0.36	0.39	0.61	0.56	0.69	0.61	0.66	0.63
K_2O	0.07	0.13	0.11	0.18	0.61		0.01	0.03	0.00	0.01	0.32	0.28	0.18	0.27	0.28	0.22	0.30	0.27	0.27
F					0.00		0.00	0.03	0.02										

(*continued on next page*)

Table 8 (*continued*)

Sample	MUN19–3	MUN19–3	MUN19–3	MUN19–3	MUN19–3	MUN19–3	MUN19–3	MUN19–3	MUN19–3	MUN19–3	MUN19–5	MUN19–5	MUN19–5	MUN19–5	MUN19–5	MUN19–5	MUN19–5	MUN19–5	MUN19–5
Run	M19 3 42	M19 3 43	M19 3 44	M19 3 45	M19 3 48	M19 3 39	M19 3 40	M19 3 41	M19 3 46	M19 3 47	M19 5 12	M19 5 13	M19 5 18	M19 5 20	M19 5 23	M19 5 25	M19 5 26	M19 5 27	M19 5 29
Position		core	rim	rim							matrix	matrix	matrix	rim		rim	core	rim	core
Total	97.41	97.39	97.25	96.96	98.37	98.02	97.04	96.87	97.74	98.05	97.58	97.66	97.72	97.98	97.83	97.70	97.61	97.72	97.49
Si (T)[a]	7.77	7.70	7.67	7.59	6.50	8.35	8.35	8.39	8.30	8.29	7.64	7.57	7.73	7.56	7.53	7.54	7.53	7.49	7.48
Al (T)	0.15	0.20	0.20	0.31	1.50						0.37	0.43	0.27	0.44	0.47	0.46	0.47	0.51	0.52
Ti (T)	0.01	0.02	0.02	0.02															
Fe3+ (T)	0.07	0.08	0.11	0.08															
Ti (C)					0.23	0.01	0.02	0.02	0.01	0.01	0.04	0.04	0.02	0.04	0.03	0.03	0.04	0.05	0.04
Al (C)					0.15	0.06	0.06	0.11	0.07	0.05	0.24	0.14	0.12	0.16	0.12	0.12	0.15	0.09	0.10
Cr (C)	0.01	0.01	0.01	0.00	0.01		0.01			0.00		0.00	0.00		0.00	0.00		0.01	0.00
Fe^{3+} (C)	0.20	0.25	0.29	0.36	0.41						0.06	0.16	0.11	0.19	0.24	0.27	0.22	0.28	0.29
Fe^{2+} (C)	1.69	1.75	1.71	1.80	2.41	3.90	3.91	3.21	3.99	4.10	2.29	2.34	2.17	2.20	2.15	2.13	2.19	2.13	2.14
Mg (C)	3.10	2.99	3.00	2.84	1.80	0.26	0.27	0.26	0.27	0.26	2.38	2.32	2.58	2.41	2.46	2.46	2.41	2.45	2.43
Mn^{2+} (B)	0.04	0.06	0.06	0.07	0.04	1.09	1.06	0.91	1.14	1.20	0.08	0.07	0.09	0.07	0.08	0.07	0.08	0.07	0.08
Fe^{2+} (B)	0.12	0.32	0.22	0.25	0.06						0.06		0.10	0.05	0.08	0.07	0.05	0.07	0.06
Ca (B)	1.81	1.59	1.68	1.64	1.78	0.17	0.18	0.23	0.20	0.17	1.78	1.88	1.74	1.77	1.76	1.75	1.76	1.76	1.78
Na (B)	0.03	0.03	0.03	0.05	0.12	0.02	0.02	0.04	0.01	0.02	0.09	0.05	0.08	0.11	0.08	0.11	0.10	0.10	0.09
Ca (A)																			
Na (A)	0.03	0.03	0.03	0.05	0.48						0.02	0.05	0.04	0.06	0.08	0.09	0.07	0.09	0.09
K (A)	0.01	0.02	0.02	0.03	0.12		0.00	0.01	0.00	0.00	0.06	0.05	0.03	0.05	0.05	0.04	0.06	0.05	0.05
OH (W)	2.00	2.00	2.00	2.00	2.00	2.00	2.00	1.99	1.99	2.00	2.00	2.00	2.00	2.00	2.00	2.00	2.00	2.00	2.00
F (W)					0.00		0.00	0.02	0.01										
Sum T,C,B,A	15.04	15.06	15.05	15.09	15.60	14.63	14.61	14.57	14.66	14.68	15.08	15.11	15.07	15.12	15.13	15.13	15.13	15.14	15.14
T (°C)[b]	681	720	721	727							671	659	656	668	676	667	673	674	675
P (kbar)[b]																			
$(H_2O)^{b}_{melt}$ (wt%)	4.18	4.15	4.29	4.42								5.93	4.82	5.49	5.19	5.29	5.40	5.16	5.33

Sample	MUN19–5	MUN19–5	MUN19–5	MUN19–5	MUN19–5	MUN19–5	MUN19–5	MUN19–5	MUN19–5	MUN19–5	MUN19–5	MUN19–5	MUN19–5	MUN19–5	MUN19–5	MUN19–5	MUN19–5	MUN19–5	MUN19–5
Run	M19 5 30	M19 5 31	M19 5 34	M19 5 40	M19 5 41	M19 5 42	M19 5 44	M19 5 45	M19 5 46	M19 5 47	M19 5 48	M19 5 49	M19 5 50	M19 5 51	M19 5 52	M19 5 53	M19 5 54	M19 5 55	M19 5 56
Position	int	rim	matrix	rim	core	core	rim	int	int	core	core	int	rim	int	matrix	rim	rim	core	non altered
SiO_2	50.48	51.92	50.34	51.63	52.91	49.29	50.72	51.11	51.65	48.93	48.69	50.42	51.13	48.82	51.23	50.70	49.85	50.14	49.82
TiO_2	0.34	0.07	0.43	0.29	0.15	0.36	0.24	0.23	0.16	0.53	0.56	0.28	0.23	0.38	0.30	0.34	0.38	0.29	0.34
Al_2O_3	3.35	2.12	3.03	2.23	1.33	3.70	2.91	2.75	2.02	3.93	4.08	2.79	2.49	3.74	2.30	2.37	2.92	2.58	3.60
Cr_2O_3	0.04				0.00	0.02		0.02			0.02	0.06		0.02				0.03	
MnO	0.54	0.65	0.61	0.53	0.64	0.58	0.43	0.53	0.58	0.61	0.68	0.55	0.57	0.69	0.61	0.54	0.53	0.60	0.54
FeO	19.88	18.64	20.62	18.94	18.65	20.79	19.61	19.51	19.42	20.92	20.64	19.50	19.17	21.07	19.89	20.31	19.96	19.52	19.98
MgO	11.10	11.89	10.29	11.70	12.14	10.47	11.22	11.45	11.77	10.26	10.15	11.13	11.46	10.42	11.04	11.06	10.68	11.37	10.48
CaO	10.95	11.39	11.35	11.69	11.60	10.82	11.87	11.92	11.73	11.02	11.26	11.60	11.87	10.83	11.58	11.49	11.64	11.75	11.61
Na_2O	0.68	0.25	0.44	0.29	0.20	0.82	0.36	0.34	0.21	0.85	0.65	0.38	0.28	0.73	0.35	0.31	0.37	0.32	0.56
K_2O	0.25	0.16	0.29	0.15	0.09	0.26	0.19	0.19	0.12	0.32	0.35	0.21	0.17	0.27	0.16	0.19	0.21	0.18	0.30
F																			
Total	97.62	97.09	97.40	97.46	97.70	97.11	97.54	98.05	97.67	97.38	97.08	96.91	97.36	96.97	97.46	97.32	96.53	96.78	97.22
Si (T)[a]	7.51	7.73	7.56	7.67	7.82	7.41	7.54	7.56	7.66	7.33	7.33	7.56	7.61	7.35	7.65	7.58	7.52	7.51	7.47
Al (T)	0.49	0.27	0.44	0.33	0.18	0.59	0.46	0.44	0.35	0.67	0.67	0.45	0.39	0.65	0.36	0.42	0.48	0.46	0.53
Ti (T)																		0.03	
Fe3+ (T)																			
Ti (C)	0.04	0.01	0.05	0.03	0.02	0.04	0.03	0.03	0.02	0.06	0.06	0.03	0.03	0.04	0.03	0.04	0.04	0.00	0.04
Al (C)	0.10	0.10	0.09	0.06	0.05	0.06	0.05	0.04	0.01	0.02	0.06	0.05	0.04	0.02	0.05		0.04		0.11
Cr (C)	0.01					0.00		0.00			0.00	0.01		0.00				0.00	
Fe^{3+} (C)	0.27	0.13	0.20	0.18	0.08	0.39	0.32	0.32	0.28	0.55	0.41	0.29	0.27	0.49	0.21	0.30	0.32	0.41	0.27
Fe^{2+} (C)	2.12	2.13	2.36	2.14	2.17	2.16	2.12	2.09	2.10	2.07	2.19	2.14	2.12	2.11	2.25	2.19	2.20	2.04	2.24
Mg (C)	2.46	2.64	2.30	2.59	2.68	2.35	2.49	2.52	2.60	2.29	2.28	2.49	2.54	2.34	2.46	2.47	2.40	2.54	2.34

(*continued on next page*)

Table 8 (*continued*)

Sample	MUN19–5	MUN19–5	MUN19–5	MUN19–5	MUN19–5	MUN19–5	MUN19–5	MUN19–5	MUN19–5	MUN19–5	MUN19–5	MUN19–5	MUN19–5	MUN19–5	MUN19–5	MUN19–5	MUN19–5	MUN19–5	MUN19–5
Run	M19 5 30	M19 5 31	M19 5 34	M19 5 40	M19 5 41	M19 5 42	M19 5 44	M19 5 45	M19 5 46	M19 5 47	M19 5 48	M19 5 49	M19 5 50	M19 5 51	M19 5 52	M19 5 53	M19 5 54	M19 5 55	M19 5 56
Position	int	rim	matrix	rim	core	core	rim	int	int	core	core	int	rim	int	matrix	rim	rim	core	non altered
Mn^{2+} (B)	0.07	0.08	0.08	0.07	0.08	0.07	0.05	0.06	0.07	0.07	0.09	0.07	0.07	0.09	0.08	0.07	0.07	0.07	0.06
Fe^{2+} (B)	0.08	0.07	0.03	0.03	0.05	0.07	0.00		0.03		0.00	0.01		0.06	0.02	0.05			
Ca (B)	1.75	1.82	1.83	1.86	1.84	1.74	1.89	1.89	1.86	1.77	1.82	1.86	1.89	1.75	1.85	1.84	1.88	1.89	1.87
Na (B)	0.11	0.04	0.06	0.04	0.03	0.12	0.05	0.05	0.03	0.16	0.10	0.06	0.04	0.11	0.05	0.05	0.05	0.05	0.07
Ca (A)																			
Na (A)	0.09	0.04	0.06	0.04	0.03	0.12	0.05	0.05	0.03	0.09	0.10	0.06	0.04	0.11	0.05	0.05	0.05	0.05	0.09
K (A)	0.05	0.03	0.06	0.03	0.02	0.05	0.04	0.04	0.02	0.06	0.07	0.04	0.03	0.05	0.03	0.04	0.04	0.04	0.06
OH (W)	2.00	2.00	2.00	2.00	2.00	2.00	2.00	2.00	2.00	2.00	2.00	2.00	2.00	2.00	2.00	2.00	2.00	2.00	2.00
F (W)																			
Sum T,C,B,A	15.14	15.07	15.12	15.07	15.04	15.17	15.09	15.09	15.05	15.15	15.16	15.10	15.07	15.16	15.08	15.08	15.10	15.08	15.15
T (°C)[b]	673	653	661	651	644	683	659	660	662	687	687	662	653	726	650	673	662	681	670
P (kbar)[b]																			
$(H_2O)^{b}_{melt}$ (wt%)	5.15	4.96	5.42	5.1		5.42	5.51	5.37	5.29	5.45	5.60	5.33	5.32	5.55	5.28	5.29	5.52	5.29	5.75

Sample	MUN19–5	MUN19–5	MUN19–5	MUN19–5	MUN19–5	MUN19–5	MUN19–5	MUN19–5	MUN19–5	MUN19–5	MUN19–5	MUN19–5
Run	M19 5 57	M19 5 58	M19 5 61	M19 5 63	M19 5 64	M19 5 65	M19 5 67	M19 5 73	M19 5 74	M19 5 87	M19 5 21	M19 5 28
Position	core	rim	int	rim	core	core	rim	core (matrix)	core (matrix)	matrix		
SiO_2	50.93	50.08	51.05	49.09	50.56	50.71	50.63	50.38	47.74	51.48	52.73	52.51
TiO_2	0.20	0.29	0.13	0.45	0.34	0.35	0.35	0.43	0.70	0.12	0.10	0.10
Al_2O_3	2.42	3.32	2.38	3.71	2.45	2.34	2.52	2.96	4.93	2.12	0.59	0.44
Cr_2O_3		0.09	0.03	0.01	0.02			0.01				
MnO	0.68	0.59	0.62	0.69	0.54	0.58	0.58	0.63	0.59	0.71	1.74	1.82
FeO	19.69	20.19	19.51	20.73	19.56	19.92	19.79	20.03	21.69	18.70	28.10	28.85
MgO	11.29	10.40	11.39	10.31	11.28	11.16	11.12	11.15	9.14	11.69	12.27	12.3
CaO	11.63	11.42	11.55	10.85	11.81	11.88	11.45	11.34	10.77	11.47	2.21	1.43
Na_2O	0.30	0.43	0.28	0.71	0.34	0.31	0.31	0.35	0.56	0.32	0.08	0.07
K_2O	0.19	0.22	0.16	0.30	0.18	0.18	0.19	0.47	1.04	0.13	0.02	0.02
F												
Total	97.32	97.02	97.11	96.83	97.07	97.43	96.93	97.74	97.14	96.75	97.83	97.53
Si (T)[a]	7.60	7.53	7.62	7.41	7.56	7.57	7.59	7.51	7.27	7.70	8.33	8.34
Al (T)	0.40	0.47	0.38	0.59	0.43	0.41	0.41	0.49	0.73	0.30		
Ti (T)					0.01	0.02						
Fe3+ (T)												
Ti (C)	0.02	0.03	0.02	0.05	0.03	0.02	0.04	0.05	0.08	0.01	0.01	0.01
Al (C)	0.02	0.11	0.04	0.07			0.04	0.03	0.16	0.07	0.11	0.08
Cr (C)		0.01	0.00	0.00	0.00			0.00				
Fe^{3+} (C)	0.30	0.24	0.27	0.36	0.34	0.35	0.26	0.27	0.22	0.18		
Fe^{2+} (C)	2.15	2.27	2.13	2.20	2.11	2.14	2.18	2.17	2.46	2.13	3.71	3.83
Mg (C)	2.51	2.33	2.54	2.32	2.51	2.48	2.49	2.48	2.08	2.61	0.41	0.43
Mn^{2+} (B)	0.09	0.08	0.08	0.09	0.06	0.06	0.07	0.08	0.08	0.09	0.89	1.01
Fe^{2+} (B)	0.01	0.03	0.03	0.06			0.04	0.06	0.08	0.03		
Ca (B)	1.86	1.84	1.85	1.75	1.89	1.90	1.84	1.81	1.76	1.84	0.38	0.24
Na (B)	0.04	0.06	0.04	0.10	0.05	0.05	0.05	0.05	0.09	0.05	0.03	0.02
Ca (A)												
Na (A)	0.04	0.06	0.04	0.10	0.05	0.05	0.05	0.05	0.07	0.05		
K (A)	0.04	0.04	0.03	0.06	0.03	0.04	0.04	0.09	0.20	0.02	0.00	0.00
OH (W)	2.00	2.00	2.00	2.00	2.00	2.00	2.00	2.00	2.00	2.00	2.00	2.00

(*continued on next page*)

Table 8 (*continued*)

Sample	MUN19–5	MUN19–5	MUN19–5	MUN19–5	MUN19–5	MUN19–5	MUN19–5	MUN19–5	MUN19–5	MUN19–5	MUN19–5	MUN19–5
Run	M19 5 57	M19 5 58	M19 5 61	M19 5 63	M19 5 64	M19 5 65	M19 5 67	M19 5 73	M19 5 74	M19 5 87	M19 5 21	M19 5 28
Position	core	rim	int	rim	core	core	rim	core (matrix)	core (matrix)	matrix		
F (W)												
Sum T,C,B,A	15.08	15.11	15.07	15.16	15.08	15.08	15.08	15.14	15.27	15.07	14.62	14.62
T (°C)[b]	672	666	671	687	672	667	671	696	716	649		
P (kbar)[b]												
$(H_2O)^b_{melt}$ (wt%)	5.40	5.84	5.50	5.42	5.26	5.24	5.30	4.87	4.50	5.09		

[a]Structural amphibole formula was calculated according to Locock (2014).
[b]Pressure, temperature and melt water content obtained by Amp thermobarometry from Ridolfi et al. (2010).

Table 9
Microprobe analyses of pyroxenes from the subvolcanic dikes from Cerro Munro.

Sample	MUN19–2	MUN19–2	MUN19–2	MUN19–2	MUN19–2	MUN19–2	MUN19–2	MUN19–2	MUN19–2	MUN19–2
Run	M19 2 1	M19 2 2	M19 2 2a	M19 2 3	M19 2 4	M19 2 5	M19 2 5b	M19 2 7	M19 2 7b	M19 2 23
phase	Opx	Opx	Opx	Opx	Opx	Opx	Opx	Cpx	Opx	Opx
Position	rim	int	int	core	int	rim		matrix	matrix	
SiO_2	53.22	53.37	53.89	52.69	53.05	52.67	53.81	53.03	52.29	53.28
TiO_2	0.36	0.20	0.01	0.24	0.30	0.30	0.08	0.20	0.12	0.28
Al_2O_3	0.66	0.45	0.18	0.80	1.16	0.88	0.26	0.95	0.30	0.62
FeO	21.54	21.60	21.35	21.70	21.37	22.08	22.58	8.70	22.53	22.43
MgO	22.96	23.39	24.71	23.12	23.43	23.19	22.97	14.52	23.07	23.21
MnO	0.60	0.52	0.59	0.56	0.50	0.51	0.77	0.33	0.72	0.64
CaO	1.49	1.30	0.60	1.43	1.43	1.30	0.96	22.28	0.84	1.29
Na_2O	0.04	0.03	0.03		0.05	0.04		0.44		0.00
K_2O				0.03			0.03	0.01	0.02	0.01
F										
SrO			0.01						0.01	
Cr_2O_3	0.00		0.02	0.00	0.02	0.03		0.04		0.03
Total	100.9	100.9	101.4	100.6	101.3	101.0	101.5	100.5	99.9	101.8
#Mg	0.66	0.66	0.67	0.66	0.66	0.65	0.64	0.75	0.65	0.65

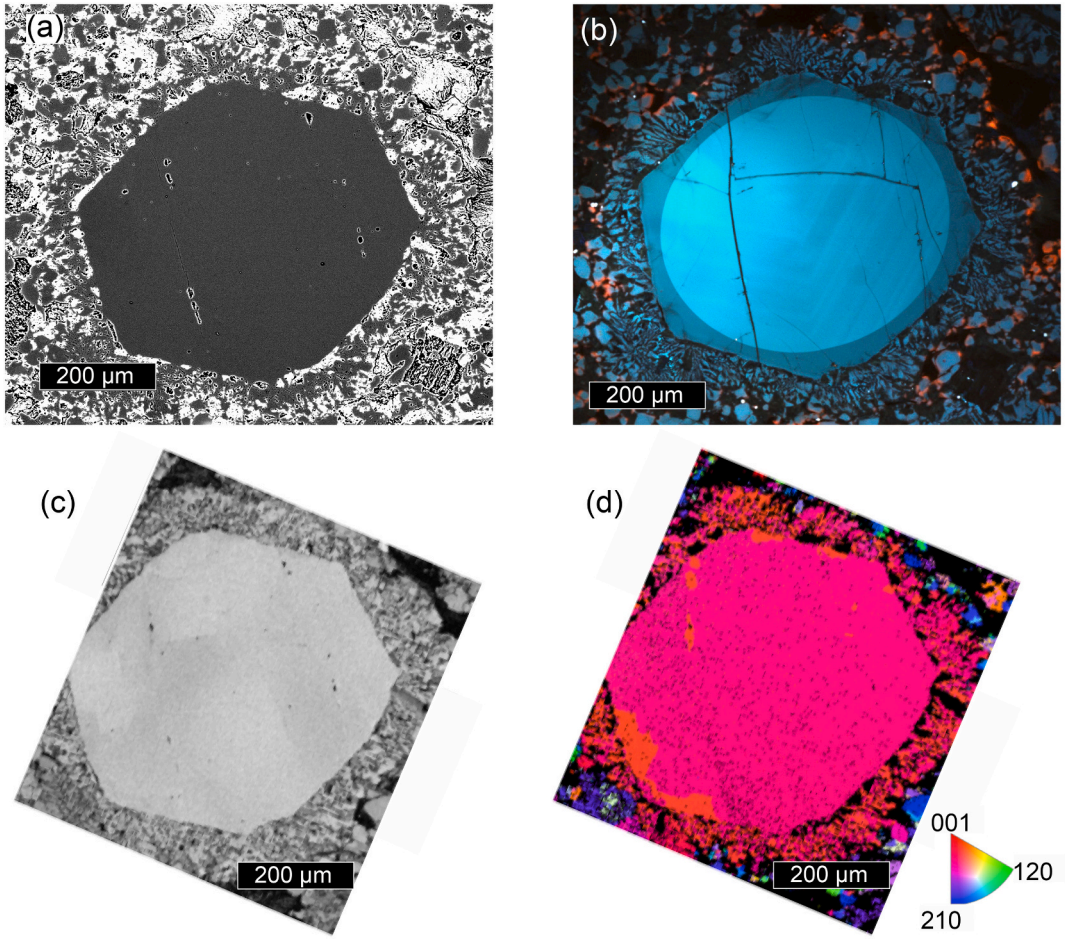

Fig. 7. (a) BSE image of Qz from rhyolitic porphyry A312–24. (b) Real colour cathodoluminiscenceimage of Qz from sample A312–24. (c) Image quality. (d) Orientation map using Miller indices as orientation parameter. Red colour indicates the occurrence of the *c* crystallographic axis of Qz parallel to the normal direction in the sample (z). A certain grade of misorientation can be appreciated in the idiomorphic crystal of the image. In addition, Qz occurring at the mirmekyte rims mantains the orientation of large central crystal. (For interpretation of the references to colour in this figure legend, the reader is referred to the web version of this article.)

section.

8.2. *Compositional magma splitting in the tonalite pluton*

The observed textural and geochemical relations between enclaves and host tonalites support a process of compositional magma splitting occurred at the margins of the feeder channels, below the present-day erosional level. A thermal boundary layer (TBL) is created, giving rise to a solidification front where temperature may vary from near *solidus* at the cold margin to the *liquidus* towards the interior of the conduit. Multiple lines of evidence from dynamic experiments in a TBL (Rodríguez and Castro, 2017) and geological record (Bacon, 1986; Rodríguez and Castro, 2018; Weinberg et al., 2021; Xu et al., 2021) yield that fractionation by gas-driven filter pressing is an efficient mechanism of crystal–liquid separation in water-bearing magmas. Thus, liquid is expelled when water reaches saturation and second boiling promotes melt segregation (Pistone et al., 2020; Sisson and Bacon, 1999).

The andesite composition is preferred as parental magma because it has a major- and trace-element composition just in the gap separating MME and host tonalites (Fig. 11). Although massive plutonic rocks of Munro represent the evolved liquid of the compositional splitting process, most sampled tonalites are in turn plagioclase-rich cumulates from which, a late residual liquid was extracted. This is revealed by the cumulate textures observed in most tonalites. Also, the sampled tonalites represent the last stage of a time-elapsed process, while enclaves represent arrested (chilled) magmatic system, like a snapshot of a time-evolving process.

Mechanical considerations indicate that the crystal-liquid separation is most efficient if water saturation is reached at a high critical crystallinity X_{cc} around 0.7 (Castro et al., 2021; Pistone et al., 2015; Pistone et al., 2020), which can be reached for magmas containing 3 wt% of initial dissolved water and at pressures of 3 kbar and higher (Fig. 14a). In the case of Cerro Munro magma chamber, crystallization proceeded at around 1 kbar pressure. Thus, to water saturation be reached within the high crystallinity region of the solidification front and liquid segregation be effective, the initial water content of the magma must be between 1.1 and 1.5 wt% (Fig. 14a). This is in accordance with the late crystallization of amphibole in tonalites and enclaves. That is, the melt water content for Amp stabilization at low pressure (ca. 4 wt% H_2O; Naney, 1983), is reached when a high crystal fraction (ca. 60% crystals) is present in the magma. At the referred pressure of 1 kbar, that melt is water saturated close to the 4% water.

8.2.1. *Composition of the expelled melt*

The composition of the expelled hydrous melt can be approached by Rhyolite-MELTS thermodynamic modelling (Gualda et al., 2012) using the assumed andesite composition as the parental magma of enclaves and fractionated tonalite. The expelled melt fraction is controlled by the fraction of saturated liquid assuming an initial water content of 1.5 wt% in the andesite parental magma and a pressure of crystallization of 1

Table 10
Whole-rock analyses of major and trace elements of Cerro Munro Tonalite and related rocks.

Sample	A312–29	A312–29b	A312–32	A312–33	A312–33a	A312–36	A312–36a	A312–36b	A312–36c	A312–37	A312–37a	A312–38	C.2011–11
Rock Type	Tonalite	Autolith	Tonalite	Tonalite	Autolith	Tonalite	Autolith	Autolith	Autolith	Tonalite	Autolith	Autolith	Tonalite
Major elements (wt%)													
SiO_2	63.19	57.21	61.95	63.07	57.81	64.21	64.32	61.1	57.86	65.37	57.73	58.31	63.19
TiO_2	0.8	1.13	0.88	0.79	1.05	0.37	0.43	0.88	0.8	0.69	1.03	0.92	0.8
Al_2O_3	16.36	16.5	16.51	16.66	16.78	18.92	18.54	16.78	16.81	15.9	16.39	16.73	16.36
FeOt	4.45	6.68	4.84	4.28	6.35	2.22	2.29	4.98	6.37	3.77	6.27	6.23	4.49
MgO	2.44	3.44	2.63	2.13	3.77	1.15	1.14	2.93	4.07	1.92	3.6	3.7	2.44
MnO	0.09	0.14	0.09	0.09	0.17	0.04	0.05	0.09	0.13	0.07	0.15	0.11	0.09
CaO	4.05	6.24	4.46	3.99	5.5	4.1	3.98	5.17	6.12	3.14	5.62	6.64	4.05
Na_2O	4.05	4.1	4	4.19	4.24	4.57	4.58	3.93	4.09	4.17	4.44	4.39	4.05
K_2O	2.01	1.61	1.96	2.2	1.82	2.58	2.56	1.73	1.1	2.56	1.57	1.04	2.01
P_2O_5	0.28	0.39	0.31	0.26	0.3	0.14	0.14	0.3	0.24	0.22	0.34	0.33	0.28
Loi	1.19	1.16	1.47	1.36	0.98	0.77	0.98	0.92	1.19	1.13	1.42	0.34	1.19
Total	98.91	98.6	99.1	99.02	98.77	99.07	99	98.81	98.77	98.94	98.56	98.74	98.95
ASI[a]	1.05	0.87	1.03	1.05	0.92	1.08	1.08	0.99	0.91	1.07	0.89	0.85	1.05
$K/K + Ca$[b]	0.23	0.13	0.21	0.25	0.16	0.27	0.28	0.17	0.1	0.33	0.14	0.09	0.23
Mg#[c]	0.49	0.48	0.49	0.47	0.51	0.48	0.47	0.51	0.53	0.48	0.51	0.51	0.49
Fe#[d]	0.65	0.66	0.65	0.67	0.63	0.66	0.67	0.63	0.61	0.66	0.64	0.63	0.65
Trace elements (ppm													
Li	36.4	32.78	29.93	28.44	36.37	24.8	17.72	27.8	28.23	29.34	40.45	9.08	36
Sc	12.09	20.62	11.93	10.13	21.48	6.54	5.31	12.47	20.56	9.68	20.45	20.33	12.1
V	92.62	150.53	93.99	78.76	129.16	66.6	47.74	93.84	137.73	72.19	124.08	147.78	92.6
Cr	51.77	33.38	46.29	25.21	77.57	34.42	17.98	41.99	87.05	26.67	62.1	64.3	51.8
Co	30.58	26.81	25.46	25.81	29.66	42.46	21.08	27.48	32.19	25.61	27.88	32.63	30.6
Ni	34.69	31.77	34.13	20.74	43.68	31.93	19.55	38.84	67.27	26.55	32.44	40	34.7
Cu	37.44	197.13	29.02	22.56	44.75	26.94	18.27	33.34	41.05	18.99	28.65	73.09	37.4
Zn	73.75	89.21	75.39	73.97	129.04	46.85	34.13	69.1	92.06	64.92	110.63	90.03	73.7
Ga	18.54	17.89	18.1	18.35	18.99	25.78	18.45	17.81	18.07	18.22	18.4	17.64	18.5
Rb	58.71	49.07	50.14	58.72	57.79	79.96	58.62	44.81	25.32	60.6	51.81	17.62	58.7
Sr	384.5	389.3	402	345.4	352.9	611.7	462.1	420.5	425.7	281.9	369.9	430.8	384
Y	21.25	26.48	20.74	21.76	40.08	11.17	9.34	18.9	22.15	24.96	30.09	21.93	21.2
Zr	208.8	118.8	208.6	255.7	195.5	241.1	239.2	185.7	60.8	224.6	227.8	118.6	20
Nb	13.77	17.31	14.29	14.97	21.85	9.52	7.75	12.66	10.32	15.5	15.52	10.63	13.8
Cs	1.92	1.82	1.71	1.96	2.97	2.03	1.33	1.66	0.86	1.21	2.39	0.9	1.9
Ba	316.2	202.1	316.4	324.7	266.7	379.3	323.8	258	196.1	354	192.8	258.2	316
La	27.6	33.45	26.53	29.85	33.42	21.05	16.4	23.42	21.1	30.1	31.05	22.74	27.6
Ce	59.55	73.22	57.26	61.33	81.08	37.45	31.07	50.18	46.79	67.1	68.37	50.05	59.6
Pr	7.11	8.7	6.8	7.09	10.51	4.17	3.44	6.06	5.9	8.12	8.35	6.19	7.1
Nd	26.67	32.88	25.53	26.64	41.01	15.16	12.36	22.97	23.03	31.11	32.05	24.44	26.7
Sm	5.18	6.43	5.02	5.05	8.54	2.74	2.28	4.52	4.84	6.15	6.67	5.11	5.2
Eu	1.35	1.55	1.3	1.39	1.74	1.57	1.17	1.24	1.44	1.27	1.62	1.5	1.4
Gd	4.79	5.89	4.41	4.63	7.89	2.32	1.96	4.06	4.59	5.49	6.13	4.72	4.8
Tb	0.7	0.87	0.66	0.63	1.25	0.34	0.28	0.6	0.68	0.76	0.94	0.69	0.7
Dy	3.96	4.91	3.71	3.65	7.16	1.79	1.68	3.38	4.08	4.49	5.36	4	4
Ho	0.8	1.02	0.75	0.76	1.55	0.38	0.31	0.67	0.86	0.91	1.12	0.82	0.8
Er	2.04	2.57	1.98	1.95	4.03	1.01	0.81	1.75	2.18	2.33	2.91	2.11	2
Tm	0.31	0.4	0.31	0.3	0.66	0.18	0.13	0.27	0.34	0.35	0.45	0.32	0.3
Yb	1.93	2.52	1.85	1.91	4.2	1.02	0.82	1.67	2.1	2.05	2.82	1.99	1.9
Lu	0.27	0.36	0.27	0.28	0.6	0.15	0.12	0.23	0.29	0.3	0.4	0.28	0.3
Hf	0.35	0.74	0.98	0	0.8	−0.37	0.15	0.34	0.77	0	0.59	0.67	0.4
Ta	1.67	1.56	1.36	1.42	2.15	3.27	1.51	1.41	1.28	1.62	1.53	1.3	1.7
Pb	7.81	10.66	6.15	8.03	20.38	8.54	7.48	7.18	9.44	9.75	12.18	7.53	7.8
Th	6.68	6.52	6.91	9.44	7.57	9.8	7.61	6.23	4.81	8.73	6.59	3.57	7.6

(*continued on next page*)

Table 10 (*continued*)

Sample	A312–29	A312–29b	A312–32	A312–33	A312–33a	A312–36	A312–36a	A312–36b	A312–36c	A312–37	A312–37a	A312–38	C.2011–11
Rock Type	Tonalite	Autolith	Tonalite	Tonalite	Autolith	Tonalite	Autolith	Autolith	Autolith	Tonalite	Autolith	Autolith	Tonalite
U	0.57	0.61	0.76	0.75	1.36	0.97	0.68	0.69	0.71	0.75	0.83	0.87	0.6

Sample	A312–30	A312–31	A312–34	A312–35	Mun19–2	Mun19–3	Mun19–5
Rock type	Slates (host rock)	Slates (host rock)	Rhyolitc porphyry	Andesite porphyry dyke	Andesite porphyry dyke	Dacite porphyry dyke	Dacite
Major elements (wt%)							
SiO_2	60.13	66.44	76.58	61.59	61.67	65.65	64.95
TiO_2	1.01	0.81	0.04	0.87	1.04	0.71	0.66
Al_2O_3	17.63	15.55	13.57	16.14	16.30	16.05	15.51
FeOt	7.43	5.92	0.5	4.60	5.11	3.45	5.09
MgO	3.35	2.46	0.26	2.44	2.98	1.35	1.67
MnO	0.19	0.07	0.02	0.08	0.08	0.06	0.08
CaO	3.66	1.05	0.2	3.84	5.27	3.72	3.34
Na_2O	1.95	2.35	1.19	4.13	4.31	4.55	4.80
K_2O	3.05	2.63	5.61	1.92	1.74	2.85	2.22
P_2O_5	0.35	0.11	0.06	0.38	0.36	0.24	0.19
Loi	0	1.21	1.65	2.98	0.16	0.22	0.59
Total	98.75	98.6	99.68	98.97	99.02	98.85	99.10
ASI[a]	1.43	1.86	1.64	1.08	0.92	0.96	0.97
K/K + Ca[b]	0.33	0.6	0.94	0.23	0.16	0.31	0.28
Mg#[c]	0.45	0.43	0.48	0.49	0.51	0.41	0.37
Fe#[d]	0.69	0.71	0.66	0.65	0.63	0.72	0.75
Trace elements (ppm)							
Li	103.75	68.84	75.96	54.44	21.00	13.06	24.41
Sc	21.32	14.56	2.83	11.37	12.09	7.44	14.71
V	151.52	101.54	3.37	98.74	103.0	59.51	44.19
Cr	105.11	75.76	1.86	62.86	67.60	30.44	36.52
Co	34.92	30.11	15.29	23.51	42.61	31.39	54.76
Ni	53.17	40.33	4.61	27.24	36.57	13.35	14.59
Cu	31.34	17.81	1.98	34.62	30.71	51.89	16.17
Zn	112.41	89.76	19	88.34	80.48	62.32	66.58
Ga	23.13	18.86	17.61	18.61	18.38	18.27	18.81
Rb	128.95	106.5	158.56	42.67	42.26	72.85	59.67
Sr	168.8	205.1	21	484.7	340.5	331.4	188.9
Y	38.44	14.56	11.55	17.49	18.47	19.11	25.57
Zr	199.5	220.8	38.8	143.54	242.90	270.40	454.50
Nb	14.78	13.86	24.44	11.21	12.05	14.99	12.60
Cs	11.17	6.64	3.16	3.05	1.18	2.79	2.39
Ba	536.1	394.2	196.9	401.70	237.68	343.16	358.47
La	41.38	29.44	4.21	25.68	22.22	27.20	25.57
Ce	86.23	61.9	10	55.47	48.37	58.63	55.34
Pr	10.43	7.19	1.27	6.71	5.84	6.84	6.67
Nd	41.8	27.81	4.28	25.56	22.93	25.84	26.38
Sm	9.14	5.47	1.53	4.97	4.55	4.82	5.57
Eu	2.01	1.26	0.22	1.37	1.22	1.11	1.62
Gd	8.5	4.54	1.59	4.41	3.71	3.83	4.76
Tb	1.2	0.57	0.3	0.63	0.58	0.59	0.78
Dy	6.74	3.06	2.01	3.39	3.21	3.31	4.62
Ho	1.38	0.56	0.37	0.66	0.64	0.65	0.94
Er	3.56	1.32	0.99	1.58	1.64	1.75	2.41
Tm	0.57	0.21	0.16	0.24	0.25	0.29	0.37
Yb	3.54	1.31	1.05	1.49	1.51	1.68	2.18

(*continued on next page*)

Table 10 (*continued*)

Sample	A312–30	A312–31	A312–34	A312–35	Mun19–2	Mun19–3	Mun19–5
Rock type	Slates (host rock)	Slates (host rock)	Rhyolitc porphyry	Andesite porphyry dyke	Andesite porphyry dyke	Dacite porphyry dyke	Dacite
Lu	0.52	0.2	0.15	0.21	0.23	0.26	0.33
Hf	0	0	0.95	3.07	1.94	4.54	3.88
Ta	1.78	1.86	3.2	1.21	0.88	1.24	0.93
Pb	27.84	17.64	7.58	8.76	5.03	9.15	7.22
Th	11.2	8.89	2.92	5.55	6.05	12.52	5.88
U	2.94	1.59	1.95	1.38	1.22	3.13	1.24

LOI: Loss of ignition.
[a]ASI = [Al_2O_3/(Na_2O + K_2O+(CaO-1,67*P_2O_5))]
[b]K/(K + Ca) = molar K_2O/[K_2O + CaO]
[c]Mg# = molar MgO/[MgO+ FeO]
[d]Fe* = wt% FeOt/[FeOt+MgO]

kbar (see above). A portion of this saturated melt is retained within the crystal framework and the other one will be expelled out when the saturation is reached. The saturated melt fraction (X_{melt}) is given by the water-based mass balance:

$$X_{melt} = W_0/W_s \quad (1)$$

Being W_0 the initial water content of the liquid and W_s the water content at saturation according to Burnham's model (Burnham, 1979). The low pressure (1 kbar) is constrained by amphibole barometry and the initial water content (1.5 wt%) is assumed by the late crystallization of amphibole in residual melt pools in the tonalites and enclaves, and by the prerequisite to reach the critical crystallinity with initial water contents between 1.1 and 1.5 wt% (Fig. 14e). Value of $W_s = 4$ wt% H_2O is obtained for 1 kbar and, consequently, a saturated melt fraction ranging from 0.28 to 0.38 wt%. The composition of this saturated melt is given in Table 11. This is a leucogranodiorite or K-rich trondhjemite. It may represent the melt expelled from the chilled margin of ascent conduits, which is mixed with new pulses of pristine andesite that contribute to generate the fractionated tonalite magma. The latter is a mixture of the pristine andesite and the expelled leucogranodiorite hydrous melt. A multielemental mass balance is applied to estimate the expelled melt fraction. In this case, the matrix terms of the equation are the andesite (**AN**) as the whole system and the enclave (**ENC**) and the expelled water-saturated melt (**EM**) as the contributing parts of the system:

$$\mathbf{AN} = \mathbf{EM}^*X + \mathbf{ENC}^*(1 - X) \quad (2)$$

Being X the fraction of expelled melt (EM), given by X = (**AN** – **ENC**) / (**EM** – **ENC**). *Difference plots* are shown in Fig. 14, yielding a mass fraction close to 0.2. These values represent the expelled melt from the rigid crust (Marsh, 2002) without considering the retained melt fraction into the crystal framework. For this reason, the fraction values are slightly lower compared with those obtained from the water-based mass balance (0.28–0.38). It should be noted that the melt fractions can vary due to uncertainties in the initial water content of the parental andesite and the pressure of crystallization. Nevertheless, the obtained values of crystallinity are within the region of the rigid crust ($X_c > 0.55$) and close to the terminal 20–30% porosity (Donev et al., 2004), where mechanical behavior favor melt separation by gas-driven filter pressing.

A mix between pristine andesite and its own fractionated melt accounts for the straight line (mixing line) defined by tonalites and MME in the CaO–MgO diagram, with the andesitic dike in the middle (Fig. 11f), with a Pearson correlation of $R^2 = 0.96$. This straight line slightly departs from the cotectic curve in this diagram, which is defined by equilibrium crystallization. This result fits the predictions of the in-situ *crystallization* model (Langmuir, 1989) in which, the intruding magma is fluxed by residual liquids expelled from partially crystallized zones of a magma reservoir or dike.

In sum, compositional magma splitting is able to produce MME and tonalites with the textural and geochemical relationships observed in the Cerro Munro pluton. We propose a crystallization history for the Cerro Munro pluton consisting of in situ crystallization (Langmuir, 1989) induced by water saturation of a cooling andesitic parental magma at the ascent conduits. The temperature interval between *solidus* and *liquidus* establishes a solidification front (Marsh, 2002), in which the water saturation will be reached as the crystallization proceeds. If differentiation advances at the ascent conduits, the magma input will drag the MME from the chilled margins at the same time that the intruding magma is being fluxed by the expelled water-saturated liquid to the magma chamber (Fig. 15). Cumulate features in enclaves and tonalites, such as textural and geochemical signatures, can be explained by the advance of a solidification front, from which a residual liquid is expelled, likely generating a reactive flow and promoting the magmatic differentiation (Rodríguez and Castro, 2018; Xu et al., 2021). During the late stages of the magma chamber consolidation, this can potentially trigger a further volcanic event recorded by late rhyolite porphyries, favored by the extensional tectonic setting.

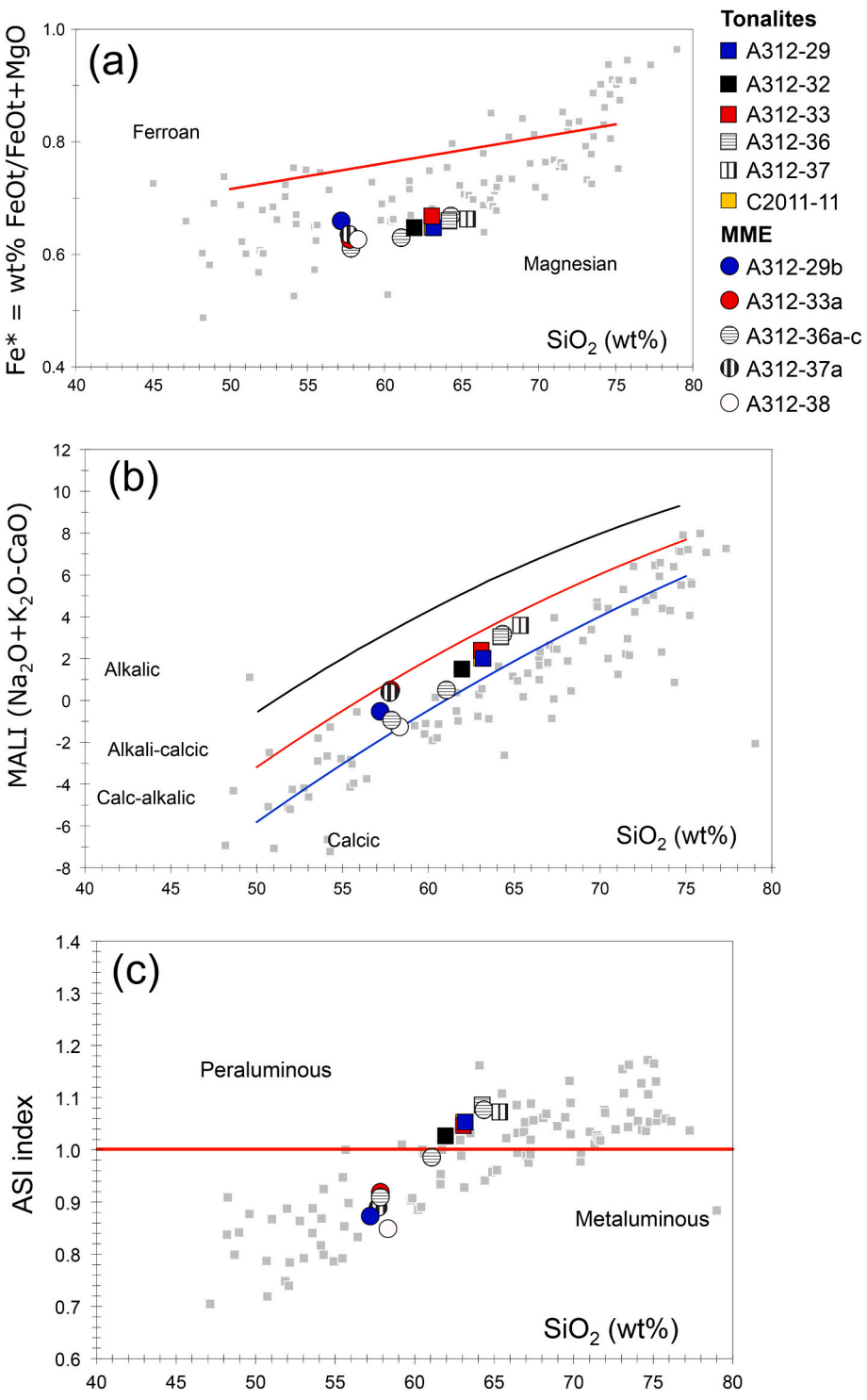

Fig. 8. Classification diagrams for Cerro Munro tonalites and MME. (a) Fe* vs SiO_2 diagram shows the magnesian character of both tonalites and enclaves, according the classification of Frost et al., 2001. (b) MALI index (Frost et al., 2001) indicates that Cerro Munro Tonalite have a calc-alkalic composition. (c) The ASI index separates the MME as metaluminous and the tonalites as peraluminous. Grey dots represent data from Patagonian Batholith (Argentina (Castro et al., 2011), taken as representative of calc-alkaline magmas.

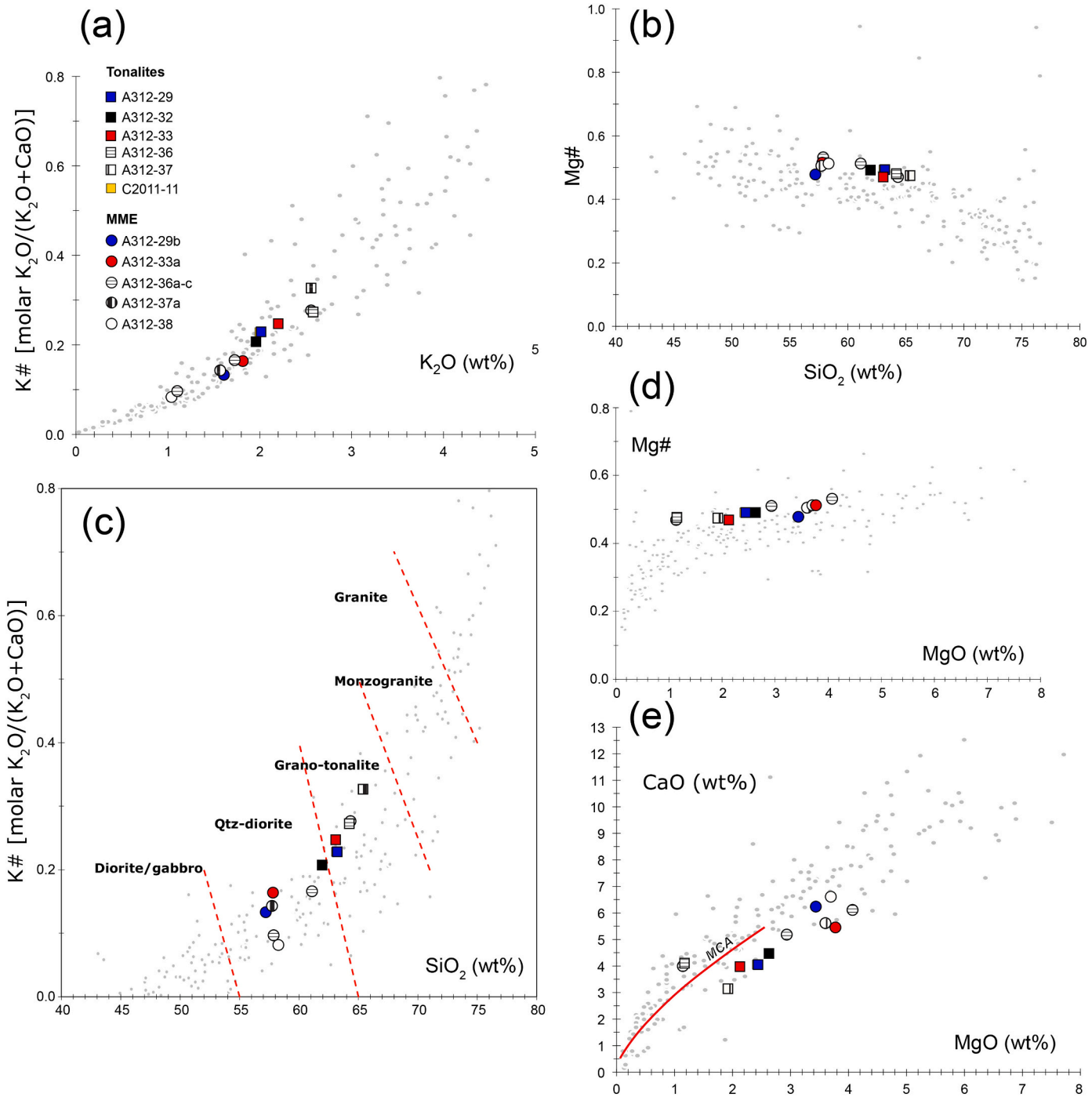

Fig. 9. Variation diagrams for Cerro Munro tonalites and MME. (a) Molar ratio $K_2O/K_2O + CaO$ vs K_2O diagram indicated the calc-alkaline trend by which tonalites and MME are differentiated. (b) Mg number (calculated as molar ratio MgO (MgO + FeO)) maintains high values as the silica content (wt%) increases, away from the trend marked by the Patagonian batholith. (c) K number (molar ratio $K_2O/K_2O + CaO$) vs K_2O plot classifies the MME as Qz-diorite and host-rocks as granodiorites/tonalites. The K number is a proxy of the Streckeisen QAP diagram. The relation of Mg# (d) and CaO (e) with Mg denotes the decoupling of the Cerro Munro samples from the calc-alkaline trend.

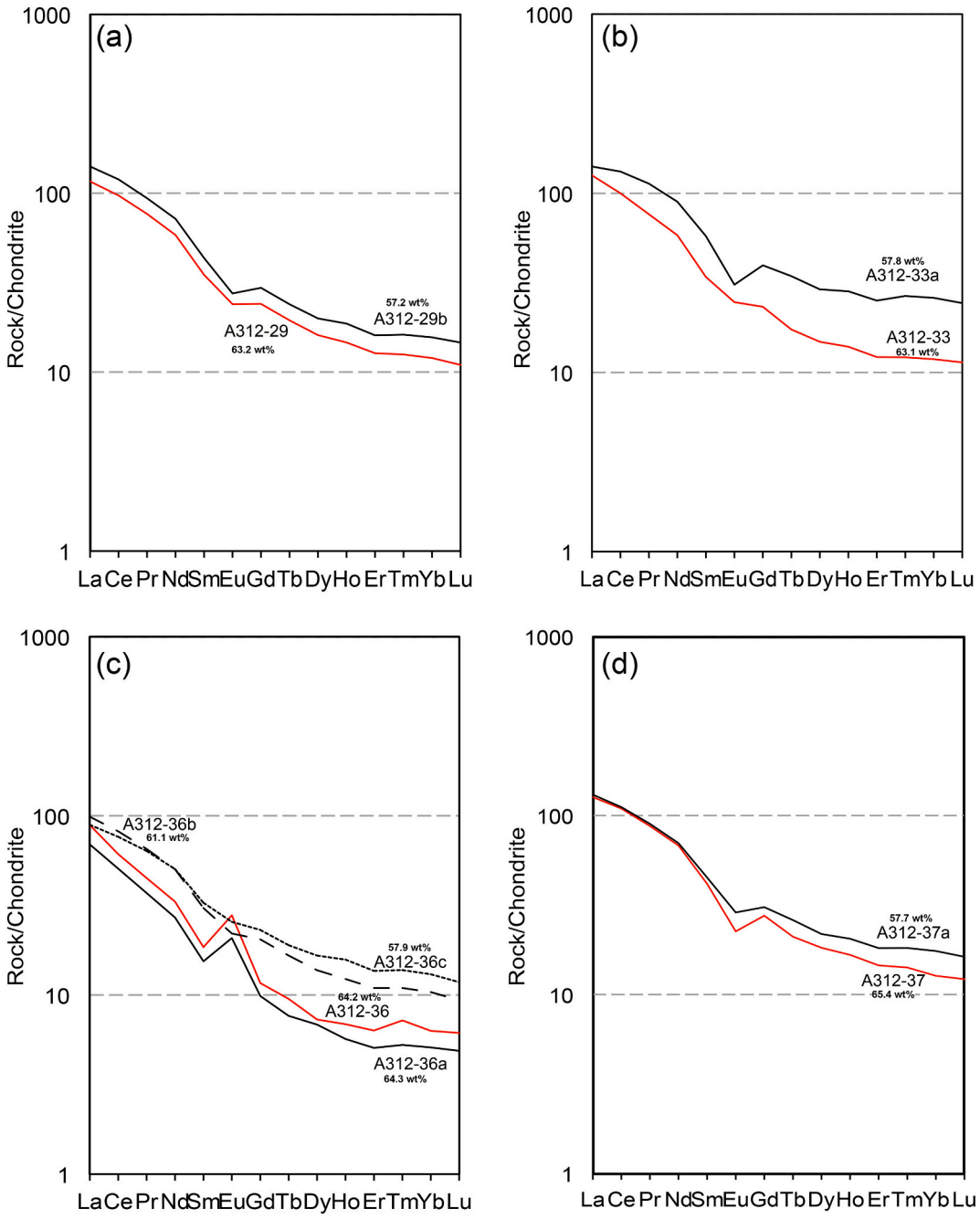

Fig. 10. REE chondrite normalized (Nakamura, 1974) diagrams showing the relation of the tonalites (red curves) with their respective enclaves (black curves). Silica content is indicated in bold font for each sample. (For interpretation of the references to colour in this figure legend, the reader is referred to the web version of this article.)

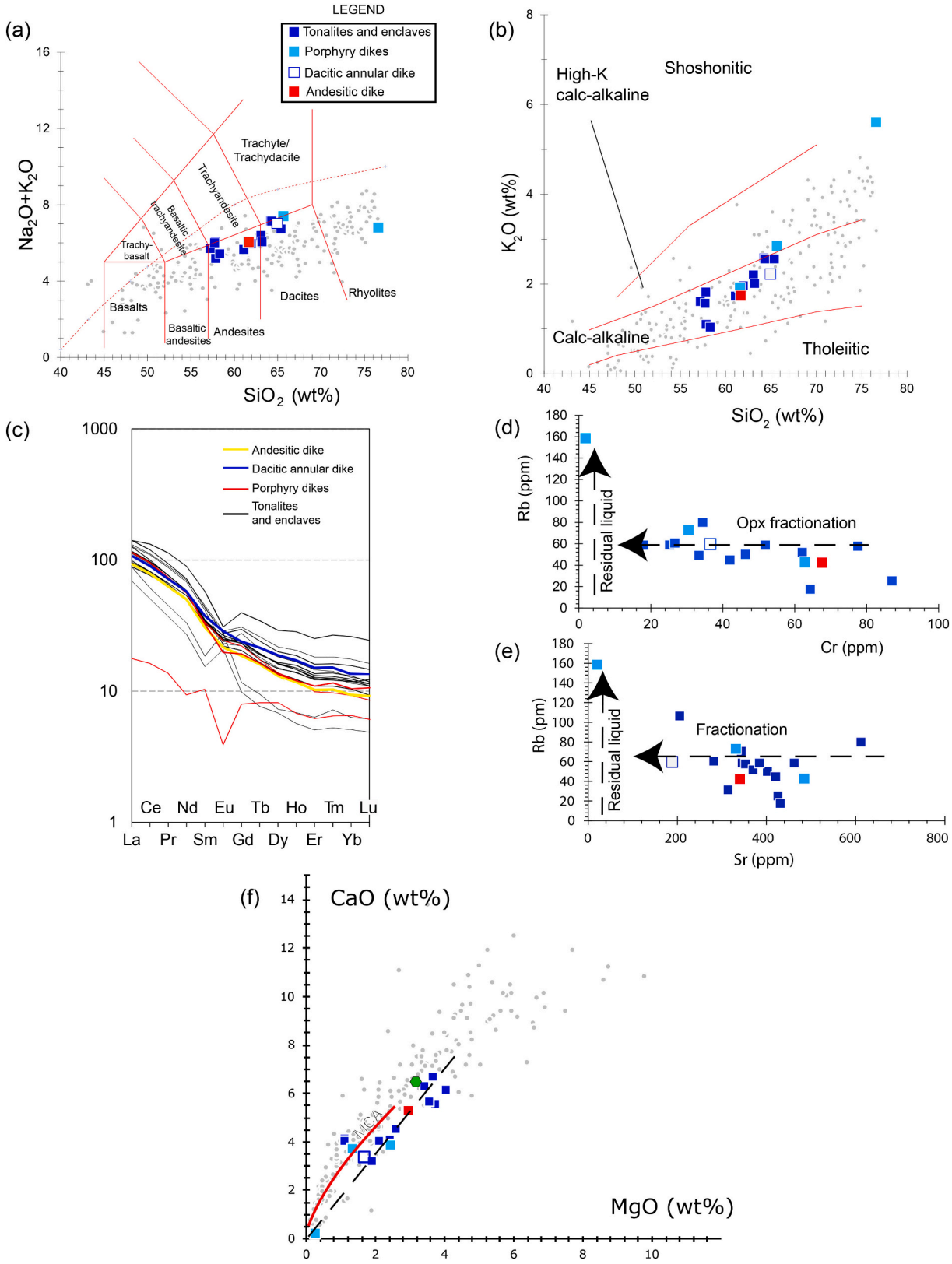

Fig. 11. (a) Total Alkali-Silica diagram for tonalites, MME and dikes from Cerro Munro. (b) SiO_2 vs K_2O diagram showing the calc-alkaline and high-K calc-alkaline affinity for the entire set of tonalites, MME and dikes. (c) REE chondrite normalized (Nakamura, 1974) diagram for tonalites and MME (black curves), andesitic (yellow curve), dacitic annular (blue curve) and porphyry dikes (red curve). (d) Cr vs Rb diagram showing an involvement of Opx, as Cr-rich phase, in the fractionation pattern. (e) Sr vs Rb diagram for igneous rocks from Cerro Munro following a close fractionation pattern. (f) MgO vs CaO diagram for both subvolcanic and plutonic samples. Main cotectic array (MCA; from Castro, 2021) is represented by the red line and their starting material is marked by a green hexagon. (For interpretation of the references to colour in this figure legend, the reader is referred to the web version of this article.)

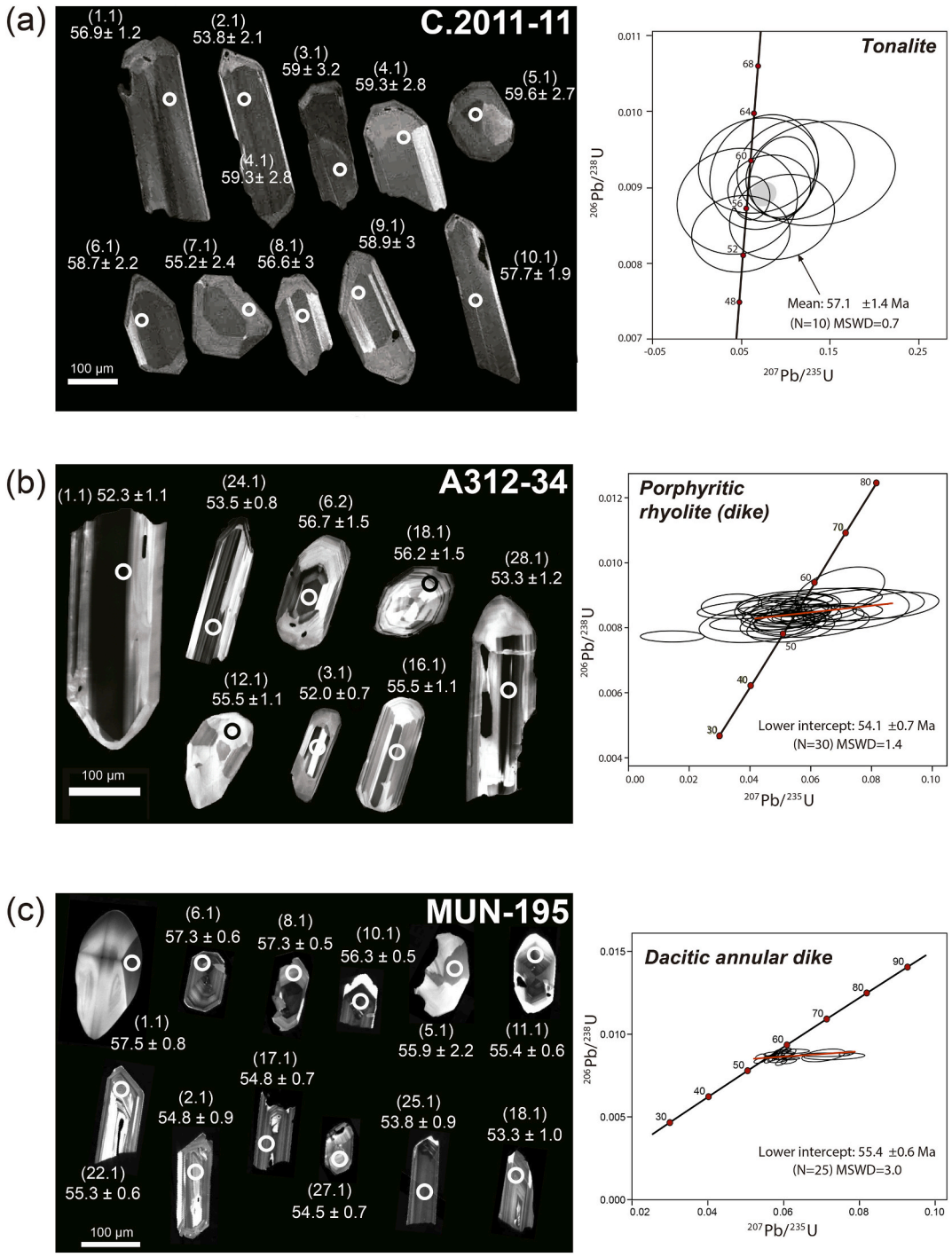

Fig. 12. (a) Cathodoluminescence images of the zircon population analyzed in the tonalite sample (C.2011–11). Spots location and their resulting $^{206}Pb/^{238}U$ ages (*Ma*) are indicated. The concordia U—Pb diagram and the mean age for the obtained ages are shown beside CL images. Error ellipses for data points in the concordia diagrams are 68.3% confidence limits, including the error from the standard. (b) CL images of zircon crystals representing the zircon population ($N = 30$) analyzed in the porphyritic rhyolite sample. The 208-corrected wetherill discordia diagram and the resulting age of the lower intercept are shown together with the cathodoluminescence images. Data are given in Table 8a and b. Scale bars are 100 µm.

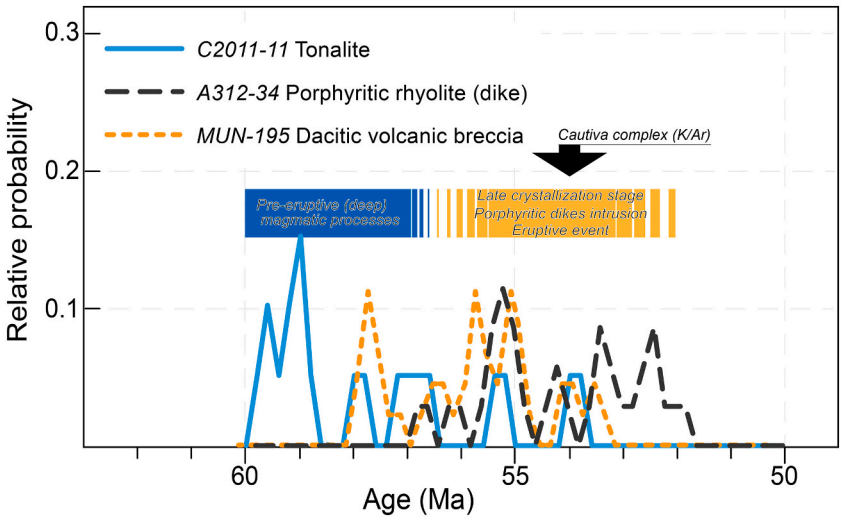

Fig. 13. Probability density distribution of U—Pb zircon ages showing the main magmatic processes depicted by the geochronological results. The K/Ar age of the volcanic rocks that cover the Cerro Munro pluton (La Cautiva complex) is taken from Turner (1982).

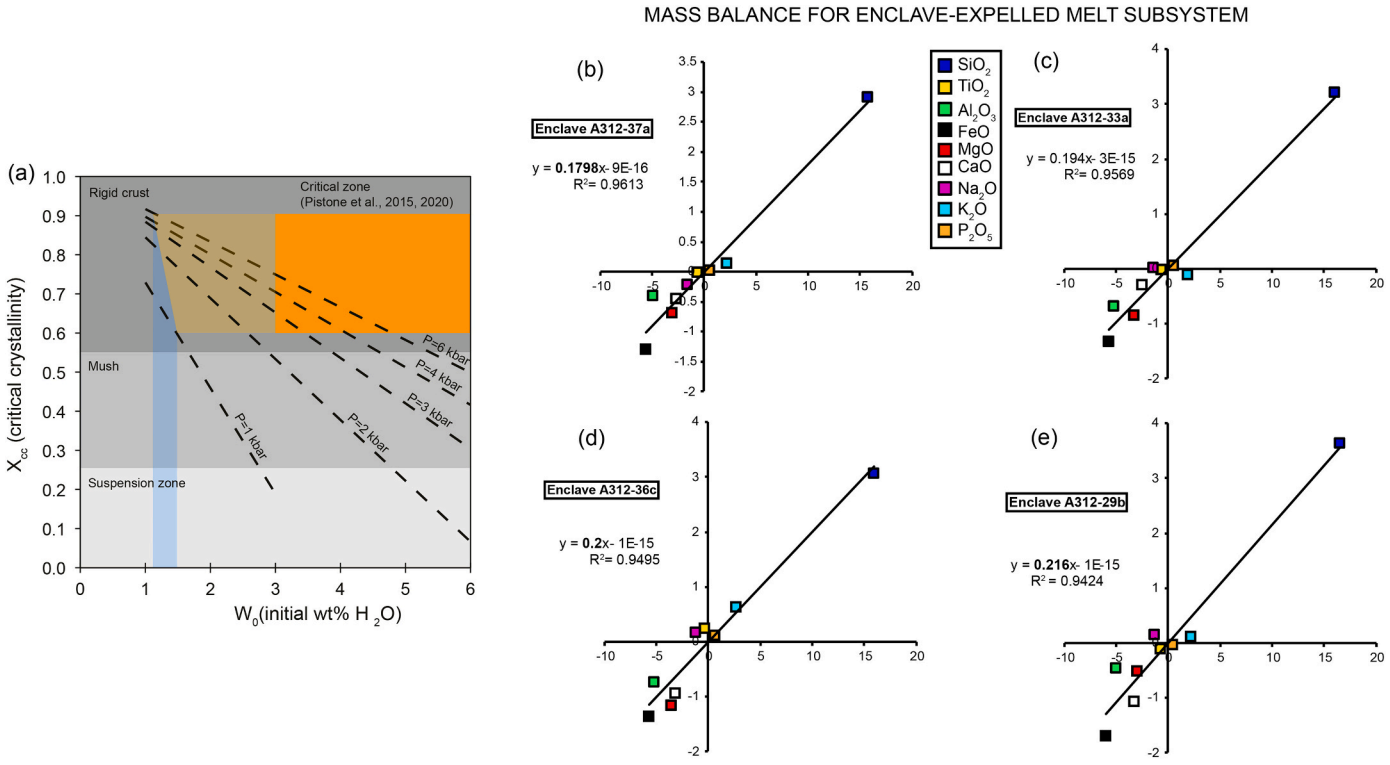

Fig. 14. (a) Plot taken from (Castro et al., 2021) of critical crystallinity vs initial water content of a granitic liquid showing the diverse zones of solidification front (Marsh, 2002) and the critical zone for melt extraction (Pistone et al., 2015; Pistone et al., 2020). This critical zone is extended to lower pressures (transparent orange zone) and the corresponding W_0 values are marked by the blue zone. (b-e) Multi elemental mass-balance of the compositional splitting process for the enclave and expelled melt subsystem. (For interpretation of the references to colour in this figure legend, the reader is referred to the web version of this article.)

Table 11
Composition of the calculated saturated liquid from the andesitic parental.

SiO_2	75.15
TiO_2	0.45
Al_2O_3	11.97
FeO	0.84
MnO	0.15
MgO	0.61
CaO	3.14
Na_2O	2.95
K_2O	3.81
P_2O_5	0.89
Total	100.0
H_2O	4

9. Conclusions

New zircon U—Pb results date the final crystallization of the Cerro Munro pluton, the eruption of rhyolitic to dacitic magmas and the intrusion of porphyritic dikes at ca. 54 *Ma*. Geochemical and petrological modelling evidences complex processes of fluid-assisted fractionation in the Cerro Munro pluton. Parental magma for tonalites and enclaves is likely of andesitic composition, represented by andesite dikes coeval with the emplacement of the pluton. Fractionation took place at possibly shallow pressure of 1 kbar, which implies very low water content of parental magma to make efficient exsolution of a water-saturated residual melt that mix with the pristine andesite to produce the tonalites. Cerro Munro can be considered as an example of in-situ fractionation at shallow depths. Rhyolitic dikes and large ignimbrite

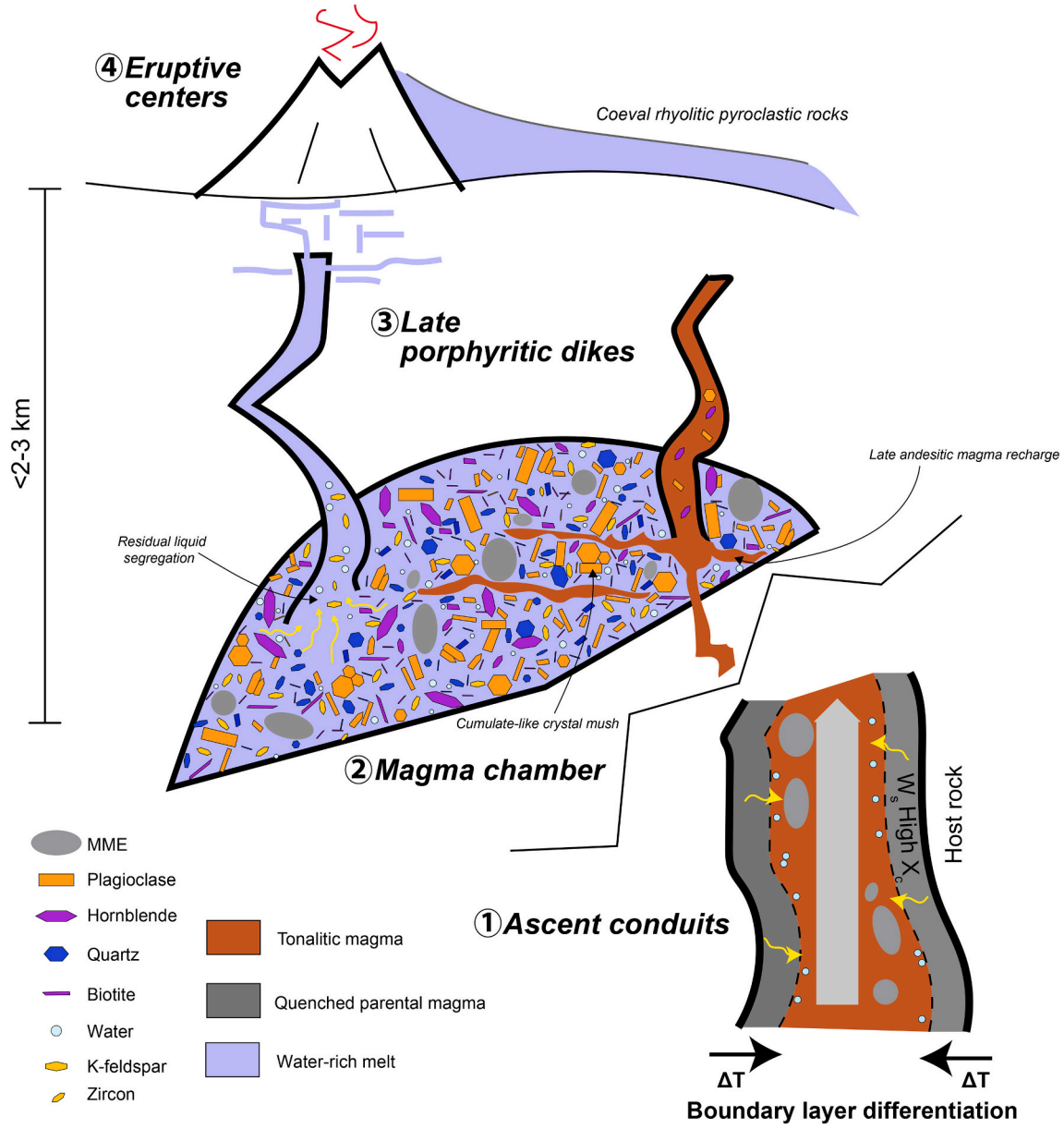

Fig. 15. Cooling model of the Cerro Munro magmatic system where the differentiation can advance at the ascent conduits (1) giving rise to rounded MME dispersed within the magma chamber (2). During a late magmatic stage (3), the porphyritic dikes extruded coinciding with the magma chamber consolidation (4). Crystal and MME size are not to scale. The ellipsoidal external form of the magma chamber was deduced from the satellite images but the in-depth morphology of the reservoir is unknown.

plateaux in the region can have resulted from similar magma chambers below large calderas.

Declaration of Competing Interest

The authors declare that they have no known competing financial interests or personal relationships that could have appeared to influence the work reported in this paper.

Acknowledgments

The manuscript has been benefited from valuable suggestions from Mattia Pistone and Jiří Žák. This work is supported by IBERCRUST project (PGC2018–096534-B-I00). C. R. is grateful for her AUIP grants (Asociación Universitaria Iberoamericana de Postgrado) for both stays at the Universidad Nacional de La Plata (Argentina), during 2015 and 2018, and for her postdoctoral contract from the University of Huelva (under the Estrategia Política Científica de la UHU 2016/2017). This is the IBERSIMS publication n°85. JM is funded by the MINECO grant CGL2017-84901-C2-P1.

Appendix A. Supplementary data

Supplementary data to this article can be found online at https://doi.org/10.1016/j.lithos.2021.106396.

References

Aragón, E., Mazzoni, M.M., 1997. Geología y estratigrafía del complejo volcánico piroclástico del río Chubut medio (Eoceno), Chubut, Argentina. Rev. Asoc. Geol. Argent. 52, 243–256.
Aragón, E., D'Eramo, F., Castro, A., Pinotti, L., Brunelli, D., Rabbia, O., Rivalenti, G., Varela, R., Spakman, W., Demartis, M., Cavarozzi, C.E., Aguilera, Y.E., Mazzucchelli, M., Ribot, A., 2011. Tectono-magmatic response to major convergence changes in the North Patagonian suprasubduction system; the Paleogene subduction–transcurrent plate margin transition. Tectonophysics 509, 218–237.
Aragón, E., Castro, A., Diaz-Alvarado, J., Pinotti, L., D'eramo, F., Demartis, M., Coniglio, J., Hernando, I., Rodriguez, C., 2018. Mantle Derived Crystal-Poor Rhyolitic Ignimbrites: Eruptive Mechanism from Geochemical and Geochronological Data of the Piedra Parada Caldera. Geoscience Frontiers, Southern Argentina.
Bachmann, O., Bergantz, G.W., 2004. On the origin of crysytal-poor rhyolites: extracted from batholitic crystal mushes. J. Petrol. 45, 1565–1582.
Bachmann, O., Bergantz, G.W., 2008. Rhyolites and their Source Mushes across Tectonic Settings. J. Petrol. 49, 2277–2285.
Bachmann, O., Huber, C., 2016. Silicic magma reservoirs in the Earth's crust. Am. Mineral. 101, 2377–2404.
Bacon, C.R., 1986. Magmatic inclusions in silicic and intermediate volcanic rocks. J. Geophys. Res. Solid Earth 91, 6091–6112.
Baedecker, P.A., 1987. Methods for geological analysis. U.S. Geol. Surv. Bull. 1770.
Bea, F., Montero, P., Stroh, A., Baasner, J., 1996. Microanalysis of minerals by an Excimer UV-LA-ICP-MS system. Chem. Geol. 133, 145–156.
Beane, R., Wiebe, R.A., 2012. Origin of quartz clusters in Vinalhaven granite and porphyry, coastal Maine. Contrib. Mineral. Petrol. 163, 1069–1082.
Black, L.P., Kamo, S.L., Allen, C.M., Aleinikoff, J.N., Davis, D.W., Korsch, R.J., Foudoulis, C., 2003. TEMORA 1: a new zircon standard for Phanerozoic U–Pb geochronology. Chem. Geol. 200, 155–170.
Boudreau, A., 2016. Bubble migration in a compacting crystal-liquid mush. Contrib. Mineral. Petrol. 171, 32.
Burnham, C.W., 1979. The importance of volatile constituents. In: Yoder, H.S.J. (Ed.), The Evolution of the Igneous Rocks. Princeton University Press, Princeton, pp. 439–482.
Castro, A., 2020. The dual origin of I-type granites: the contribution from experiments. Geol. Soc. Lond., Spec. Publ. 491, 101–145.
Castro, A., 2021. A non-basaltic experimental cotectic array for calc-alkaline batholiths. Lithos 382-383, 105929.
Castro, A., Moreno-Ventas, I., Fernández, C., Vujovich, G., Gallastegui, G., Heredia, N., Martino, R.D., Becchio, R., Corretgé, L.G., Díaz-Alvarado, J., García-Arias, M., Liu, D.-Y., 2011. Petrology and SHRIMP U-Pb zircon geochronology of Cordilleran granitoids of the Bariloche area, Argentina. J. S. Am. Earth Sci. https://doi.org/10.1016/j.jsames.2011.03.011.
Castro, A., Rodríguez, C., Diaz-Alvarado, J., Fernández, C., García-Moreno, O., 2021. Magma Differentiation and Contamination: Constraints from Experimental and Field Evidences (Magma Differentiation and Contamination).
Claoue-Long, J.C., Compston, W., Roberts, J., Fanning, C.M., 1995. Two Carboniferous ages: a comparison of SHRIMP zircon dating with conventional zircon ages and 40Ar/39Ar analysis. In: Berggren, W.A., Kent, D.V., Aubry, M.-P., Hardenbol, J. (Eds.), Geochronology, Time Scales and Global Stratigraphic Correlation, p. 362.
Cumming, G.L., Richards, J.R., 1975. Ore lead isotope ratios in a continuously changing earth. Earth Planet. Sci. Lett. 28, 155–171.
Deering, C.D., Bachmann, O., 2010. Trace element indicators of crystal accumulation in silicic igneous rocks. Earth Planet. Sci. Lett. 297, 324–331.
D'Lemos, R.S., Kearsley, A.T., Pembroke, J.W., Watt, G.R., Wright, P., 1997. Complex quartz growth histories in granite revealed by scanning cathodoluminescence techniques. Geol. Mag. 134, 549–552.
Donev, A., Cisse, I., Sachs, D., Variano, E.A., Stillinger, F.H., Connelly, R., Torquato, S., Chaikin, P.M., 2004. Improving the Density of Jammed Disordered Packings using Ellipsoids. Science 303, 990–993.
Fernández Paz, L., Litvak, V.D., Echaurren, A., Iannelli, S.B., Encinas, A., Folguera, A., 2018. Late Eocene volcanism in North Patagonia (42°30′-43° S): Arc resumption after a stage of within-plate magmatism. J. Geodyn. 113, 13–31. https://doi.org/10.1016/j.jog.2017.11.005.
Fiedrich, A.M., Bachmann, O., Ulmer, P., Deering, C.D., Kunze, K., Leuthold, J., 2017. Mineralogical, geochemical, and textural indicators of crystal accumulation in the Adamello Batholith (Northern Italy). Am. Mineral. 102, 2467–2483.
Frost, B.R., Barnes, C.G., Collins, W.J., Arculus, R.J., Ellis, D.J., Frost, C.D., 2001. A Geochemical Classification for Granitic Rocks. J. Petrol. 42, 2033–2048.
Glazner, A.F., 2014. Magmatic life at low Reynolds number. Geology 42, 935–938.
Götze, J., Plötze, M., Habermann, D., 2001. Origin, spectral characteristics and practical applications of the cathodoluminescence (CL) of quartz – a review. Mineral. Petrol. 71, 225–250.
Gualda, G.A.R., Ghiorso, M.S., Lemons, R.V., Carley, T.L., 2012. Rhyolite-MELTS: a modified calibration of MELTS optimized for silica-rich, fluid-bearing magmatic systems. J. Petrol. 53 (5), 875–890.
Guilherme, A.R.G., Mark, S.G., 2013. Low-pressure Origin of high-silica rhyolites and granites. J. Geol. 121, 537–545.
Higgins, M.D., 2017. Quantitative investigation of felsic rock textures using cathodoluminescence images and other techniques. Lithos 277, 259–268.
Iannelli, S.B., Fennell, L.M., Litvak, V.D., Fernández Paz, L., Encinas, A., Folguera, 2018. Geochemical and tectonic evolution of late cretaceous to early Paleocene magmatism along the Southern Central Andes (35-36°S). J. S. Am. Earth Sci. 87, 139–156. https://doi.org/10.1016/j.jsames.2017.12.008.
Janoušek, V.c., Bowes, D.R., Braithwaite, C.J.R., Rogers, G., 2000. Microstructural and mineralogical evidence for limited involvement of magma mixing in the petrogenesis of a Hercynian high-K calc-alkaline intrusion: The Kozárovice granodiorite, Central Bohemian Pluton, Czech Republic. In: Barbarin, B., Stephens, W.E., Bonin, B., Bouchez, J.-L., Clarke, D.B., Cuney, M., Martin, H. (Eds.), The Fourth Hutton Symposium on the Origin of Granites and Related Rocks. Geological Society of America.
John, B.E., Blundy, J.D., 1993. Emplacement-related deformation of granitoid magmas, southern Adamello Massif, Italy. GSA Bull. 105, 1517–1541.
John, B.E., Stünitz, H., 1997. Magmatic Fracturing and Small-Scale Melt Segregation during Pluton Emplacement: Evidence from the Adamello Massif (Italy). In: Bouchez, J.L., Hutton, D.H.W., Stephens, W.E. (Eds.), Granite: From Segregation of Melt to Emplacement Fabrics. Springer Netherlands, Dordrecht, pp. 55–74.
Kirkpatrick, R.J., 1981. Kinetics of crystallization of igneous rocks. Rev. Mineral.; (United States), Medium: X; Size: Pages: 321–395.
Langmuir, C.H., 1989. Geochemical consequences of in situ crystallization. Nature 340, 199–205.
Lee, C.T.A., Morton, D.M., 2015. High silica granites: Terminal porosity and crystal settling in shallow magma chambers. Earth Planet. Sci. Lett. 409, 23–31.
Lee, C.-T.A., Morton, D.M., Farner, M.J., Moitra, P., 2015. Field and model constraints on silicic melt segregation by compaction/hindered settling: the role of water and its effect on latent heat release. Am. Mineral. 100, 1762–1777.
Locock, A.J., 2014. An Excel spreadsheet to classify chemical analyses of amphiboles following the IMA 2012 recommendations. Comput. Geosci. 62, 1–11.
Ludwig, K.R., 2003. Mathematical–Statistical Treatment of Data and Errors for 230Th/U Geochronology. Rev. Mineral. Geochem. 52, 631–656.
Marsh, B.D., 2002. On bimodal differentiation by solidification front instability in basaltic magmas, part 1: basic mechanics. Geochim. Cosmochim. Acta 66, 2211–2229.
Masotta, M., Beier, C., Mollo, S., 2021. Crustal Magmatic System Evolution: Anatomy, Architecture and Physics-Chemical. AGU-Wiley.
Matthews, N.E., Pyle, D.M., Smith, V.C., Wilson, C.J.N., Huber, C., Hinsberg, V., 2011. Quartz zoning and the pre-eruptive evolution of the ~340-ka Whakamaru magma systems, New Zealand. Contrib. Mineral. Petrol. 163, 87–107.
Matthews, N.E., Huber, C., Pyle, D.M., Smith, V.C., 2012. Timescales of Magma Recharge and Reactivation of large Silicic Systems from Ti Diffusion in Quartz. J. Petrol. 53, 1385–1416.
Montero, P., Bea, F., Corretgè, L.G., Floor, P., Whitehouse, M.J., 2008. U-Pb ion microprobe dating and Sr and Nd isotope geology of the GaliÒeiro Igneous complex: a model for the peraluminous/peralkaline duality of the Cambro-Ordovician magmatism of Iberia. Lithos 107, 227–238.
Muñoz, J., Troncoso, R., Duhart, P., Crignola, P., Farmer, L., Stern, C.R., 2000. The relation of the mid-Tertiary coastal magmatic belt in south-central Chile to the late Oligocene increase in plate convergence rate. Rev. Geol. Chile 27, 177–203.
Nakamura, N., 1974. Determination of REE, Ba, Fe, Mg, Na and K in carbonaceous and ordinary cohondrites. Geochim. Cosmochim. Acta 38, 757–775.
Naney, M.T., 1983. Phase equilibria of rock-forming ferromagnesian silicates in granitic systems. Am. J. Sci. 283, 993–1033.
Pistone, M., Arzilli, F., Dobson, K.J., Cordonnier, B., Reusser, E., Ulmer, P., Marone, F., Whittington, A.G., Mancini, L., Fife, J.L., Blundy, J.D., 2015. Gas-driven filter pressing in magmas: Insights into in-situ melt segregation from crystal mushes. Geology 43, 699–702.

Pistone, M., Baumgartner, L.P., Bégué, F., Jarvis, P.A., Bloch, E., Robyr, M., Müntener, O., Sisson, T.W., Blundy, J.D., 2020. Felsic Melt and Gas Mobilization during Magma Solidification: an Experimental Study at 1.1 kbar. Front. Earth Sci. 8.
Rapela, C.W., Spalletti, L., Merodio, J.C., 1983. Evolución magmática y geotectónica de la Serie Andesitica andina (Paleoceno–Eoceno) en la cordillera norpatagónica. Rev. Asoc. Geol. Argent. 38, 469–484.
Rapela, C.W., Spalletti, J.C., Aragón, E., 1987. Temporal evolution and spatial variation of the lower tertiary Andean volcanism (40-42 30'S). J. S. Am. Earth Sci. 1, 1–14.
Ridolfi, F., Renzulli, A., 2012. Calcic amphiboles in calc-alkaline and alkaline magmas: thermobarometric and chemometric empirical equations valid up to 1,130°C and 2.2 GPa. Contrib. Mineral. Petrol. 163, 877–895.
Ridolfi, F., Renzulli, A., Puerini, M., 2010. Stability and chemical equilibrium of amphibole in calc-alkaline magmas: an overview, new thermobarometric formulations and application to subduction-related volcanoes. Contrib. Mineral. Petrol. 160, 45–66.
Rodríguez, C., Castro, A., 2017. Silicic magma differentiation in ascent conduits. Experimental constraints. Lithos 272–273, 261–277.
Rodríguez, C., Castro, A., 2018. Origins of mafic microgranular enclaves and enclave swarms in granites: field and geochemical relations. GSA Bull. 131, 635–660.
Savignano, E., Mazzoli, S., Arce, M., Franchini, M., Gautheron, C., Paolini, M., Zattin, M., 2016. (Un)coupled thrust belt-foreland deformation in the northern Patagonian Andes: New insights from the Esquel-Gastre sector (41°30′–43°S). Tectonics 35, 2636–2656.
Sisson, T.W., Bacon, C.R., 1999. Gas-driven filter pressing in magmas. Geology 27, 613–616.
Spikermann, J.P., 1978. Contribución al conocimiento de la intrusividad en el Paleozoico de la región extraandina del Chubut. Rev. Asoc. Geol. Argent. 33.
Steiger, R.H., Jäger, E., 1977. Subcommission on geochronology: convention on the use of decay constants in geo- and cosmochronology. Earth Planet. Sci. Lett. 36, 359–362.
Sunagawa, I., 1981. Characteristics of crystal growth in nature as seen from the morphology of mineral crystals. Bull. Mineral. 104, 81–87.
Turner, J.S., 1982. Descripción Geológica de la Hoja 44c, Tecka, Provincia de Chubut. Serv. Geol. Nacional Bol. 180, 92.
Vernon, R.H., Collins, W.J., 2011. Structural criteria for identifying granitic cumulates. J. Geol. 119, 127–142.
Weinberg, R.F., Vernon, R.H., Schmeling, H., 2021. Processes in mushes and their role in the differentiation of granitic rocks. Earth Sci. Rev. 103665.
Whitney, D.L., Evans, B.W., 2010. Abbreviations for names of rock-forming minerals. Am. Mineral. 95, 185–187.
Wiebe, R.A., Wark, D.A., Hawkins, D.P., 2007. Insights from quartz cathodoluminescence zoning into crystallization of the Vinalhaven granite, coastal Maine. Contrib. Mineral. Petrol. 154, 439–453.
Williams, I.S., 1998. U-Th-Pb geochronology by ion microprobe. In: McKibben, M.A., Shanks III, W.C., Ridley, W.I. (Eds.), Applications of Microanalytical Techniques to Understanding Mineralizing Processes. Reviews in Economic Geology, pp. 1–35.
Wyllie, P.J., Cox, K.G., Biggar, G.M., 1962. The Habit of Apatite in Synthetic Systems and Igneous Rocks. J. Petrol. 3, 238–243.
Xu, W., Zhu, D.-C., Wang, Q., Weinberg, R.F., Wang, R., Li, S.-M., Zhang, L.-L., Zhao, Z.-D., 2021. Mafic microgranular enclaves formed by gas-driven filter pressing during rapid cooling: an example from the Gangdese batholith in Southern Tibet. J. Petrol. 61.